

HOLLOW BEAM ATOM TUNNEL

by

Yonho Song

A Dissertation submitted to the Faculty of the Graduate School
of the University of Maryland, College Park in partial
fulfillment of the requirements for the degree
of Doctor of Philosophy
1999

Advisory committee:

Professor Wendell T. Hill III, Chairman

Professor Carroll O. Alley

Professor Frederick C. Wellstood

Professor Rajarshi Roy

Professor Millard H. Alexander

ABSTRACT

Title of Dissertation: HOLLOW BEAM ATOM TUNNEL

Yonho Song, Doctor of Philosophy, 1999

Dissertation directed by: Professor Wendell T. Hill III

Institute for Physical Science and Technology

One of the more promising proposals for guiding and focusing neutral atoms involves dark hollow laser beams. When the frequency of the laser is detuned to the blue of resonance, the dipole force the atoms feel in the light confines them to the dark core where the atoms can be transported with minimal interaction with the light. The ability of the all-light atom guides to transport large number of ultracold atoms for long distances without physical walls leads to the possibility of a versatile tool for atom lithography, atom interferometry, atomic spectroscopy as well as for transporting and manipulating Bose-Einstein condensates. Furthermore since the atoms transported in all-light atom guides do not come into contact with matter, they can in principle be used to transport antimatter as well.

In this work a hollow beam atom tunnel is demonstrated by guiding magneto-optically trapped ultracold cesium atoms with a hollow core laser beam. The 1mm

diameter diffractionless hollow beam used to construct the atom tunnel was generated from a TEM_{00} mode diode laser at 852 nm using a series of axicons and simple lenses. The axicon generated hollow beam has a dark core extended for most of its diameter and steep walls suitable for an atom guide. Ultracold cesium atoms loaded into the tunnel from a MOT spend 90% of their time in the dark, scattering photons only when they collide with the light walls. We modeled the evolution of atoms using the interaction between the atoms and the light walls, which agreed well with experimental observations. The direction and speed of the atoms in the tunnel can be controlled by varying the detuning of the tunnel beam.

The ability to vary the core size of the hollow beam makes the all-light atom guide potentially useful for focusing neutral atoms. The atoms could be focused as tight as the core size of the hollow beam at its waist. This new focusing scheme, called the atom funnel, would not show spherical and chromatic aberrations that conventional harmonic focusing suffers from.

© Copyright by

Yonho Song

1999

ACKNOWLEDGMENTS

First of all, I send my thanks and love to my parents. My mother encouraged me to overcome all the trials I met. She was always with me and will live forever in my memory. My father supported me with endless love. I dedicate this dissertation to them.

This work would have been impossible without my advisor, Professor Wendell T. Hill III. He led me with a great deal of patience in situations where nothing was clear. He gave me the directions I should follow and also pointed out the details I missed.

I also thank all the colleagues and friends who helped me. Dr. Jie Zhu gave me much advice and I learned from him most of what I needed to know in the lab. Dan Milam helped me as a friend and collaborator. Tyson Lee saved me a lot of time with his wonderful mechanical engineering skill. I really enjoyed friendship with Frederik Adamietz while he was visiting our lab. I also thank Bill Degraffenreid for useful discussion. I will miss my new lab mate Kun Zhao and hope for much success in his research in this lab.

The support of my family is what kept me going. My wife endured all the troubles and never stopped believing in me. When I was tired from working in the lab late in the night, I thought of my son and daughter, how lovely they were.

TABLE OF CONTENTS

<u>Section</u>	<u>Page</u>
1 INTRODUCTION	1
2 INTERACTIONS BETWEEN ATOMS AND LIGHT	13
2.1 Hermite-Gaussian vs. Laguerre-Gaussian modes	13
2.2 Scattering force and laser cooling	16
2.3 Optical heating and cooling limits	23
2.4 Dipole interaction	25
3 EXPERIMENTAL APPARATUS	30
3.1 Diode lasers	30
3.1.1 Mechanical mounting and collimating optics	32
3.1.2 Temperature stabilization	34
3.1.3 Tuning characteristics and external cavities.	36
3.2 Saturated absorption spectroscopy and frequency locking	41
3.3 Optical delivery of the laser beam	45
3.3.1 Optical components	45
3.3.2 The shutters	49
3.4 The vacuum chamber and pumping system	51
3.5 Other instruments	54
3.5.1 Oscilloscopes	54
3.5.2 Spectrum analyzer.	54
4 MAGNETO-OPTICAL TRAP OF CESIUM AND A CRUDE ATOM TUNNEL	56
4.1 Cesium	56
4.2 Principles of MOT	59
4.3 Experimental arrangement	64
4.4 MOT loading parameters	68
4.5 Imaging schemes and the temperature measurement	66
4.6 Crude atom tunnel	75
5 EVOLUTION OF ULTRACOLD ATOMS IN THE AXICON GENERATED HOLLOW BEAM	86
5.1 Generating hollow core beams	86
5.2 Evolution of atoms in the hollow beam atom tunnel	97
5.2.1 The interactions between the atoms and the light wall	97
5.2.2 Shape factor and ensemble heating	99
5.2.3 Maximum hold times and optimum detuning.	105
6 ALL-LIGHT ATOM TUNNEL	111

6.1 Horizontal images and scattering acceleration	111
6.2 Levitating the atoms	120
6.3 Longitudinal images and loss mechanism	123
7 ATOM FUNNEL	132
7.1 Harmonic focusing and aberrations	132
7.2 Atom funnel	137
8 SUMMERY	144
REFERENCES	146

List of Figures

<u>Figure</u>	<u>Page</u>
1.1 The physics of intense lasers	3
1.2 Hot beam vs. cold beam	4
1.3 Vapor pressure vs. temperature for alkali metals	7
1.4 Axicon generated hollow beam vs. TEM ₀₁ * mode beam	10
2.1 Intensity profiles of some low order LG _{0m} modes	17
2.2 The drift velocity as a function of distance	21
2.3 Principle of laser cooling	22
2.4 Focusing with dipole force for Gaussian and donut modes	26
2.5 Dipole potential of TEM ₀₁ * mode as a function of detuning	27
3.1 Overall experimental setup	31
3.2 Schematic of the diode laser mount and housing	33
3.3 Temperature control circuit for diode laser	35
3.4 Two designs of the external cavity	38
3.5 Spectra for the external cavity diode lasers	40
3.6 Saturated absorption spectroscopy	42
3.7 (a) Saturated absorption signal for $6^2S_{1/2}(F=3) \rightarrow 6^2P_{3/2}(F'=2,3,4)$	43
(b) Saturated absorption signal for $6^2S_{1/2}(F=4) \rightarrow 6^2P_{3/2}(F'=3,4,5)$	44
3.8 Circuit diagram for I-V converter and sidelock servo	46
3.9 The wave plates and polarizing beam splitters	48
3.10 Schematic of Acousto-Optic Modulator (AOM) setup	50
3.11 The vacuum chamber	52
4.1 Energy level structure of Cs	57
4.2 One-dimensional model of the Magneto-Optical Trap	60
4.3 The MOT laser beam arrangement	63
4.4 MOT buildup	67
4.5 Number of atoms in the MOT as a function of the background Cs pressure	70
4.6 The fluorescence image and the density profile of a MOT	72

4.7	Shadow images and the density profile	72
4.8	Timing scheme for shadow imaging	74
4.9	The horizontal size of a MOT measured at consecutive times.	76
4.10	Setup for the crude atom tunnel	77
4.11	Spatial images and radial intensity profiles of the hollow beam.	79
4.12	Shadow images showing 9 ms of evolution of the atom cloud with and without the tunnel beam	80
4.13	Horizontal (transverse) size of the atom cloud with and without the tunnel beam	83
4.14	Vertical (longitudinal) size of the atom cloud with and without the tunnel beam	84
4.15	Vertical position of the atom cloud with and without the tunnel beam	85
5.1	Spherical lens vs. axicon	88
5.2	(a) Hollow beam images generated by an axicon and lenses	91
	(b) Hollow beam images generated with an axicon replacing the second lens	92
5.3	The optical setup for generating a collimated hollow beam	94
5.4	Spatial images and radial profiles of the axicon generated beam	95
5.5	Extended harmonic potential and shape factor for various potentials	101
5.6	Shape factor for TEM_{01}^* beam and the axicon beam.	103
5.7	(a) Increase in the transverse kinetic energy spread in a TEM_{01}^* beam	108
	(b) Increase in the transverse kinetic energy spread in our axicon generated hollow beam	109
6.1	Transverse shadow images of the atom cloud in the tunnel beam directed downward	112
6.2	Transverse density profile of an atoms cloud in the tunnel	114
6.3	Vertical position of the atoms clouds	115
6.4	Scattering acceleration of the atom clouds at $T = 80 \mu K$ with different detunings of the tunnel beam.	117
6.5	Longitudinal size of the atom clouds in the tunnel.	119
6.6	Transverse shadow images of the atom cloud in the tunnel beam directed upward	121

6.7	Vertical position of the atom clouds in the tunnel directed upward	122
6.8	Setup for longitudinal shadow imaging	124
6.9	Longitudinal shadow images of the atom clouds	125
6.10	The number of atoms I the tunnel vs. time for longitudinal images	126
6.11	The number of atoms in the tunnel vs. time with different detunings	130
7.1	Harmonic focusing of an atomic beam	133
7.2	Focusing an atomic beam with the TEM ₀₁ * donut mode laser beam	136
7.3	A prototype design of atom funnel	138
7.4	The adiabatic heating and bounce back of atoms thrown into a funnel	140
7.5	Shadow images of the atom cloud in the funnel without the repumping beam	142

CHAPTER 1

INTRODUCTION

Tunable laser sources developed in recent decades have enabled the manipulation of neutral atoms with laser light. An ability to control the momentum and energy of atoms with laser light has led to laser cooling and trapping that allowed new sources of atomic samples. High density ($n > 10^{11}/\text{cm}^2$), ultracold ($T < 1$ mK) atomic ensembles in magneto-optical traps (MOT) [1] have made new experiments possible, including ultracold collisions [2, 3, 4], photoassociation of ultracold atoms [5, 6, 7], ultraprecision spectroscopy [8, 9] and Bose-Einstein condensation [10].

Another useful application is to produce an ultracold atomic beam. A well collimated atomic beam with high flux density is desirable in many applications, including atom lithography, atom interferometry, atomic spectroscopy and collision studies. Ultracold atomic beams generated from laser cooled and trapped atoms have small drift velocities that can be controlled with radiation pressure. The direction of the colliding partners in collision studies can be varied arbitrarily, including head-on collisions. The small drift velocity increases the time that the atoms spend in the experiment. This can be used, for example, to enhance the resolution of atomic clocks. The small energy distribution of the ultracold atomic beam might greatly enhance the resolution of pattern formation in atomic lithography [11, 12]. The small energy distribution might also make it possible to focus the beam of atoms to a small spot. A tightly focused atomic beam is useful, especially in intense laser field experiments where the peak laser intensity far exceeds the saturation intensity for multiphoton ionization.

When the peak laser intensity is extremely high, even the intensity in the wings of the beam can be high enough to cause significant ionization. Since the number of atoms exposed to the edge of the beam is considerably larger than that exposed to the core, as shown in Fig. 1.1, ionization processes occurring near the peak are hard to distinguish from those resulting from the low intensity wing. Isolation of intense field processes in this situation involves a cumbersome integral over the whole laser field. This problem can be avoided by preparing an atomic target smaller than the core size of the laser beam.

The need for a small atomic target was the motivation of my work for this thesis. A small atomic target would produce clearer strong field spectra. It enables us to look for novel ionization processes that are predicted to occur at intensities of 10^{16} W/cm² and above. We could also study strong field ionization by looking at ion recoil, which would be possible with cold atoms.

A simple way to generate an ultracold atomic beam is to kick the trapped atoms with a laser as shown in Fig. 1.2. The terminal velocities of the atoms range from a few meters per second to a few tens of meters per second, depending on the intensity and detuning of the laser, as will be discussed in Ch. 2. These velocities are much smaller than the drift velocity of several hundred meters per second in conventional hot atomic beams effused from hot ovens. After the ultracold atoms from a MOT are accelerated to 20 m/s, the velocity spread of the atoms is ~ 20 cm/s, which is a hundred times smaller than the drift velocity. The velocity spread of effusive beams is about the same as the drift velocity of the beam (i.e. $\delta v_z/v_z \sim 1$) without velocity selection. Therefore, compared to effusive beams, the ultracold beam is almost mono-energetic. This turns out to be important for focusing an atomic beam to small sizes.

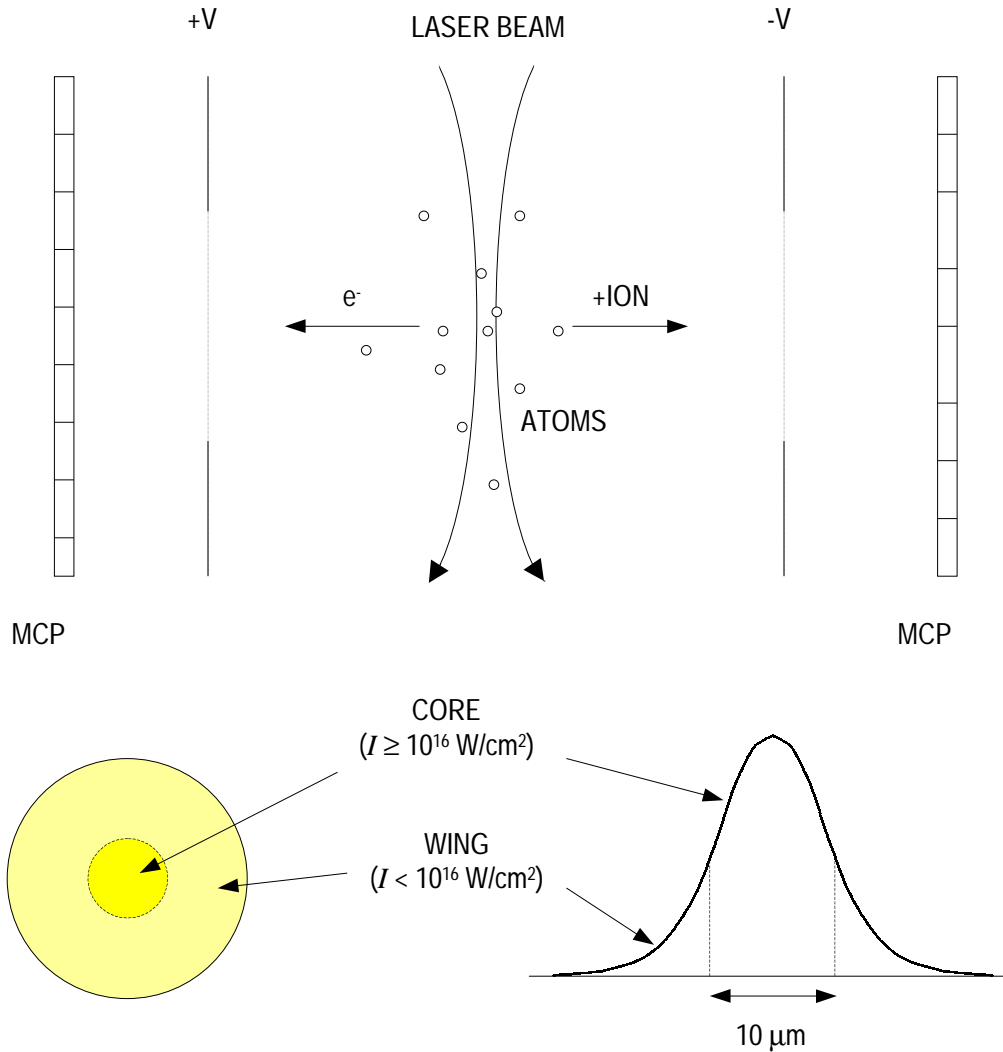


Figure 1.1 The physics of intense lasers. The tightly focused intense laser has a core size of $\sim 10 \mu\text{m}$ where the atoms interact with the intense field. The wing of lower intensity is much wider than the core. The ions and electrons resulting from the ionization are extracted by the DC field and detected by the micro channel plates (MCP). Most of the ionization signal comes from the less intense wing.

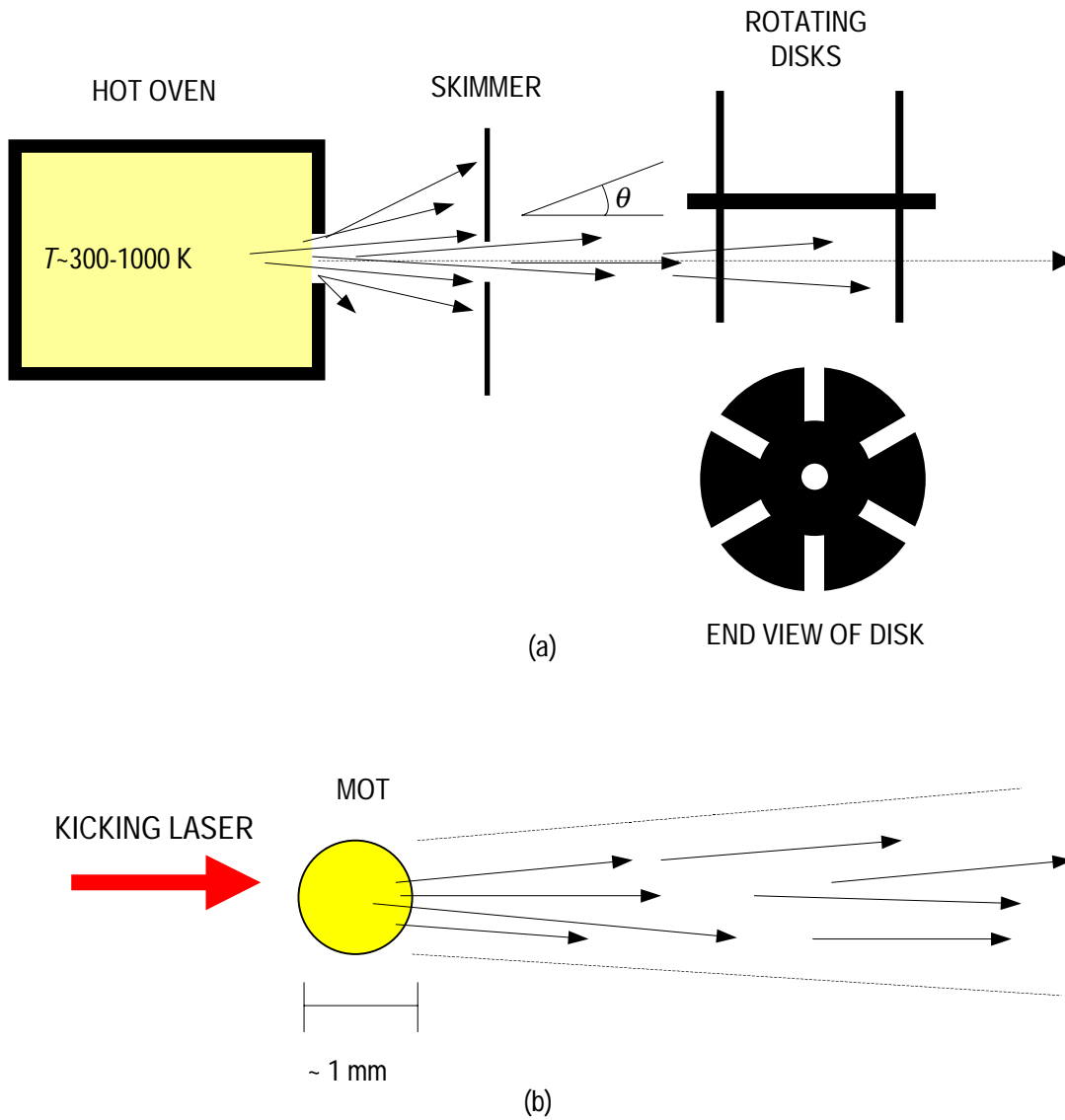


Figure 1.2 Hot beam vs. cold beam. (a) Effusive beam from an oven. The hot beam has large velocity distribution ($\delta v_z / v_z \sim 1$) and large divergence ($\cos^2\theta$ distribution around the propagation axis) without the velocity chopper and the skimmer. (b) Ultracold atomic beam from a MOT. The drift velocity depends on the intensity and detuning of the kicker beam.

Another advantage that ultracold beams have over hot beams is their large flux. If trapped atoms were continuously loaded into a beam, the flux of the ultracold beam would be the same as the number of atoms captured by the trap per unit time, which is $\sim 10^9$ atoms per second at $P = 10^{-7}$ Torr as will be discussed in Ch. 4 for magneto-optical trap. The instantaneous flux, however, can be many orders of magnitude higher when pulsed beams are generated. The flux of a pulsed beam is given by:

$$\Phi = \frac{\text{\# of atoms in the beam}}{l/v_z}, \quad (1.1)$$

where l is the size of the beam in the longitudinal direction and v_z the drift velocity. When a 1 mm cloud of atoms at a typical MOT temperature of ~ 100 μK travels 20 cm, its speed would reach 20 m/s, and its size would have expanded to ~ 2 mm. The flux at this position is $\sim 10^{13}$ s^{-1} ; the flux density would be $\sim 2 \times 10^{14}$ $/\text{cm}^2 \cdot \text{s}$. While an ultracold beam has higher peak flux when made pulsed, hot beams have the same peak flux in both continuous and pulsed beam. Consider an effusive beam move closely. The number of atoms that emerge per second from a small hole into a solid angle Ω with velocity $v - v + \delta v$ is given by [13]:

$$\Phi = \int_v^{v+\delta v} An \left(\frac{m}{2\pi kT} \right)^{3/2} e^{-\frac{mv^2}{2kT}} v^3 dv \int_{\Omega} \cos \theta d\Omega, \quad (1.2)$$

where A is the area of the hole, n the number density of the atoms in the oven and θ the azimuthal angle as shown in Fig. 1.2a. Without any velocity selection, a Cs beam with a 1 mm diameter, 20 cm away from the oven at $T = 500$ K ($P \approx 0.1$ Torr) effused through a 100 μm diameter hole would have a flux of $\sim 10^{10}$ s^{-1} (flux density of $\sim 10^{12}$ $/\text{cm}^2 \cdot \text{s}$). If a velocity group $v - v + \delta v$ is selected with a velocity chopper as shown in Fig. 1.2a, the flux would be reduced by $\delta v / \langle v \rangle$, where $\langle v \rangle$ is the average velocity over the whole Maxwell-Boltzmann distribution. Other alkali metals have lower vapor pressure (see Fig. 1.3), and therefore a smaller flux. The flux of a hot atomic beam is several orders of magnitude smaller than that of the pulsed ultracold atomic beam. The large drift velocity of the hot beam makes the situation even worse. For example, in the ionization experiment by short pulsed (femto second) intense lasers, the number of atoms in the laser focus is an important quantity to be considered. The number density (flux density divided by drift velocity) in a hot beam would be $\sim 10^7$ $/\text{cm}^3$. This gives only one atom contained in the focal volume of a laser focused to 10 μm with a Rayleigh length of 500 μm . Meanwhile, the ultracold beam launched by a kicker has the density of $\sim 10^{11}$ $/\text{cm}^3$ which gives $\sim 10^4$ atoms in the focal volume.

Though a small drift velocity of an ultracold beam is desirable in many situations, the divergence ($\theta = v_t/v_z$ where v_t is the transverse velocity and v_z the drift velocity), especially just after the atoms are launched, needs to be controlled. In the above example, the ultracold atomic beam expanded by a factor of ~ 2 after it traveled 20 cm. This limits the usefulness of the ultracold beam in experiments where localized atomic samples are required. The divergence of the ultracold beam can be avoided by guiding the atoms. This desire to control the divergence was the impetus that led to the

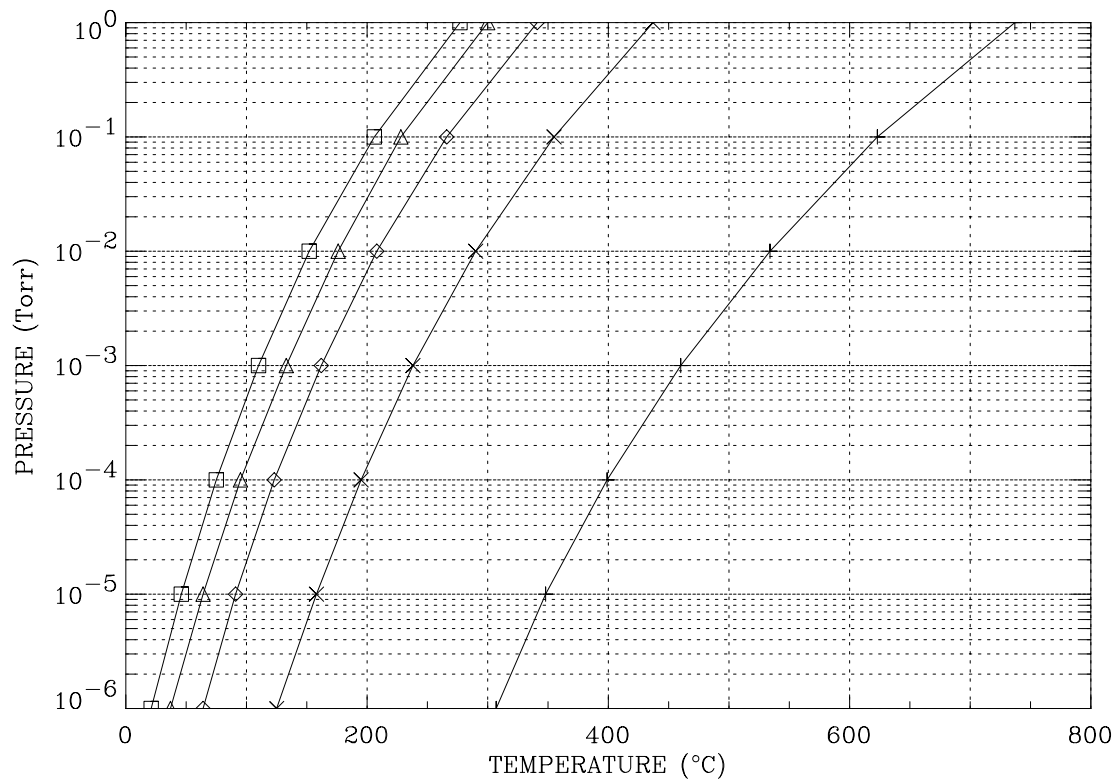


Figure 1.3 Vapor pressure vs. temperature for alkali metals: Li (+), Na (x), K (◇), Rb (△) and Cs (□).

development of our atom tunnel, a novel method of generating and transporting an ultracold atomic beam [14]. The atom tunnel employs a hollow core laser beam detuned above the resonance frequency. The dipole force supplied by the gradient of the laser field confines the atoms in the dark core where the atoms can be transported with minimal interaction. The ultracold atoms, therefore, can be transported for long distances without divergence. For an ultracold atomic ensemble whose velocity spread is very small (~ 10 cm/s), the small momentum transfer from photons (0.4 cm/s per photon absorption for Cs atoms) is not negligible. The spontaneous emission in random directions quickly increases the velocity spread of the atoms when they stay in the laser field. The atoms will acquire kinetic energy larger than the potential depth and escape the tunnel. This optical heating is suppressed in hollow core beams since the atoms spend most of their time in the dark. The hollow beam atom tunnel also provides an ability to control the speed and direction of the atomic beam. The acceleration in the tunnel can be varied by changing the frequency of the tunnel laser. In our atom tunnel experiment, the tunnel laser itself served to launch and accelerate the atoms. The optical acceleration by the tunnel beam ranges from 2 m/s^2 to 15 m/s^2 . When the tunnel beam was directed against gravity, it was possible to levitate the atoms. The ability to control the acceleration gives the experimenter a knob for varying the velocity of the atoms in the guide. Compared with other methods of generating ultracold beams, such as the ‘Atom Funnel’ by E. Riis *et al.* [15] and ‘LVIS’ (low intensity intense source) by Z. Lu *et al.* [16], the hollow beam atom tunnel generates a diffractionless atomic beam and provides an independent control of the speed, direction and size of the beam. While other methods

lose their control after the atoms are launched, the atomic tunnel keeps control during the entire transport process.

Another type of atom guide developed in recent years is the hollow fiber guide that employed evanescent waves in the hollow core. Compared with fiber guides [17, 18, 19], the hollow beam atom tunnel has a relatively large core size ($\sim 100 \mu\text{m} - \sim 1 \text{mm}$) and wall thickness ($>10 \mu\text{m}$). This eliminates the quantum tunneling loss, allowing bulk guiding of atoms for long distances. The hollow beam atom tunnel does not show cavity QED effects because it does not employ physical walls. The absence of physical walls also makes loading much easier because a MOT can be formed inside the tunnel beam. Moreover, the tunnel beam can be turned on and off. The all-light atom tunnel, therefore, may be useful for manipulating and transporting Bose-Einstein condensates and antimatter as well. Furthermore, the ability to control the core size of the hollow beams might allow them to be used for focusing ultracold atoms.

As we were developing the hollow beam atom tunnel, other experimental groups also started guiding and focusing experiments. There are three differences between these guide experiments [20, 21] and ours. First, we generated a hollow beam that had a large dark core and a steep wall using axicons; others generated low order donut modes that are approximately TEM_{01}^* modes. Whereas TEM_{01}^* modes have zero intensity only at the center, an axicon generated hollow beam has zero intensity extended over most of its diameter and a narrow wall where the power is concentrated as shown in Fig. 1.4. Atom guides made of TEM_{01}^* modes provide about 10 times higher heating rates and about 3 times lower potential than the axicon tunnel with the same power and frequency. Atoms

in TEM_{01}^* modes therefore are lost more quickly from the guides. The high efficiency of the axicon method makes it possible to guide atoms with low power diode lasers.

The second difference is that we followed the atoms all the way through their travel in the tunnel using a shadow imaging technique; others measured only the final flux at the detector. Shadow images of atoms enabled us to monitor the evolution of

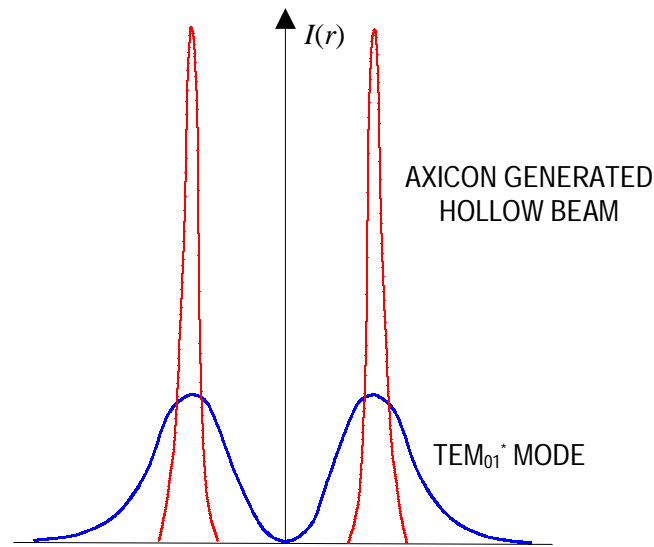


Figure 1.4 Axicon generated hollow beam vs. TEM_{01}^* mode beam. Assuming the same power and peak-to-peak diameter for the two beams, the axicon generated beam has a peak intensity about 3 times higher than the TEM_{01}^* mode beam. The axicon beam has a dark core extended over most of its diameter and steep walls where most of the power is concentrated. Atoms confined in the axicon beam spend most of their time in the dark, scattering photons only when they collide with the walls.

atomic ensembles in the tunnel. We analyzed quantitatively characteristics of the atomic ensembles, such as the total number, density distribution, the center-of-mass position and the size as a function of time.

The third difference is that we explained the evolution of atom clouds by modeling the interaction between the atoms and the light wall. We included spontaneous emission in our model, which was ignored in other analyses. The position and size of atom clouds in the hollow tunnel beam were evaluated by considering ensemble average of optical acceleration and heating. Experimental observations agreed well with our simple one-dimensional model.

In this thesis, I will discuss the basic optics theory and experimental apparatus as well as the experiments I performed. I hope in this way to provide a useful reference for experimenters who are involved with similar subjects. In Chapter 2, I discuss the interactions between the atoms and light, including resonance scattering, optical heating, and the dipole force. I will give a Brief description of Gaussian and donut modes. Chapter 3 deals with the experimental apparatus, such as external cavity diode lasers, the saturation absorption spectrometer, and various optical components. In Ch. 4, I will discuss the theory and properties of the MOT. A preliminary guiding experiment with a crude atom beam is demonstrated in the latter part of the chapter. In Ch. 5, I will explain a simple way to generate hollow beams with axicons and other optics. Evolution of the atoms in the axicon generated hollow beam will also be discussed in Ch. 5. Results and analysis of my atom tunnel experiment will be provided in Ch. 6. In Ch. 7, I will discuss various possible focusing schemes and the possibility of making an atom funnel. In Ch 8,

I will summarize my works and suggest possible application of the atom funnel and tunnel.

CHAPTER 2

INTERACTIONS BETWEEN ATOMS AND LIGHT

The history of manipulating neutral atoms with light goes back to the beginning of this century, when the first experimental proof of light pressure was obtained by Lebedev in 1901 [22]. An attempt to deflect a sodium atomic beam by radiation pressure from a sodium lamp was made in 1933 [23]. The low spectral brightness of the lamp in this pre-laser period allowed deflection by only 0.01 mm. Development of coherent light sources (lasers) gave scientists a powerful tool for manipulating atomic motion. With lasers, one can totally change the direction and speed of neutral atoms.

In this chapter I discuss the basic interactions between atoms and laser light. This includes resonance absorption, spontaneous reemission and the dipolar interaction as discussed in section 2.2, 2.3 and 2.4 respectively. Spatial modes of the laser in free space, such as Hermite-Gaussian modes or Laguerre-Gaussian modes are discussed in section 2.1.

2.1 Hermite-Gaussian modes vs. Laguerre-Gaussian modes

For the purpose of this thesis, laser beams can be divided into two categories according to their spatial modes, a Gaussian mode and donut modes. The Gaussian mode is a fundamental mode in laser propagation and has its maximum intensity at the center. The donut modes are higher order modes that have zero intensity at the center. A general treatment of laser modes can be found in *Lasers* by Siegman [24], where the electromagnetic wave equation is solved under the *paraxial approximation*.

If the z -dependence of the wave amplitude is slow compared to the wavelength and the transverse variation due to the finite width of the beam, the solutions to the

electromagnetic wave equation $\left[\nabla^2 - \frac{1}{c^2} \frac{\partial^2}{\partial t^2} \right] E(\vec{r}, t) = 0$ are given by:

$$E(\vec{r}, t) = u_{pm}(r, \theta, z) e^{-ikz - i\omega t}, \quad (2.1)$$

where

$$u_{pm}(r, \theta, z) = \sqrt{\frac{2p!}{(1 + \delta_{0m})\pi(m+p)!}} \frac{\exp(i(2p+m+1)(\varphi(z) - \varphi_0))}{w(z)} \times \left(\frac{\sqrt{2}r}{w(z)} \right)^m L_p^m \left(\frac{2r^2}{w(z)^2} \right) \exp \left(-ik \frac{r^2}{2q(z)} + im\theta \right), \quad (2.2)$$

where $\delta_{0m} = \begin{cases} 1 & \text{if } m = 0 \\ 0 & \text{if } m \neq 0 \end{cases}$ is the Kronecker's delta, $\varphi(z) \equiv \tan^{-1} \left(\frac{z}{z_R} \right)$ the phase angle,

$q_z \equiv z + iz_R$ the complex radius and $w(z) \equiv w_0 \sqrt{1 + \left(\frac{z}{z_R} \right)^2}$ the spot size, $z_R \equiv \frac{\pi w_0^2}{\lambda}$ the

Rayleigh length, and w_0 the minimum spot size. In the solution the L_p^m functions are the

associated Laguerre polynomials given by $L_p^m(x) = \sum_{k=0}^p (-1)^k \frac{(p+m)!}{(p-k)!(m+k)!k!} x^k$.

This family of solutions, called the Laguerre-Gaussian modes (LG_{pm}), provide a complete basis for expanding an arbitrary optical beam in free space. The integer $p \geq 0$ is the radial index and m is the azimuthal mode index. There are p nodes for $m = 0$ and $p+1$ nodes for $m > 0$. Laguerre-Gaussian modes with $p = 0$ and $m > 0$ have only one zero at

the propagation axis ($r = 0$) and are called donut modes. The phase of LG_{pm} modes with $m > 0$ depends on the azimuthal angle (θ), which enables the donut modes (LG_{0m} modes) to preserve the dark cores.

An alternative set of solutions in rectangular coordinates are called Hermite-Gaussian modes. These two sets are equally valid, but LG modes are more convenient for problems with cylindrical symmetry. It is readily noticed in the solutions that the amplitude profiles remain unchanged in shape at any z , though the transverse scale ($w(z)$) changes. Optical beams that do not maintain their shapes as they propagate are expressed in linear combination of LG or HG modes.

The lowest LG mode (LG_{00}) is the same as and usually referred to as the TEM_{00} Gaussian mode. The radial intensity of the Gaussian mode is given by:

$$I_{00}(r) = \frac{2P}{\pi w(z)^2} e^{-2r^2/w(z)^2}, \quad (2.3)$$

where $P = \iint |u|^2 dx dy$ is the total power. The LG_{01} mode is the same as the TEM_{01}^* donut mode:

$$I_{01}(r) = \frac{4P}{\pi w(z)^4} r^2 e^{-2r^2/w(z)^2}. \quad (2.4)$$

TEM_{01}^* is not a pure mode but a combination of the TEM_{01} and TEM_{10} modes in rectangular coordinates.

The intensity profiles for several low order LG_{0m} modes are given in Fig. 2.1. In the first order donut mode beam the intensity is maximized at $r = w/\sqrt{2}$, where the intensities of TEM_{01}^* mode are equal to that of TEM_{00} mode. The higher order LG_{0m} modes have larger peak-to-peak diameters and steeper walls, allowing minimal interaction between the atoms and the light for atoms confined in the hollow core [25].

2.2 Scattering Force and laser cooling

When an atom absorbs (plus signs in Eq. 2.5 and 2.6 below) or emits (minus signs) a photon with a wave vector \vec{k} and frequency ν , momentum and energy conservation demand:

$$m\vec{v} \pm \hbar\vec{k} = m\vec{v}' \quad (2.5)$$

$$\frac{1}{2}mv^2 \pm h\nu = \frac{1}{2}mv'^2 \pm h\nu_0, \quad (2.6)$$

where m is the mass of the atom, \vec{v} and \vec{v}' the velocities before and after absorption (emission), $h = 6.63 \times 10^{-34}$ J·s Planck's constant and $h\nu_0$ the energy of the internal transition of the atom. This momentum transfer produces a force on the atom, called the spontaneous scattering force [26]. The scattering force is the momentum transferred per photon absorption ($\Delta p = \hbar k$) times the rate at which the photons are absorbed (R_a). The photon absorption rate can be obtained by considering the dipole transition between energy levels.

The state vector of a two-level the atom can be written as:

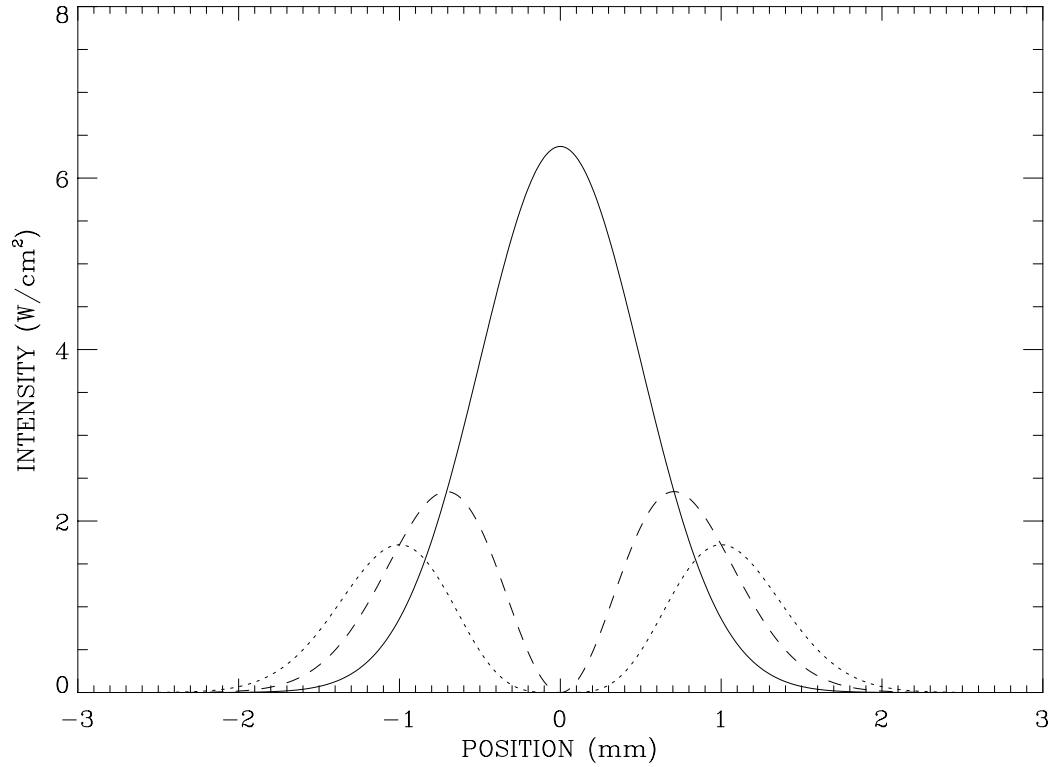


Figure 2.1 Intensity profiles of some low order LG_{0m} modes: LG_{00} (solid curve), LG_{01} (dashed curve) and LG_{02} (dotted curve). The total power is 100 mW, and the size is $w = 1$ mm. Higher order LG_{0m} donut modes have larger peak-to-peak diameter and lower peak intensity.

$$|\Psi(t)\rangle = a_1(t)e^{-itE_1/\hbar}|1\rangle + a_2(t)e^{-itE_2/\hbar}|2\rangle, \quad (2.7)$$

where $|1\rangle$ and $|2\rangle$ are the ground and excited state vectors with unperturbed energy E_1 and E_2 respectively. If the atom makes a spontaneous transition from the excited state to the ground state with lifetime τ , the upper state population $|a_2|^2$ decays as $\exp(-t/\tau)$ in the absence of the external field. When the atom is in an electric field $\vec{E}_0 \cos(\omega t)$, the rate equations for coefficients a_1 and a_2 are given by:

$$\begin{aligned} \frac{\partial a_1}{\partial t} &= \frac{i\Omega}{2} e^{i(\omega-\omega_0)t} a_2 + \frac{\gamma}{2} a_2 \\ \frac{\partial a_2}{\partial t} &= \frac{i\Omega}{2} e^{-i(\omega-\omega_0)t} a_1 - \frac{\gamma}{2} a_2 \end{aligned}, \quad (2.8)$$

where $\Omega = \frac{\langle 1|e\vec{x} \cdot \vec{E}_0|2\rangle}{\hbar}$ is the Rabi frequency, $\omega_0 = \frac{E_2 - E_1}{\hbar}$ the resonance frequency, $\gamma = 1/\tau$ the transition rate. The last terms, $\pm \frac{\gamma}{2} a_2$ were added to include the spontaneous transition. The absorption rate is the ratio between the time that the atoms spend in the upper state and the upper state lifetime. From the solutions to Eq. 2.8, the absorption rate is given by [27, 28]:

$$R_a \equiv \frac{|a_2|^2}{\tau} = \frac{\pi\Gamma I/I_s}{1 + I/I_s + 4(\Delta/\Gamma)^2}, \quad (2.9)$$

where $\Gamma = 1/(2\pi\tau)$ is the natural linewidth of the transition, I the intensity of the laser, $I_s = \frac{4\pi^2 hc\Gamma}{6\lambda^3}$ the saturation intensity and $\Delta = \nu - \nu_0$ the frequency detuning. The laser intensity is related to the Rabi frequency by $I/I_s = 2\Omega^2/\gamma^2$. There is sometimes confusion in the use of Γ and γ , ν and ω that are connected by factor of 2π . To avoid confusion, angular frequencies (γ , ω) will not be used in this thesis from now on. The I/I_s term in the denominator was introduced to include saturation in the absorption at high intensity. If the laser intensity is high enough, the spontaneous decay from the upper state is not fast enough to dissipate the absorbed energy and the absorption becomes saturated. As a result, the linewidth of the spectral distribution is broadened by $\Gamma \rightarrow \Gamma\sqrt{1 + I/I_s}$ for high intensity, which is called the power broadening [29].

Equation 2.9 is valid only for an atom that is stationary. Taking the Doppler shift ($\approx v/\lambda$) of the laser frequency for an atom moving with velocity \vec{v} into account, the scattering force is written as:

$$\vec{F}_{sc} \equiv \frac{\Delta p}{\Delta t} = \hbar\vec{k} \cdot \frac{\pi\Gamma I/I_s}{1 + I/I_s + 4\left(\frac{\Delta \pm v/\lambda}{\Gamma}\right)^2}, \quad (2.10)$$

where the positive (negative) sign corresponds to co-propagating (counter-propagating) photons. One readily available application of this scattering force is to control the drift velocity of a group of atoms by irradiating them with laser light [30, 31, 32, 33, 34]. The

atoms can be either slowed down or sped up depending on the direction of the beam relative to their momentum. The acceleration to which an atom is subject is given by:

$$a_{sc} = v_{rec} \cdot \frac{\pi \Gamma I / I_s}{1 + I / I_s + 4 \left(\frac{\Delta \pm v / \lambda}{\Gamma} \right)^2}, \quad (2.11)$$

where v_{rec} ($= \hbar k / m$) is the recoil velocity. When atoms are accelerated, the scattering rate changes due to Doppler shifting of the resonance. Eventually, the atoms can no longer absorb the light, and therefore all have the same terminal velocity. This leads to a nearly mono-energetic atomic beam whose energy spread is determined by spontaneous emission, as will be explained in section 2.3.

Fig 2.2 shows the drift velocity of ultracold atoms from a MOT as a function of the distance they travel under the scattering acceleration for some values of intensity and detuning of the kicker. The plot shows that the drift velocity increases at a lower rate as the atoms travel farther. The drift velocity 20 cm away from the MOT ranges from ~10 m/s to ~40 m/s for the given parameters. If a highly saturated beam ($I/I_s \gg 1$) on resonance ($\Delta = 0$) is used for the kicker, the drift velocity will be ~100 m/s.

Another important application of the scattering force is to reduce the speed of atoms moving in an arbitrary direction, which is called laser cooling [26, 35]. For simplicity, consider the one-dimensional motion of an atom in a pair of counter-propagating laser beams as shown in Fig. 2.3. The frequency of the laser is below the resonance frequency of the atomic transition. The atom then sees the frequency of the

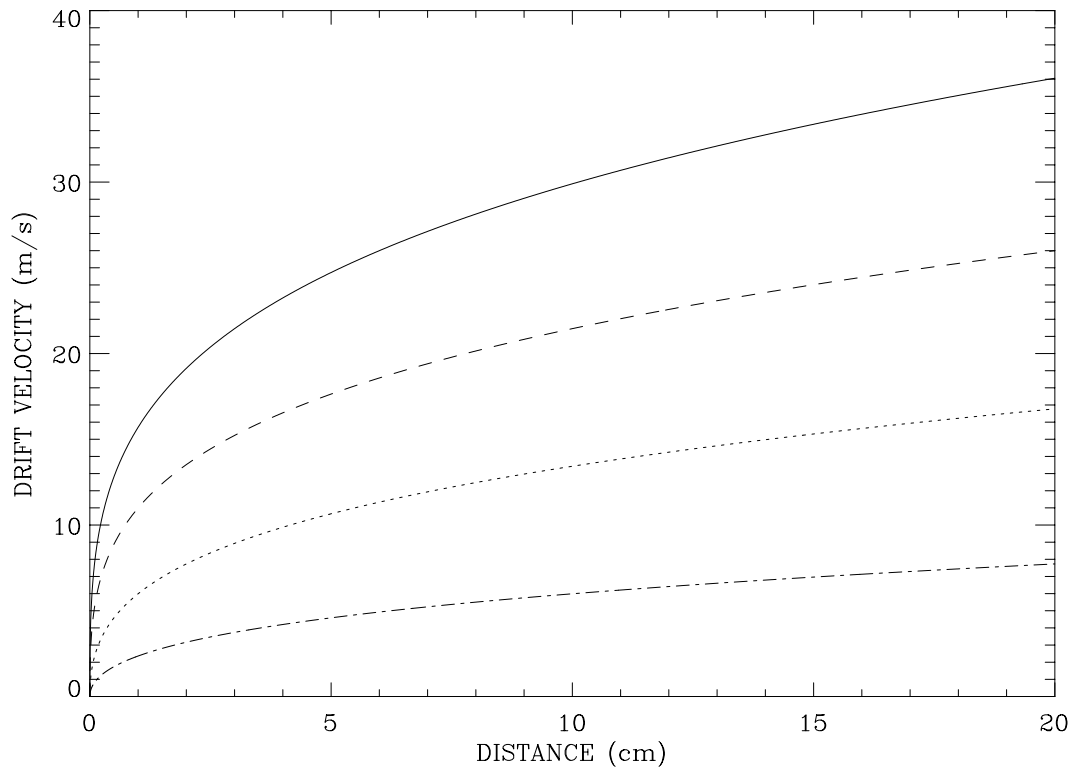


Figure 2.2 The drift velocity as a function of distance for various intensity and detuning of the kicker: $I/I_s = 10$, $\Delta = 0\Gamma$ (solid curve), $I/I_s = 3$, $\Delta = 0$ (dashed curve), $I/I_s = 1$, $\Delta = 2\Gamma$ (dotted curve), and $I/I_s = 0.1$, $\Delta = 2\Gamma$ (dot-dashed curve).

co-propagating photons red-shifted farther away from resonance, while seeing that of the counter-propagating photons blue-shifted closer to resonance. Therefore, the atom will absorb more counter-propagating photons than co-propagating photons. So regardless of the direction in which the atom moves, it will be slowed. By employing three orthogonal pairs of counter-propagating laser beams, Chu *et al.* demonstrated ‘optical molasses’ in three dimension [26]. The laser cooled atoms are not confined in space since the cooling force is not position dependent. If a magnetic potential is applied around the optical molasses, the laser cooled atoms can be trapped in space, as will be discussed in Ch. 4, which is called a magneto-optical trap (MOT) [1].

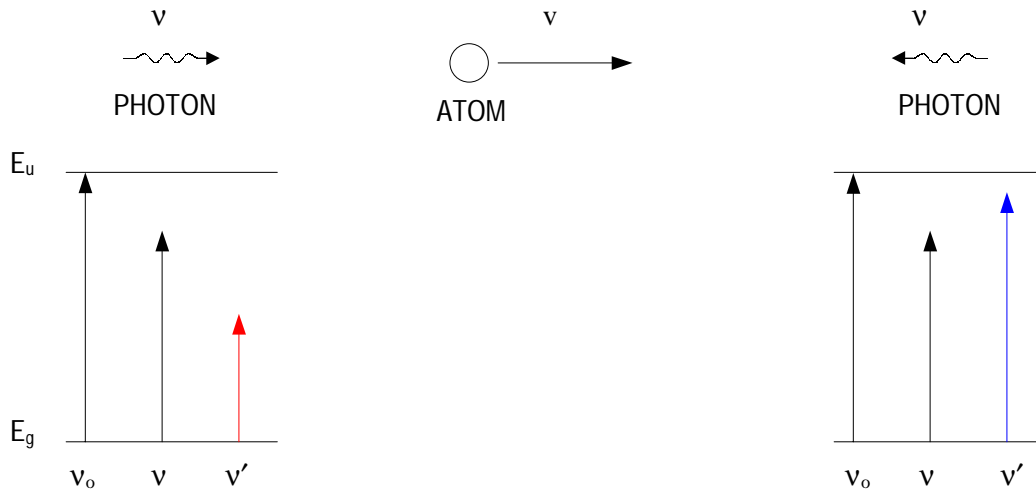


Figure 2.3 Principle of laser cooling. The frequency of co-propagating photons is red shifted away from resonance, while that of counter-propagating photons is blue shifted closer to resonance. ν_0 = resonance frequency of the atomic transition, ν = laser frequency, ν' = Doppler shifted laser frequency seen by the atom.

2.3 Optical heating and cooling limits

While absorption transfers momentum to the atoms in the direction of laser propagation, the subsequent spontaneous emission leads to a spread in the energy and momentum distributions in all directions. The spread can be modeled as a random walk process, which is a standard approach to collision problems in statistical mechanics [36]. Consider a random walk where each successive step increases or decreases the velocity by v_{rec} ($=\hbar k / m$, recoil velocity). After N such steps, the mean velocity of an ensemble of atoms will be $\langle \bar{v} \rangle = 0$, as expected since the emission is isotropic. However, the distribution of the velocities is not zero. It is given by $\delta v \equiv \sqrt{\langle v^2 \rangle} = \sqrt{(\delta v_0)^2 + N v_{rec}^2}$ where $\delta v_0 \equiv \sqrt{\langle v_0^2 \rangle}$ is the initial velocity spread. Then the kinetic energy distribution will be $\delta K \equiv m(\delta v)^2 / 2 = \delta K_0 + N K_{rec}$ where $K_{rec} = (\hbar k)^2 / 2m$ is the recoil energy of a photon emission. If the number of absorptions per unit time is R_a , as in Eq. 2.9, we can write a rate equation for the kinetic energy spread as:

$$\frac{d\delta K}{dt} = R_a K_{rec}. \quad (2.12)$$

The temperature of an ensemble of atoms is governed by its velocity distribution:

$\frac{3}{2} k_B T = \frac{1}{2} m \delta v^2 (= \delta K)$. The effect of the random emission is essentially to increase the temperature of the atoms, i.e., optical heating. This heating limits the temperature of the optical molasses. The equilibrium temperature of an optical molasses will be determined

at the point where the cooling rate ($d\delta K/dt = \vec{F} \cdot \vec{v}$) becomes equal to the heating rate given in Eq. 2.12. For the two-level atoms, Eq. 2.10 and 2.12 lead to:

$$k_B T = \frac{h\Gamma}{2} \cdot \left(\frac{1 + I/I_s + 4(\Delta/\Gamma)^2}{8|\Delta|/\Gamma} \right). \quad (2.13)$$

Under the optimum condition ($I \ll I_s$, $|\Delta| \approx \Gamma/2$), Eq. 2.13 gives a minimum temperature of $h\Gamma/2$, the Doppler limit. But the temperature measured in optical molasses is sometimes substantially lower than this limit [37, 38, 39]. This excessive cooling was explained by Tannoudji and Dalibard [40] and Chu [41], who realized that the atom was not a two-level system. The ground state has several quantum levels. The ground state sub-levels split, depending on the ‘spatially changing’ polarization of the cooling beam, forming periodic potential hills. The atoms lose their kinetic energy as they climb the periodic potential hills. Accordingly, this cooling mechanism was named polarization gradient cooling or Sisyphus cooling. In this model the temperature decreases as the detuning increases ($T \sim 1/\Delta$), different from Eq. 2.13.

In optical traps or guides, the atoms are heated as long as they are in the light. This optical heating limits the trapping time or guiding distance unless the resonance scattering rate is substantially reduced. The use of donut modes or hollow core laser beams has attracted interest because of their ability to allow minimum interaction between the atoms and the light as the atoms stay in the dark core.

2.4 Dipole interaction

Another fundamental force that an atom feels in a laser field is a dipole force related to the intensity gradient of the laser beam. This dipole force comes from the interaction between the induced dipole moment of the atoms and the inhomogeneous light field. When a two-level atom is in a laser field, the energy of states $|1\rangle$ and $|2\rangle$ is shifted by the so-called AC Stark effect. Since the energy shift depends on the field strength, the atom will feel a position dependent force by the field gradient. Whereas the scattering force is not conservative, the dipole force is conservative. Consequently the dipole force can be used to localize the atoms in space.

The dipole potential that produces the dipole force is given by [27, 28]:

$$U(\vec{x}) = \frac{h\Delta}{2} \cdot \ln\left(1 + \frac{I(\vec{x})/I_s}{1 + 4(\Delta/\Gamma)^2}\right), \quad (2.14)$$

where $I(\vec{x})$ is the position dependent laser intensity. The Doppler shift in the detuning is omitted purposely in Eq. 2.14 since the detuning is usually much larger than the Doppler shift when the dipole force is important. The dipole potential can be either positive or negative, depending on the sign of the detuning Δ . As shown in Fig. 2.4, when the laser is red detuned ($\Delta < 0$), the atoms are attracted toward the intense part of the laser beam. Therefore to confine the atoms with Gaussian mode laser beam, one needs to detune the laser frequency to the red of resonance. To confine atoms with donut mode or hollow laser beams, the laser should be detuned to the blue of resonance ($\Delta > 0$). Bjorkholm *et al.* [42, 43] focused a sodium atomic beam with a Gaussian mode detuned several GHz to

the red of resonance. They pointed out that the minimum spot size was limited by the optical heating, because the atoms spend most of their time in the most intense part of the laser beam. As an alternative, the use of a donut mode or TEM_{01}^* mode was proposed [44, 45, 46] to reduce the heating since the atoms spend most of their time in the dark or low intensity portion of the beam.

For a given laser intensity the potential depends on the detuning as in Fig. 2.5. The detuning that maximizes the potential can be obtained by solving $dU / d\Delta = 0$ and is given by:

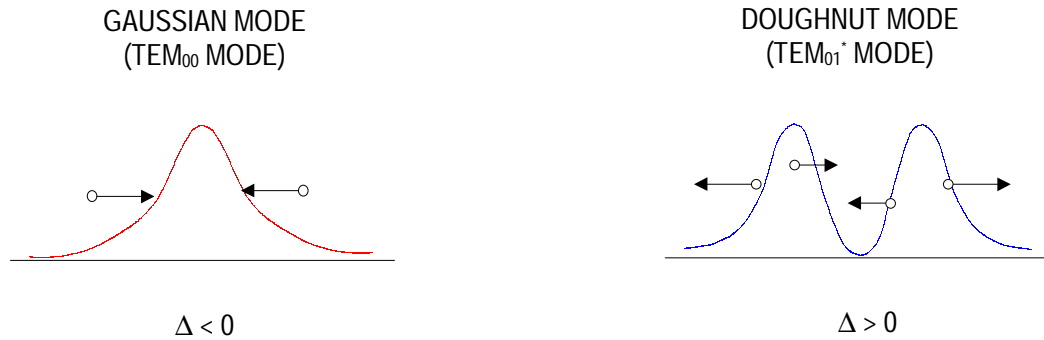


Figure 2.4 Focusing with dipole potential for Gaussian and Doughnut modes. To confine the atoms near the center, Gaussian mode must be red detuned whereas the Doughnut mode must be blue detuned. The potential shape is determined by the laser intensity profile and detuning.

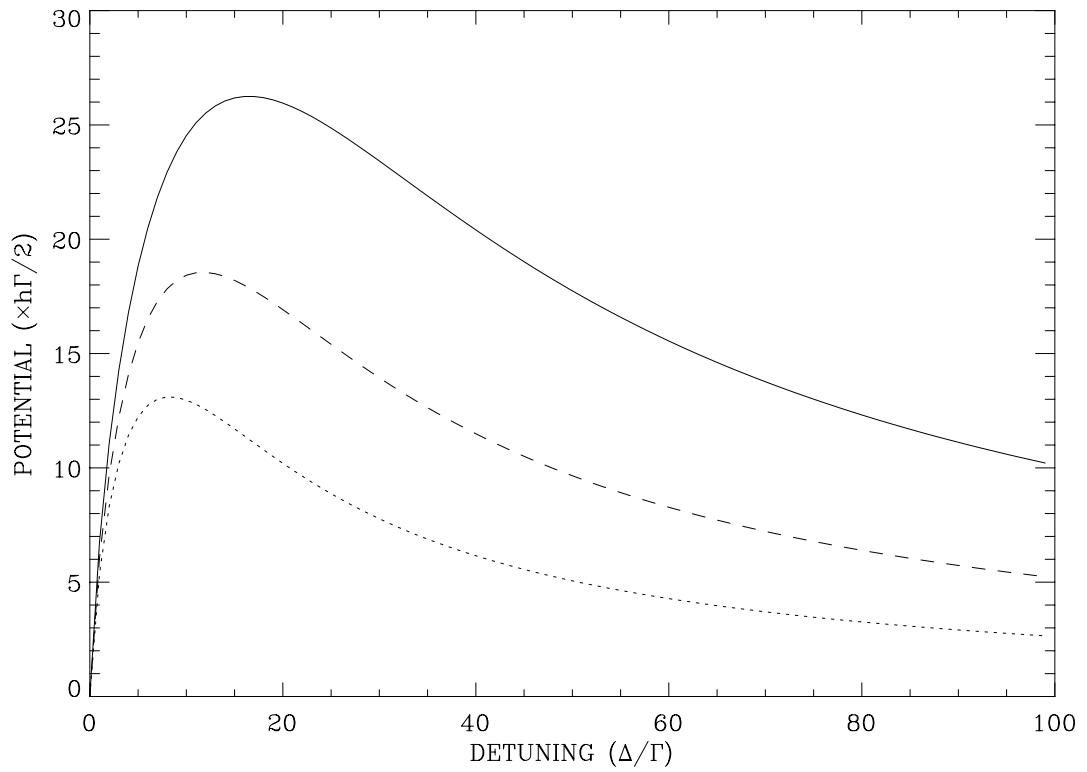


Figure 2.5 Dipole potential for TEM_{01}^* mode as a function of detuning with different total powers of the laser beam: 200 mW (solid curve), 100 mW (dashed curve) and 50 mW (dotted curve). The size of the beam is $w = 1$ mm. The potential increases linearly with Δ for small detunings and decreases inversely proportional to Δ for large detunings.

$$\Delta_0 \approx \frac{\Gamma}{4} \sqrt{\frac{I}{I_s}}. \quad (2.15)$$

In most practical cases, the potential at this detuning is high enough to confine ultracold atoms. This detuning, however, may not be the ‘optimum’ detuning for operation of an atom trap or guide. The scattering rate at the detuning of Δ_0 (\sim tens of MHz) is not negligible when the atoms are confined in the potential for a long time. This is especially true in TEM_{01}^* mode where the atoms experience zero intensity only at the center ($r = 0$). As discussed in section 2.3, scattering increases the kinetic energy spread of the atoms. Therefore, both the potential height and scattering rate should be considered in determining the optimum detuning for long trap times or long distance guides. For typical laser intensities (tens of milliwatts \sim several watts), the optimum detuning is much larger than Δ_0 . At large detunings ($\Delta \gg \Delta_0$), the potential can be approximated as:

$$U(\vec{x}) = \frac{h\Gamma}{2} \cdot \frac{I/I_s}{4\Delta/\Gamma}. \quad (2.16)$$

The shape of the dipole potential is exactly the same as the shape of the laser intensity profile since the potential is proportional to the laser intensity. Note that the first factor in Eq. 2.16, $h\Gamma/2$, is the Doppler limit as explained in section 2.3. To confine ultracold atoms with temperature near the Doppler limit with blue detuned donut modes, the

second factor in Eq. 2.16 must be larger than unity. Therefore, to confine the ultracold atoms for a long time, the optimum detuning must be chosen such that:

$$\frac{\Gamma}{4} \sqrt{\frac{I}{I_s}} < \Delta < \frac{\Gamma}{4} \frac{I}{I_s}. \quad (2.17)$$

More details on the optimum detuning will be discussed in Ch. 5.

CHAPTER 3

EXPERIMENTAL APPARATUS

This chapter describes the apparatus used in my study, including the laser sources, the vapor cells for saturated absorption spectroscopy, the vacuum chamber, and the optical delivery system. The overall experimental setup is shown in Fig. 3.1. The most important components are the diode lasers used for trapping and guiding the ultracold atoms. Section 3.1 describes the characteristics of the diode lasers, their mechanical mounting, electronic controlling and external cavities. The laser beams are frequency locked with the saturation absorption spectroscopy as described in section 3.2. The laser beams are then delivered to the interaction region through the optical components and shutters described in section 3.3. I discuss the vacuum chamber and pumping in section 3.4.

3.1 Diode lasers

In my experiments, three GaAlAs diode lasers were used: two 50 mW diodes (model #: SDL-5400-C from Spectral Diode Labs) for the trapper and the repumper and a 100 mW diode (model #: SDL-5410-C) for the guiding hollow beam. Diode lasers have become popular laser sources in atomic physics because of their reliability, tunability, narrow bandwidth as well as low price. However, diode lasers are sensitive to changes in the operational environment (temperature, injection current and mechanical and acoustic vibration) and can be subject to a large FM noise. Therefore, the

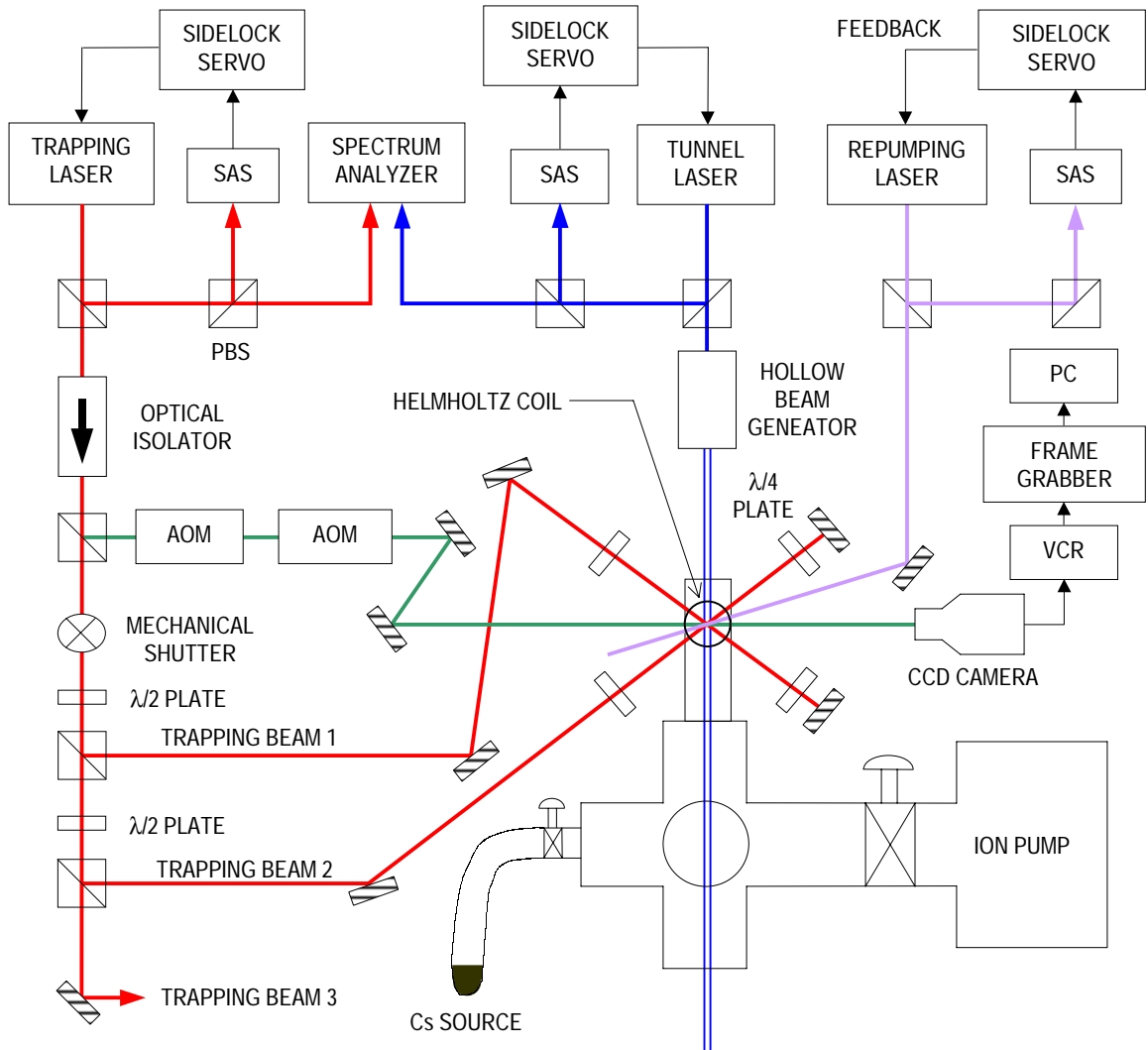


Figure 3.1 Overall experimental setup. The lenses are not shown. See Ch. 5 for a description of the hollow beam generator. The direction of the trapping beam 3 is perpendicular to the paper at the glass cell. The cubes are polarizing beam splitters (PBS). The lasers are controlled by the saturated absorption spectrometers (SAS). The frequency of the probe beam (the beam that goes to the camera) is shifted to resonance frequency by acousto-optic modulators (AOM).

application of diode lasers requires good mechanical isolation, thermal insulation and frequency stabilization.

3.1.1 Mechanical mounting and collimating optics

The diode lasers from the manufacturer typically come in small packages and need to be mounted for operation. Our laser diodes were mounted on homemade aluminum mounting blocks that also served as heat sinks. Since laser diodes are very sensitive to electrostatic discharge, grounding wrist straps are required for safe handling. To avoid voltage spikes that can easily kill the laser diodes, three forward biased diodes and a backward biased diode were connected in parallel across the positive and negative laser diode input leads. Any voltage exceeding 2.4 V in the forward direction and 0.8 V in the reverse direction is bypassed.

The output beam from the laser diode diverges with large angles ($\theta = 30^\circ$ and 10° in direction perpendicular and parallel to the polarization respectively) and needs to be collimated as shown in Fig 3.2. A 5 mm focal-length lens with a 0.5 numerical aperture was placed in front of the diode. The lens mounting block was designed to allow precise positioning, which was important for having a beam without astigmatism. The lens mount was shimmed when necessary for height adjustment. The diode mount and the lens mount were screwed down onto a base plate made of a 0.5" thick aluminum plate as in Fig. 3.2. The slot between the diode mount and the lens mount was cut to allow precision adjustment for the beam collimating. The base block was fastened to the bottom plate of an aluminum enclosure. Several layers of rubber pad were inserted between the laser enclosure and the optical table for mechanical and electric isolation.

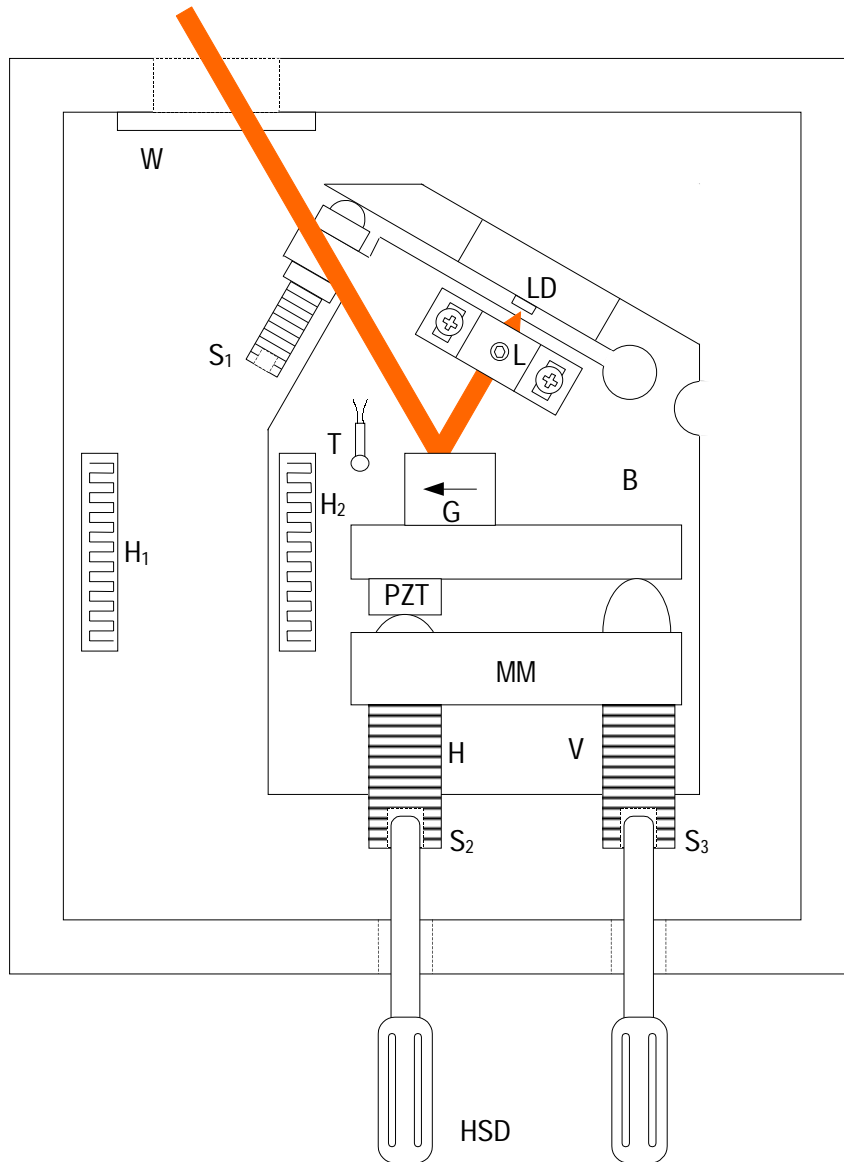


Figure 3.2 Schematic of the diode laser mount and housing. The diverging laser diode beam (LD) is collimated with the lens (L). The 1st order from the grating (G) goes back to the diode. The grating is tilted with the piezoelectric transducer (PZT) and two hex screw drivers (HSD). The housing is heated above room temperature but 2-3 degrees below the operating temperature with H₁. The temperature is stabilized with the thermistor (T) and a heater (H₂) on the base block (B). The whole housing is wrapped with styrofoam. This design is a modification of the design in Reference [50].

After collimation, the laser beam hits a grating that forms an external cavity with the back facet of the laser diode. The 1st order diffraction from the grating goes back to the diode, and the 0th order is coupled out. The grating is attached on a mirror mount. A piezoelectric transducer (PZT, Model # AE0203D04 from Thor Labs) was inserted between the fixed face and the movable face to change the cavity length. The PZT was used for fine tuning; two screws served for coarse tuning. The original thumbscrews on the mirror mount were replaced with hex screws to allow access from outside the laser housing.

3.1.2 Temperature stabilization

Since diode lasers are sensitive to temperature change, it is necessary to stabilize the temperature. This was achieved by several stages of thermal isolation and feedback. The aluminum enclosures were placed in a plastic box in which the temperature was maintained 3-4 degrees above room temperature by a commercial on-and-off temperature controller. This minimized the effect of change in the room temperature. Each enclosure was wrapped with styrofoam to minimize heat exchange. The temperature inside the enclosures was set at 2-3 degrees below the operation temperature. When the laser had a free running wavelength shorter than the operating wavelength (this is true of the trapper and repumper), the enclosure was heated with a heating tape (H_1 in Fig. 3.2). When the free running wavelength is longer than the operating wavelength (this is true of the guiding laser), the enclosure was cooled with several thermoelectric coolers stacked in series and/or parallel. Finally a thermistor (T) and heater (H_2) pair stabilized the temperature of the base plate by electric feedback with a circuit shown in Fig. 3.3. Any

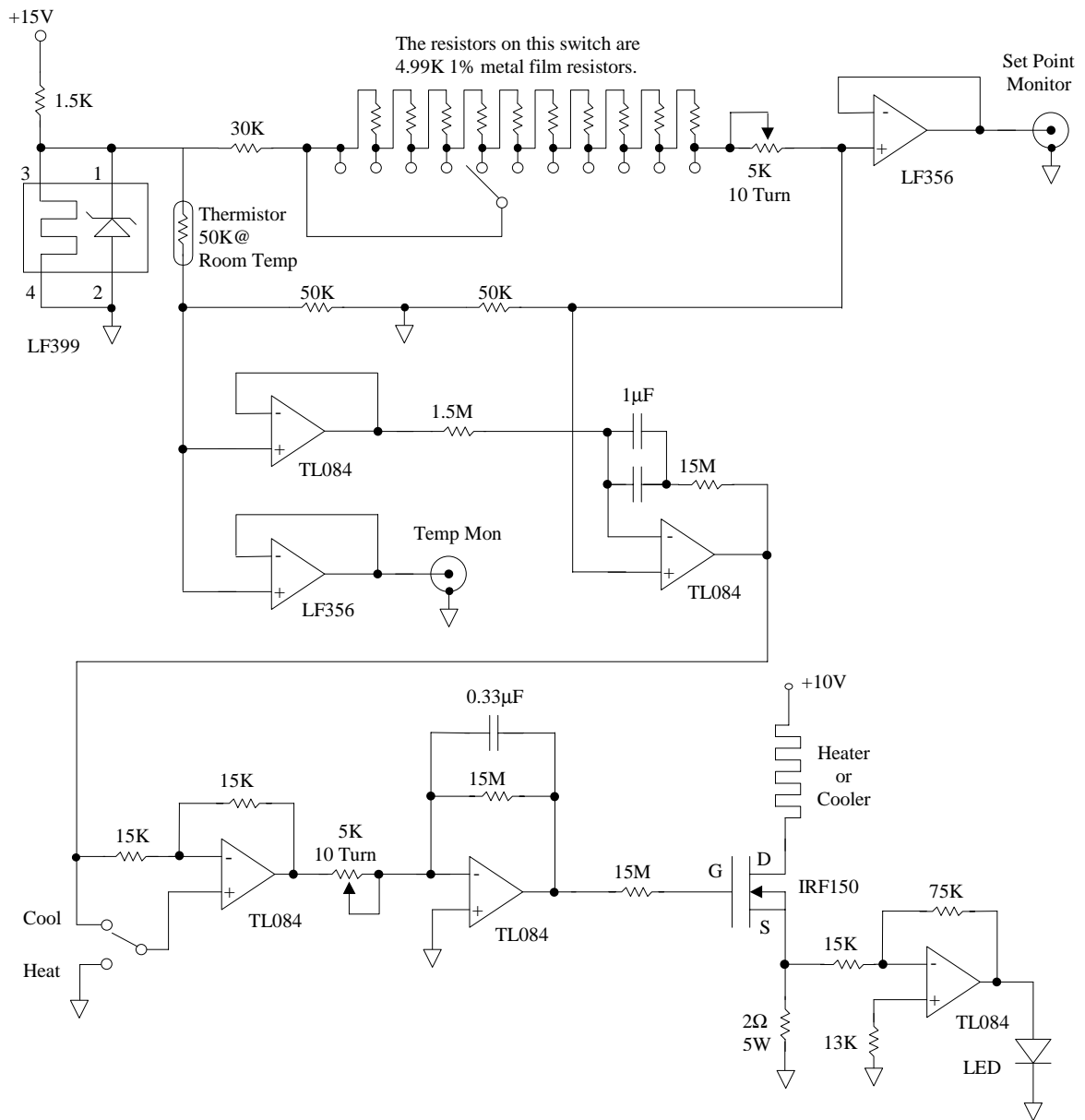


Figure 3.3 Temperature control circuit for the diode lasers. The voltage across the thermistor is compared with the set point voltage. The difference is amplified and used to turn on the power transistor (IRF150). The set point voltage is regulated by the temperature stabilized voltage reference (LF399). This design is the modification of the design in Reference [50].

temperature change detected by the thermistor was amplified and used to activate the heater. With this three-stage temperature stabilization, we could achieve the same saturated absorption spectrum every day without further tuning.

3.1.3 Tuning characteristics and external cavities

The frequency (or wavelength) of the diode laser is determined mainly by three factors: temperature, injection current and cavity mode. Changes in temperature change the index of refraction of the gain medium and thereby change the optical cavity length of the laser. The operation wavelength of the lasers in our experiment was around 852 nm with appropriate detuning. The off-the-shelf diodes from the factory had an uncertainty of ± 4 nm and had to be shifted several nanometers to reach the correct wavelength. This was accomplished by thermal tuning since the wavelength of the diodes changes by 0.3 nm per degree. The two MOT lasers had free running wavelengths below 852 nm and were heated. The guiding laser had a free running wavelength of about 854 nm and was cooled to 18 °C by using thermoelectric coolers. To set the desired wavelength, the wavelength was measured with a monochromator (coarse determination) and by a saturated absorption spectrum (fine determination) while the temperature was changed.

The injection current mainly changes the power by changing the carrier density. It also affects the potential depth of the p-n junction and shifts the gain curve. The dependence of the frequency on the current is about 7 GHz/mA. The final tuning of the frequency is achieved by control of the parameters of a cavity. The laser diode has its own internal cavity formed by front and back facets. The front facet has an anti-reflection (AR) coating with about 3 % reflectivity whereas the back facet is highly

reflective. Since the internal cavity is hard to control, an external cavity [47, 48, 49] was modulated to control the frequency.

The external cavity is formed by the back facet of the diode and a grating as shown in Fig. 3.4. Figure 3.4a shows the conventional Littrow configuration, where the 1st order reflection from the grating goes back to the diode; the 0th order is coupled out as an output. The grating used for our external cavity has 1200 lines per mm and is blazed for 500 nm. The optimal incident angle (θ_i) of the laser beam to the grating is determined by the grating equation, $a(\sin \theta_m - \sin \theta_i) = m\lambda$, where a is the spacing between the grooves (1/1200 mm in our case) and m is the diffraction order. The Littrow configuration occurs when $\theta_1 = -\theta_i$, which gives $\theta_i = 30^\circ$ for Cs resonance lines ($\lambda = 852$ nm). The power of the 0th order output depends on the blaze direction of the grating and the polarization of the laser beam. The arrow on the grating in Fig. 3.4a is for the low-feedback large-output case. The 0th order output power is maximized when the polarization of the beam is parallel to the grooves (vertically polarized) while the feedback is maximized when the beam is polarized perpendicular to the grooves (horizontally polarized). Using this configuration, we could couple out 50% of the laser power.

An enhanced design for the external cavity employs a polarizing beam splitter (PBS) for the output coupler as in Fig. 3.4b. There are two advantages in using the PBS over the previous version. First, more power can be coupled out. The amount of power reflected from the PBS depends on the polarization of the incident laser beam. The PBS reflects a vertically polarized beam while it transmits a horizontally polarized beam. The

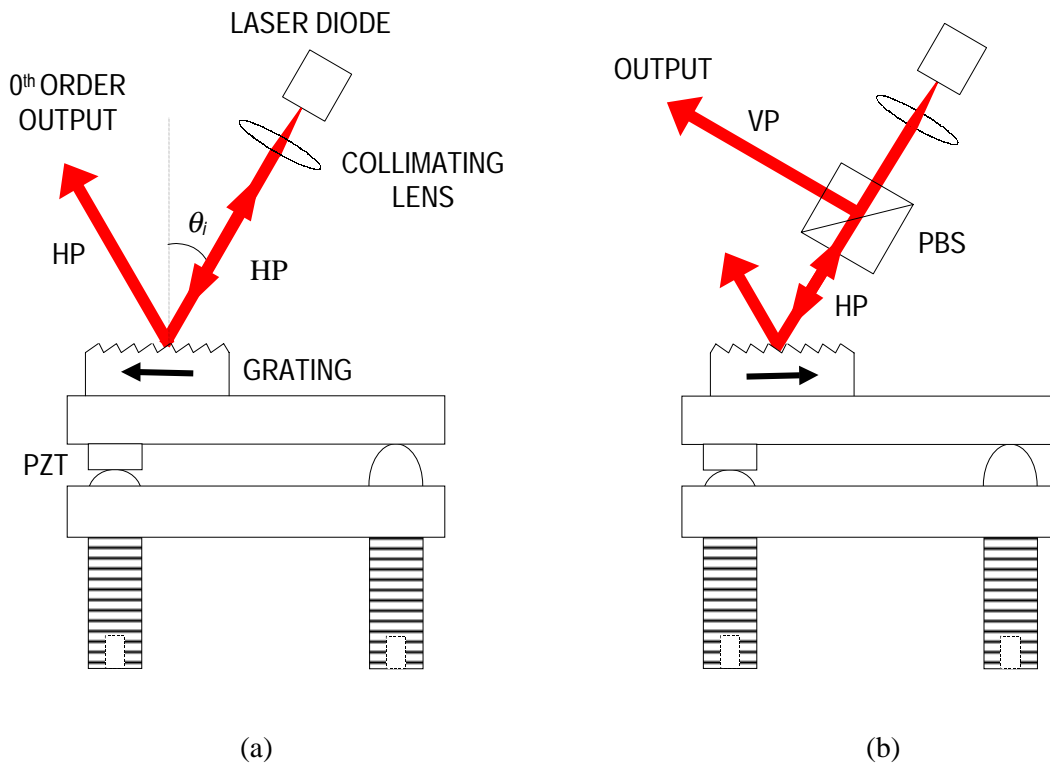


Figure 3.4 Two designs of the external cavity. (a) The 0th order diffraction from the grating is coupled out as an output. Incident angle to the grating is set to $\theta_i = \sim 30^\circ$ to have the 1st order feedback to the diode. The blaze direction is chosen to allow maximum power in the 0th order. The laser beam is horizontally polarized (HP). (b) The vertically polarized (VP) component is taken as an output from the polarizing beam splitter (PBS). The 0th order from the grating is lost while the 1st order reflects back to the diode. The blaze direction is chosen to allow maximum power in the 1st order. In both configurations, the laser is coarsely tuned with the hex screws on the mirror mount and fine tuned by the piezoelectric transducer (PZT).

output power, therefore, can be changed by rotating the polarization. This can be done either by using a half-wave plate or by rotating the laser diode itself on its mount. The maximum output available this way is limited by the efficiency of the feedback. The external cavity mode will be suppressed by the internal cavity mode if the feedback from the grating is too low. To enhance the feedback efficiency, a good collimation of the laser beam is required, since otherwise the feedback will not be focused properly into the laser diode. The blaze direction of the grating is also reversed to allow more power in the 1st order. Using this configuration we could couple out 80% of the free-running laser power as an output when about 10% was fed back to the diode from the grating. A second advantage is that the output beam does not move while the grating is rotated with the hex screwdrivers. In the previous version, all the consecutive optics had to be realigned when the grating was rotated.

The laser beam from our external cavity is diffraction limited and has a single longitudinal mode. Figure 3.5 shows the spectra from both the configurations explained above. The bandwidth of the external cavity laser is under 1 MHz [50]. In our experiment, the early version was used for the MOT trapping and repumping lasers. The new version was used for the tunnel laser.

When the laser with an external cavity is first turned on, its wavelength is measured with a monochromator. According to its free running wavelength, the diode is either heated or cooled until the desired wavelength is reached. It is very convenient to monitor the fluorescence with a vapor cell because it clearly indicates when the laser frequency is near resonance. Once the fluorescence can be seen, the injection current and the external cavity mode are varied to get the proper saturated absorption signal. If the

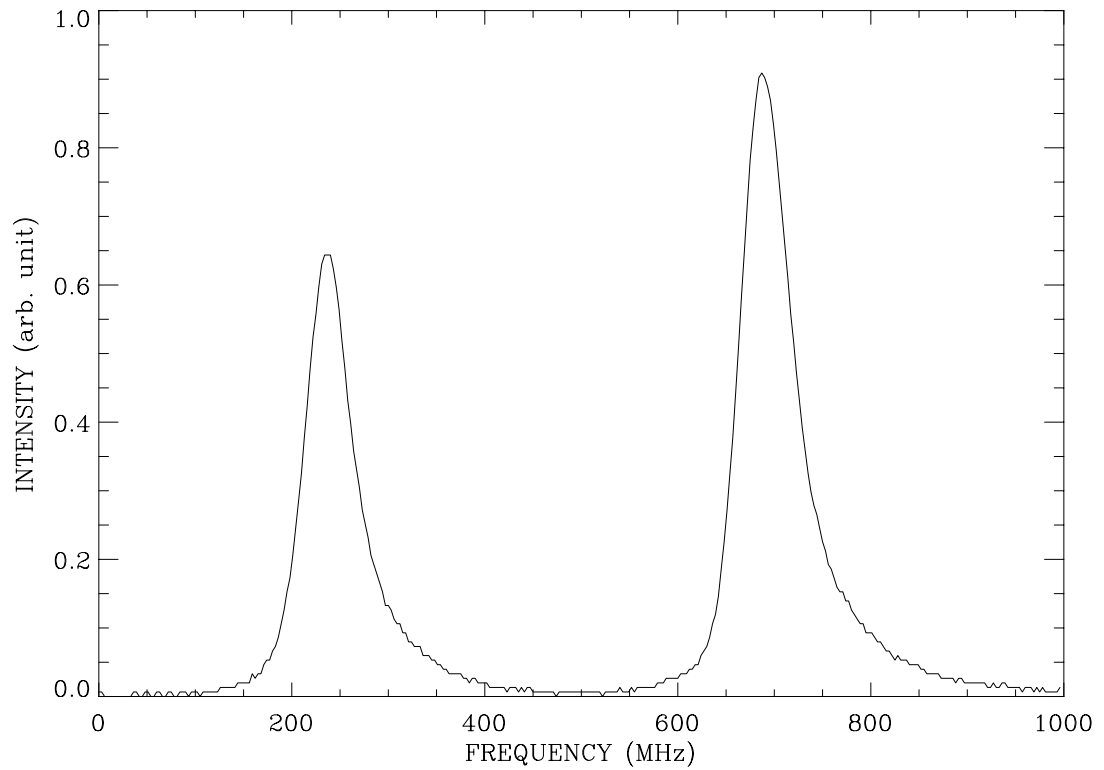


Figure 3.5 Spectra for the external cavity diode lasers. The peak on the left side is the MOT trapping beam generated by configuration (a) in Fig. 3.4. The peak on the right is the guiding laser generated by configuration (b) in Fig. 3.4. The spacing between the two peaks is set to 450 MHz. The laser bandwidth is typically under 1 MHz. The peaks shown here have FWHM of about 70 MHz because the resolution of the peaks is limited by the spectrum analyzer.

laser is not running with its maximum power when the right frequency is achieved, the temperature needs to be lowered while the current needs to be increased.

3.2 Saturated absorption spectroscopy and frequency locking

To cool and trap atoms, the trapping laser needs to be stabilized to within a natural linewidth of the transition. This frequency control was accomplished with saturated absorption spectroscopy. A small fraction (less than 1 mW) of the main output is directed to a glass vapor cell held at a pressure of $\sim 10^{-6}$ Torr as in Fig. 3.6. The weak reference beam (the beam to PD2 in Fig. 3.6) shows a Doppler broadened absorption signal. The probe beam, which overlaps the strong ($I > I_s$) saturating beam, experiences saturation near the hyperfine transition frequencies. The reason is that only zero velocity atoms are in resonance with both the probe beam and the counter-propagating saturation beam. Taking the difference between the probe and reference signals, Doppler broadening is removed. Fig 3.7 shows the Doppler-free saturated absorption signals for the Cs transitions,¹ $6^2S_{1/2}(F=3) \rightarrow 6^2P_{3/2}(F'=2,3,4)$ and $6^2S_{1/2}(F=4) \rightarrow 6^2P_{3/2}(F'=3,4,5)$. The frequency modulation was obtained by applying a triangular wave from a function generator on the PZT. The peaks marked by their transition are the hyperfine transitions. The unmarked peaks, known as crossover peaks, are located halfway between the three pairs of marked peaks. They appear because atoms with a certain velocity class can see the probe beam Doppler shifted into a hyperfine resonance, and the counter-propagating saturation beam shifted in opposite direction into another hyperfine resonance.

¹ See Ch. 4 for more information on the Cs transitions.

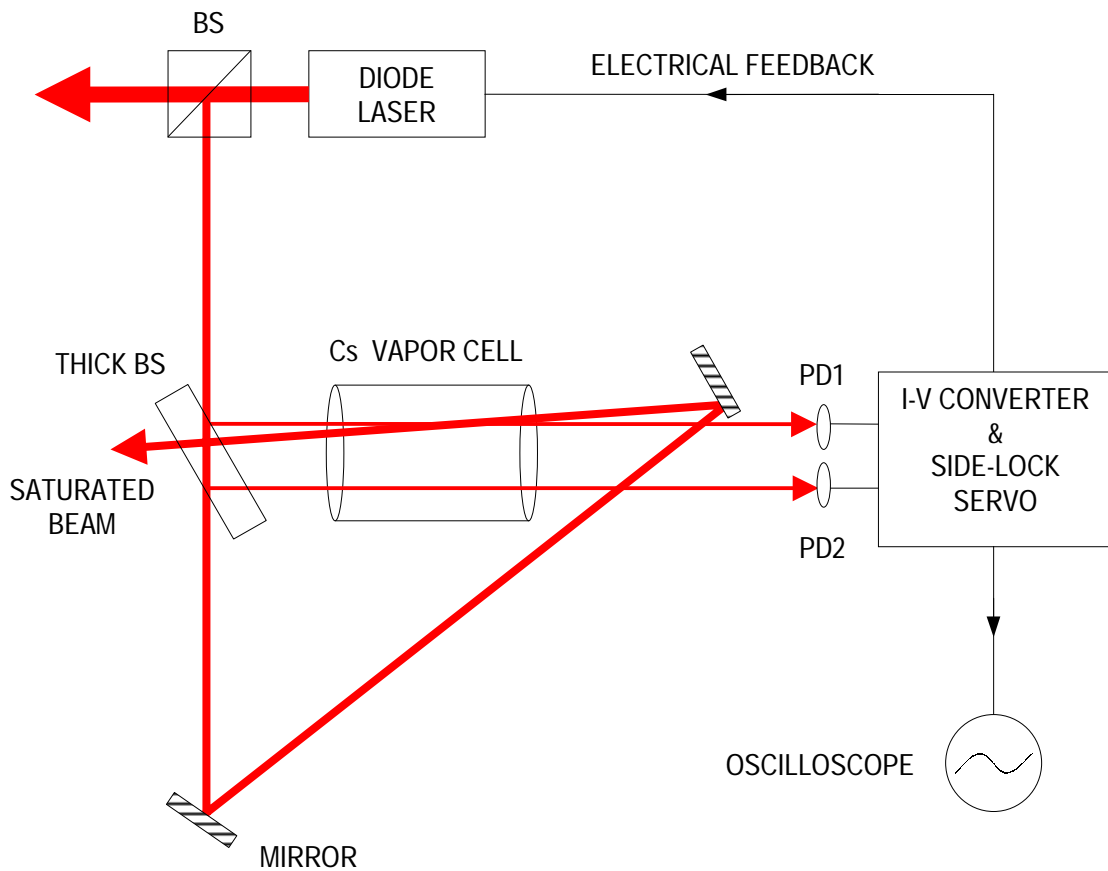


Figure 3.6 Saturated absorption spectroscopy arrangement. Two weak beams (split with a thick glass beam splitter) traverse the cell and produce absorption signals on two photo diodes. The strong beam overlaps one of the weak beams to burn holes at the resonance frequency. The signal to the oscilloscope is taken from the ‘SET POINT MON’ of the sidelock servo in Fig 3.8. The electric feedback signal drives the PZT when lock is on.

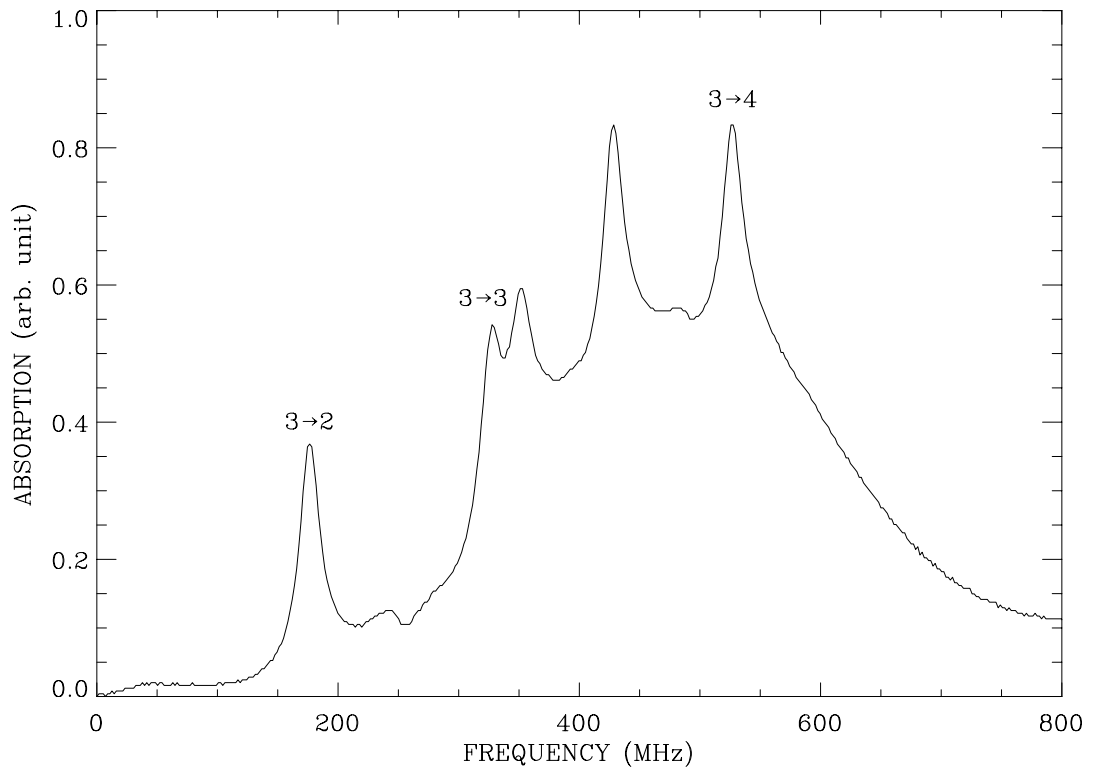


Figure 3.7a Saturated absorption signal for the $6^2S_{1/2}(F=3) \rightarrow 6^2P^o_{3/2}(F'=2,3,4)$ transition in a Cs atom. The diode laser frequency is ramped linearly by applying a triangular wave to the PZT. The spacings between the marked transitions are 150 MHz and 200 MHz from left to right. The unmarked peaks located between each of these three are ‘crossovers’. The repumping beam for a MOT is tuned to the $6^2S_{1/2}(F=3) \rightarrow 6^2P^o_{3/2}(F'=4)$ transition to pump the atoms optically back to the upper hyperfine state.

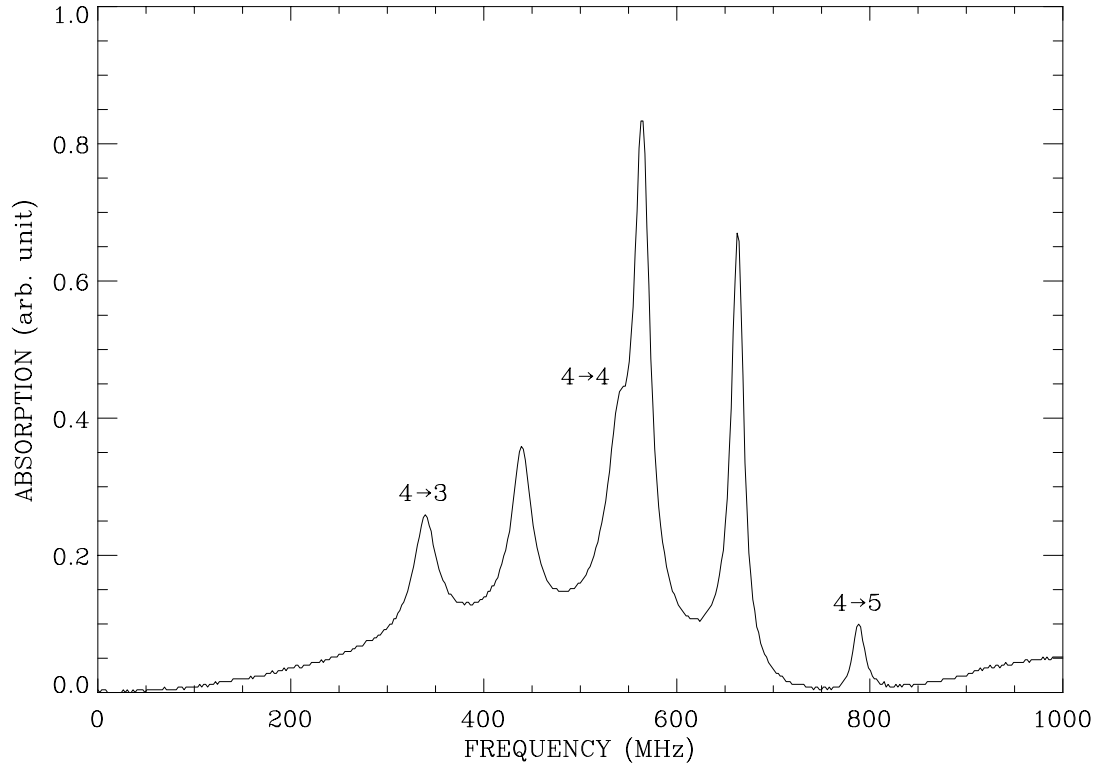


Figure 3.7b Saturated absorption signal for the $6^2S_{1/2}(F=4) \rightarrow 6^2P_{3/2}(F'=3,4,5)$ transition in a Cs atom. The spacings between the marked transitions are 200 MHz and 250 MHz from left to right. The Doppler broadening on which the absorption signals ride is removed by subtracting the two absorption signals as shown in Fig. 3.6. The MOT trapping beams are locked on the left side (red detuned) of the $6^2S_{1/2}(F=4) \rightarrow 6^2P_{3/2}(F'=5)$ transition.

After the appropriate transitions are found, the lasers are locked at the desired frequency with a sidelock servo as shown in Fig. 3.8. To lock the laser frequency, the SET POINT value is first set to the desired side of the absorption peak. The MOT trapping laser is locked to the red side of the $F=4 \rightarrow F'=5$ transition, typically by ~ 2 linewidths. The repumping laser is locked as close as possible (< 1 linewidth) to either side of the $F=3 \rightarrow F'=4$ transition. Then the triangular wave is turned off (using the RAMP IN switch in the circuit), and the frequency is brought to the set position by PZT BIAS. Closing PZT LOOP starts the feedback error signal (difference between the saturated absorption signal and the SET POINT voltage level) to the PZT. If the frequency drifts, an error signal develops and drives the PZT until the saturation signal returns to the set voltage.

3.3 Optical delivery of the laser beam.

3.3.1 Optical components

The laser beams from the diodes do not generally have the required shape and size for MOT generation. The collimated diode laser beams are highly elliptical while the required beams for MOTs are circular beams with about 1 cm diameter. Before the beam is delivered to the trap, it passes through a series of optical components to produce the necessary beam characteristics.

The very first optical element that the trapping beam passes is an optical isolator. The trapping beam needs to be accurately retroreflected as will be explained in Ch. 4, which provides optical feedback to the diode. Since a laser diode is extremely sensitive

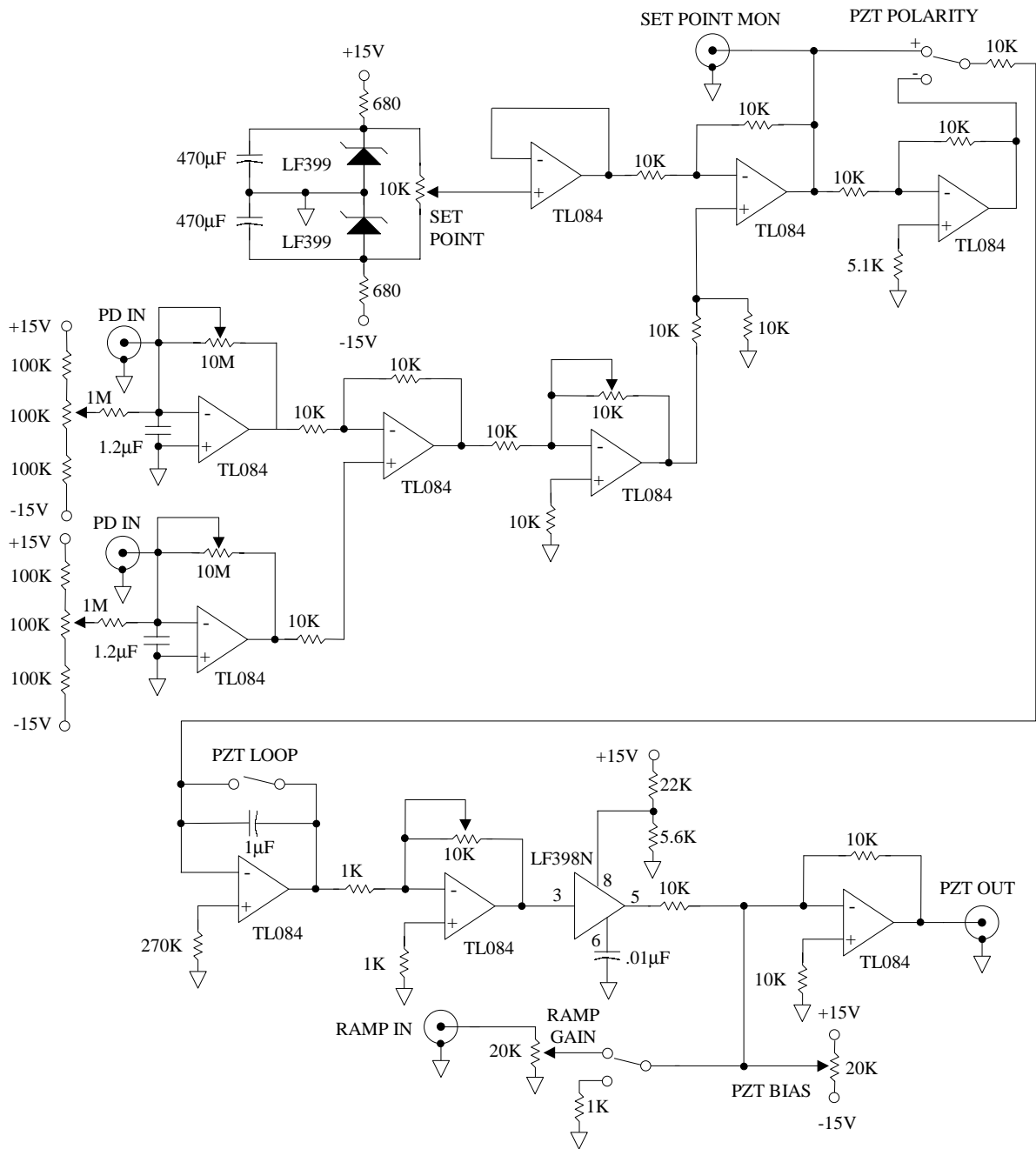


Figure 3.8 Circuit diagram for I-V converter and sidelock servo. When PZT LOOP is closed, the error signal (the difference between the SET POINT and the saturated absorption signal) drives the PZT to lock the frequency to the side of a saturated absorption feature.

to the optical feedback, all optical feedback should be removed with an optical isolator. The isolator consists of two elements, a linear polarizer and a Faraday rotator. The Faraday rotator rotates the polarization of the retroreflected beam perpendicularly to the polarization of the incident beam. The retroreflected beam that passed the Faraday rotator is extinguished by the polarizer by ~ 40 dB. The throughput loss is less than 5% when the beam is properly aligned and focused into the isolator.

A series of circular and cylindrical lenses were used to expand the beam to the desired size and shape. The MOT trapping beam is then split into three beams of equal power with half-wave plates and polarizing beam splitters as shown in Fig. 3.9. The half-wave plate divides an unpolarized incident beam into two orthogonal, linearly polarized components. When the incident beam is polarized, the power in the reflected and transmitted beams depends on the direction of the polarization. The three MOT trapping beams are then polarized circularly with quarter-wave plates to evoke $\Delta m_F = \pm 1$ transitions. Positive/negative (σ^+/σ^-) helicity² evokes $\Delta m_F = +1/-1$ transitions. A convenient way to understand how the wave plates change the polarization is to use Jones matrices as shown in Fig. 3.9. $\begin{pmatrix} 1 \\ 0 \end{pmatrix}$ and $\begin{pmatrix} 0 \\ 1 \end{pmatrix}$ represent polarization in the x and y

directions while $\begin{pmatrix} 1 \\ i \end{pmatrix}$ and $\begin{pmatrix} i \\ 1 \end{pmatrix}$ represent positive and negative helicity (or left and right circular polarization) respectively. The half-wave plate is represented by

² In most optics books, right (left) circularly polarized beam is defined as a beam whose \mathbf{E} vector rotates clockwise (counterclockwise), as seen by an observer toward whom the beam is moving. It has a negative angular momentum and is therefore σ^- (σ^+).

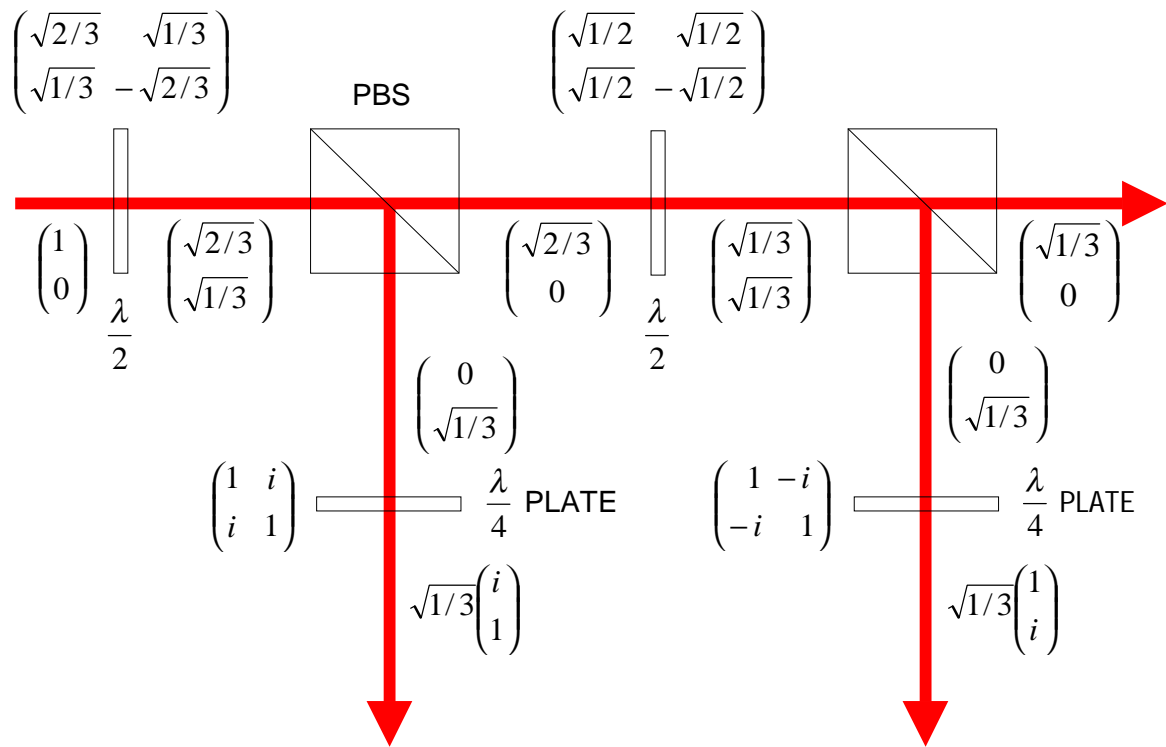


Figure 3.9 The wave plates and polarizing beam splitters. The two half wave ($\lambda/2$) plates have fast axes 17.6° and 22.5° respectively from the x (horizontal) axis from left to right. The two quarter wave ($\lambda/4$) plates have fast axes $+45^\circ$ and -45° respectively from left to right. This setup generates three right or left handed circularly polarized beams with the same power from a beam linearly polarized in x direction.

$\begin{pmatrix} \cos 2\theta & \sin 2\theta \\ \sin 2\theta & -\cos 2\theta \end{pmatrix}$ where θ is the angle of the fast axis relative to the x direction. The

two half-wave plates in Fig. 3.9 have $\theta = 17.6^\circ$ and 22.5° respectively. The second set of half-wave plate and beam splitter in Fig. 3.9 was replaced by a simple 50% silver-coated beam splitter in some of our experiments. The quarter-wave plate with its fast axis at

$\pm 45^\circ$ from x direction is represented by $\begin{pmatrix} 1 & \pm i \\ \pm i & 1 \end{pmatrix}$. The two quarter-wave plates in the

figure have the fast axis at $+45^\circ$ and -45° respectively, generating σ^- and σ^+ beams from vertically polarized beams. The linear polarization can change its direction when the beam reflects on mirrors at a tilted angle. Therefore the polarization direction should be checked before the directions of the quarter-wave plates are determined.

3.3.2 The shutters

Two types of shutters were used in our experiment to control the MOT trapping beams and the probe beam. A mechanical shutter (model # LS6 from Vincent Associates, 6 mm clear aperture) was used to turn on and off the MOT trapping beams. This shutter has a 0.8 ms 80% open and close time. Since the MOT trapping beam passes the shutter before it is expanded, the actual on and off time is substantially reduced. With about 1 mm size of the beam, the 80% on and off time was about 0.1 ms. The shutter toggles open and close on the falling edge of a TTL pulse. The response time to the TTL pulse generator is about 2 ms.

A pair of acousto-optic modulators (AOM) were employed to control the probe beam. An AOM is an optically transparent crystal in which a phase grating is formed by the propagation of an acoustic wave. The beam that passes the crystal at a critical angle

Bragg diffracts off the phonons in the crystal. The frequency shift of the first order Bragg mode is determined by the frequency of the acoustic wave. As much as 75% of the incident power can be directed into one of the first orders (negative and positive) when the incident beam is focused into the 1 mm crystal. The probe beam that was used to monitor the trapped atoms was split from the MOT trapping beam with a half-wave

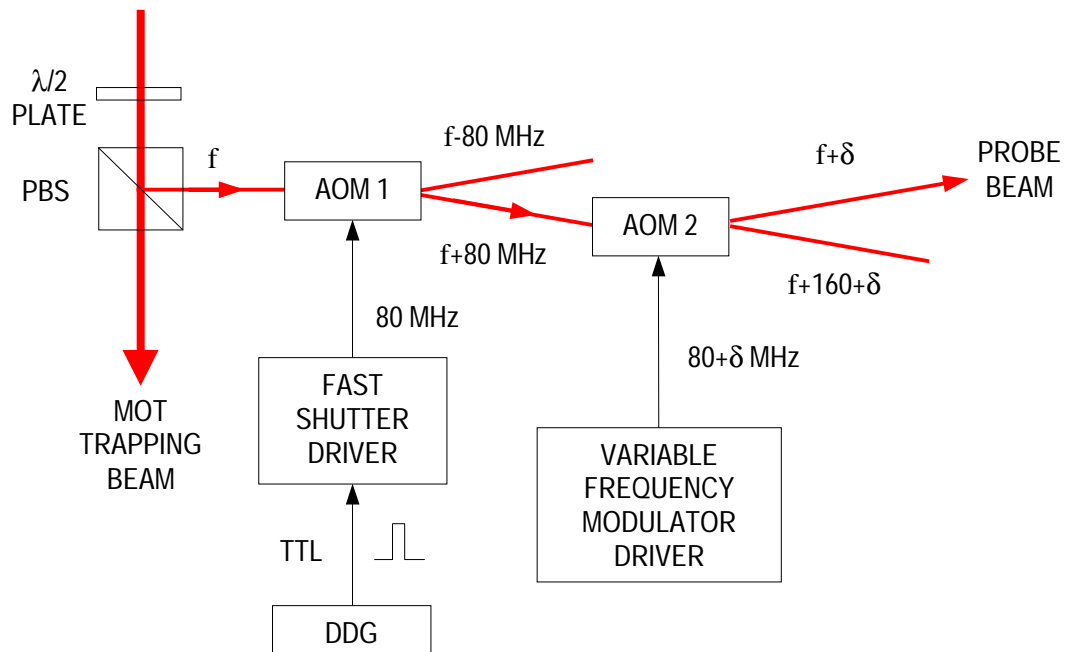


Figure 3.10 Schematic of Acousto-Optic Modulator (AOM) setup. AOM 1 serves as a fast shutter and AOM 2 serves as a variable frequency shifter. AOM 1 is activated while a high voltage (4.47 V) from a TTL pulse is applied. The frequency shift δ is typically about 10 MHz. The power of the probe beam is varied with the half wave plate.

plate and polarizing beam splitter pair. The frequency of the probe beam is then shifted to resonance by a pair of AOMs as shown in Fig. 3.10. The two AOMs (model N23080 from NEOS) used in our experiment were 80 MHz frequency modulators with two different drivers. One driver (model 222A-1 from Isomet Corporation) has a fixed frequency (80 MHz) shift and is externally triggered. The other (model D301B from Isomet Corporation) has a variable frequency shift (60-100 MHz) without external trigger. The probe beam was tuned to resonance by adjusting the frequency shift of the second AOM. The externally triggered driver served as a fast shutter since the AOMs could be opened and closed in less than a microsecond.

3.4 The vacuum chamber and pumping system

In laser cooling and trapping, it is important to have a good vacuum system. The trapping and guiding experiment was typically done between 10^{-8} - 10^{-7} Torr. The chamber consists of a stainless UHV six-way cross and tubes with an ion pump, a glass cell and a cesium (Cs) ampule connected to them (Fig. 3.11). The vacuum system has all metal seals except the valves and the glass cell. The tubes have 1.5 inch OD with $2\frac{3}{4}$ inch conflat flanges. To allow laser beams to enter, glass viewports were attached on two sides and the bottom of the six-way cross.

The right-angle valves (V_1 , V_2 in Fig. 3.11) are sealed by viton o-rings and can hold pressure below 10^{-8} Torr. The valve (V_3) separating the Cs source from the chamber is a small bellows valve with metal ball sealing. A glass tube containing pure cesium metal was used to introduce Cs vapor into the chamber. A flexible glass-metal transition

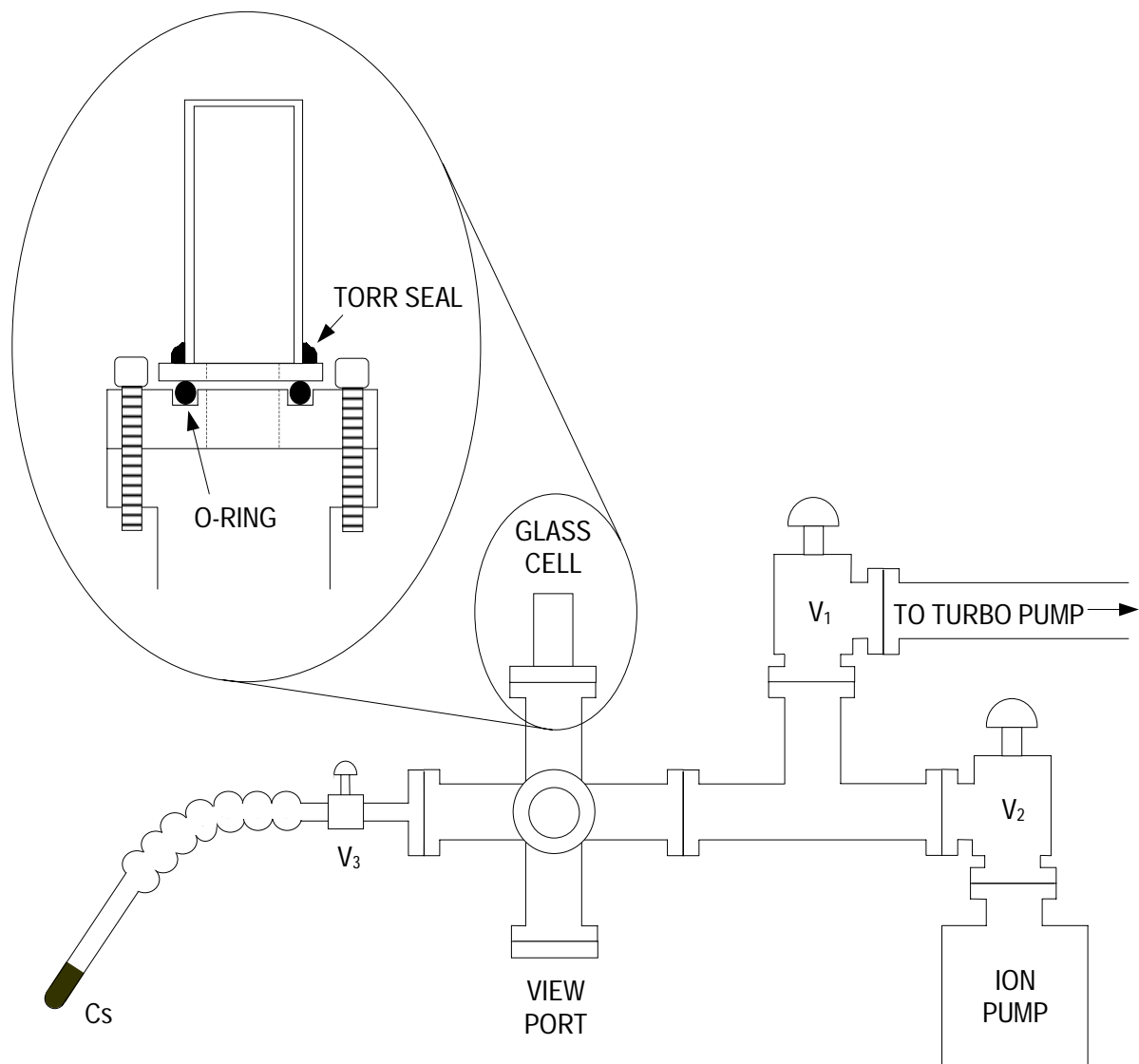


Figure 3.11 The vacuum chamber. The tubes are of stainless steel with 1.5 inch OD and $2\frac{3}{4}$ inch conflat flanges. Three o-rings were used: in V₁, V₂ and under the glass cell. After pre-pumping with the turbo pump, V₁ was closed and the turbo pump was removed. The glass tube that contained Cs was filled with argon before it was attached to the chamber. A heating tape (not shown) around the glass tube controlled the vapor pressure.

connected the glass tube to the bellows valve. The glass tube is oriented downward to prevent cesium from flowing to the valve and the chamber because it is fluid above 28 °C. The cesium container was wrapped with heating tape to evaporate the cesium metal. The vapor pressure in the chamber was controlled by changing the voltage applied on the heating tape. The glass cell (2.5 cm × 2.5 cm × 7 cm) in which the MOT is formed sits on top of the six-way cross. To reduce the distance from the cell to the center of the six-way cross, we attached the cell directly on a stainless steel flange. The first design we used was to glue the cell on a flange with low vapor pressure epoxy (Torr Seal from Varian Vacuum Product, $P < 10^{-9}$ Torr). But this never worked satisfactorily: The cell broke because of the different thermal expansion ratios of the glass and the metal when the chamber was baked. Since this problem resulted from the direct contact between two different materials, we inserted a transition between them. The glass cell was epoxied on a glass disk with a 2 cm diameter hole drilled in it. The disk then sits on an o-ring that is located in a groove machined on the flange (inset of Fig. 3.11). The cell was tightly held in position by the air pressure after the chamber was pumped down. This design worked well, and we could reach below 10^{-8} Torr successfully.

An 8 l/s ion pump (model # RVA-8-DD/0 from Duniway Stockroom Corp) was employed to maintain the vacuum in the chamber. Ion pumps are well suited to our application for they are small, quiet, require no cooling and have low ultimate pressures. Ion pumps show degradation each time they are opened to air. After several pumpdowns and/or many hours of operation (10,000 hours at $P \sim 10^{-6}$ Torr), the pumping element needs rebuilding. For an ion pump to start pumping, the chamber must be pre-pumped below 10^{-2} Torr. In our case, we used a 170 l/s turbomolecular pump to rough the

chamber down to $\sim 10^{-5}$ Torr before the ion pump was turned on. To accelerate pumping out the residual gases (mostly H_2O), the chamber and the ion pump was baked at ~ 200 °C (~ 120 °C near the o-rings) for several days. The pressure was measured by the current drawn by the ion pump. The pressure in our chamber was below 10^{-8} Torr, which is the minimum scale of our ion pump controller.

3.5 Other instruments

3.5.1 Oscilloscopes

Several oscilloscopes were used in our experiment. An analog oscilloscope (model # 466 from Tektronix) was used to display signals from the spectrum analyzer. A mainframe with two differential plugins (model # 7633 from Tektronix) allowed 4 different signals to be displayed on a screen simultaneously. It was used to monitor all three lasers at the same time. A digitizing oscilloscope (model # 5411D from Hewlett Packard) was used for digitizing various signals. The digitized signals are saved on the computer through a GPIB interface. Figures 3.5, 3.7, and 4.5 were obtained by this oscilloscope.

3.5.2 Spectrum analyzer

An optical spectrum analyzer (model # FPZ-1CU from Tec Optics) was used for two purposes. The first was to analyze the spectral profile of the diode lasers and make sure that outputs from the external cavities were single mode. The second was to determine the detuning of the guiding laser relative to the frequency of the trapping beam. This required displaying the spectra of both the trapping laser and the guiding

laser on a screen as shown in Fig. 3.5. The spacing between the two spectra was calibrated by saturated absorption spectroscopy.

CHAPTER 4

MAGNETO-OPTICAL TRAP OF CS ATOMS

AND

A PRELIMINARY GUIDING EXPERIMENT

In this chapter, the basic principles of the vapor cell magneto-optical trap (MOT) of Cs atoms, and experimental results using them will be discussed. The preliminary guiding experiment with a hollow beam will be described in the last section.

4.1 Cesium

Cesium ($^{55}\text{Cs}_{133}$) is an alkali metal that was discovered by spectroscopic analysis in 1860. Cesium melts at $T = 28.5\text{ }^\circ\text{C}$ and is one of the three elemental metals that are liquid at room temperature. Cesium has a great affinity for oxygen and burns brightly in humid air. Caution must be used not to expose Cs to water or humid air. It is safe to store cesium under argon when it is not in vacuum.

Like other alkali metals, Cs has a simple electronic configuration ($[\text{Xe}]6s^1$) and is easy to laser cool and trap. As shown in Fig. 4.1, the $6^2S_{1/2}$ ground state to $6^2P_{3/2}^o$ first excited state transition was used to trap the atoms. The trapping beam is tuned to the red (typically about two natural linewidths) of the cyclic transition $6^2S_{1/2}(F=4) \rightarrow 6^2P_{3/2}^o(F'=5)$, where F is the total atomic angular momentum (nuclear spin + total electronic angular momentum). Though the trapping beam is very close to this transition,

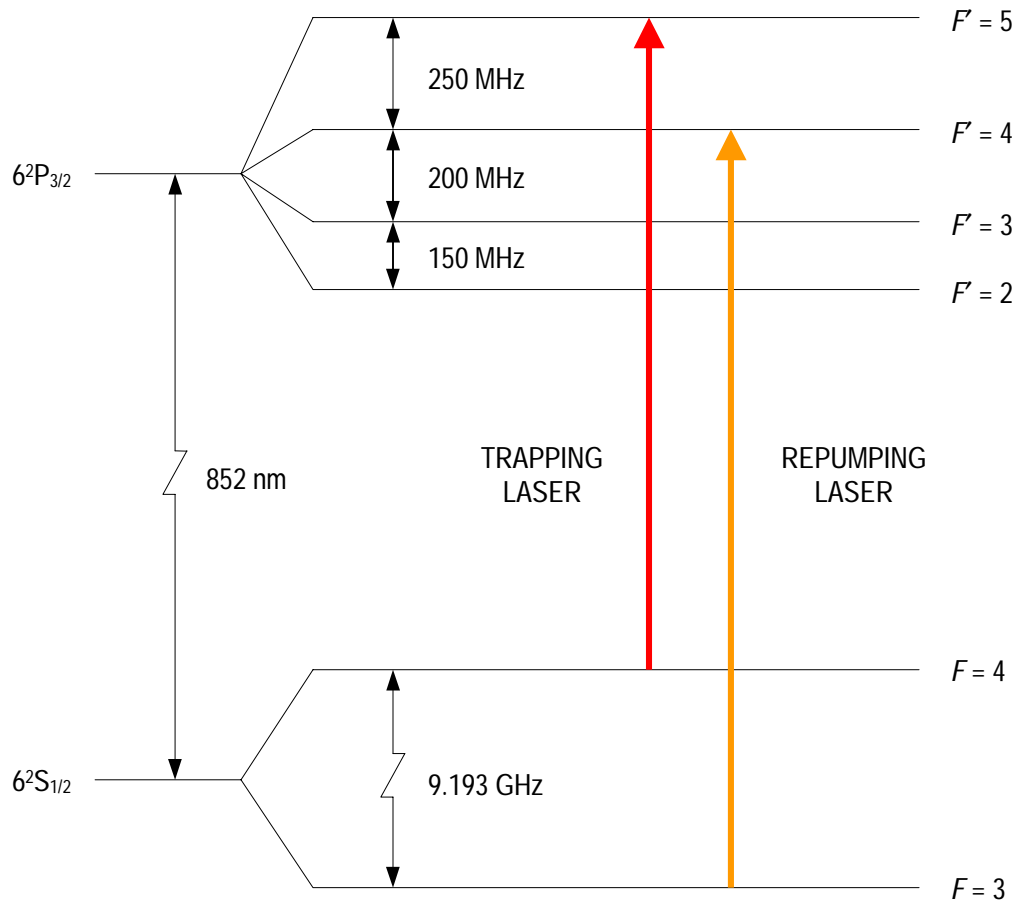


Figure 4.1 Energy level structure of Cs. The hyperfine levels are labeled by the total angular momentum F , which is the sum of the nuclear spin ($I = 7/2$) and the total electronic angular momentum ($J = 1/2, 3/2$ for S and P states respectively). The dipole selection rules allow $\Delta F = 0, \pm 1$ and $\Delta m_F = 0, \pm 1$ transitions.

there is a finite probability of inducing the $6^2S_{1/2}(F=4) \rightarrow 6^2P_{3/2}^o(F'=4)$ transition. The atoms excited to the $F'=4$ state may then decay to the $F=3$ lower hyperfine ground state and not absorb the trapping beam photons. The repumping beam tuned to $6^2S_{1/2}(F=3) \rightarrow 6^2P_{3/2}^o(F'=4)$ is used to pump the atoms optically back into the upper hyperfine state, keeping them in the cooling cycle. The first excited state $6^2P_{3/2}^o$ has a lifetime, τ , of ~ 30.5 ns [51, 52]. This gives a transition linewidth of $\Gamma = 1/(2\pi\tau) = 5$ MHz. The saturation intensity of the transition is given by $I_s = \frac{4\pi^2\hbar c\Gamma}{6\lambda^3} = 1.1$ mW/cm².

To introduce Cs vapor into the cell where the MOT is formed, the Cs reservoir is heated. Cesium has higher vapor pressure than other alkali metals as shown in Fig. 1.3. The vapor pressure of Cs is around 10^{-6} Torr at room temperature. When cesium is first evaporated into the main chamber, it takes a few days for the cesium vapor to reach the glass cell on top of the six-way cross because cesium vapor condenses readily on the stainless steel walls. After many days of operation, the walls are coated with Cs and it takes only a few hours to reach a working vapor pressure. Cesium on the walls can be removed by baking the whole chamber. An alternative for the cesium source is to use cesium getters. The getters are a cesium and chromium compound and evaporate cesium when about 5 Amp is drawn. They are safe when exposed to air and easy to use. However, we found that they are not suitable for long operation in a large volume because of the limited amount of cesium contained in them.

When the Cs reservoir is heated ($T \leq 100$ °C) for several hours, the pressure in the cell can be as high as 10^{-6} Torr, which is too high for trapping. The time for the pressure to drop to 10^{-8} Torr again depends on how much Cs is on the walls of the chamber, but

it generally takes more than twice as long as the evaporation time. It is convenient to align the MOT trapping beams to cross in the cell at high pressures where the fluorescence is clearly visible. But with the pressure too high, the MOT cannot be seen due to the fluorescence of the background atoms. In addition, fewer atoms are trapped because the laser intensity is attenuated by the background absorption. To capture as many atoms as possible, our experiment was conducted at a pressure of about 10^{-7} Torr (see Fig 4.6).

4.2 Principles of MOT

When an atom is placed in a magnetic field, the degeneracy of the hyperfine levels is removed. The separation between the energy levels is given by:

$$\Delta E = \mu_B m_F B, \quad (4.1)$$

where μ_B is the Bohr magneton (9.27×10^{-27} erg/Gauss), m_F the magnetic quantum number and B the magnetic field. If the magnetic field is inhomogeneous, ΔE will be position dependent. The transition rates to these states will also be position dependent, as will be the scattering force (Eq. 2.10) on the atoms for fixed wavelength. This position dependent force, called the Zeeman shift induced force, can be used to confine atoms in space. To formulate this confining force, we go back to the one dimensional atom whose ground and excited states are labeled as $F = 0$ and $F = 1$ respectively as shown in Fig 4.2. The magnetic gradient splits the upper magnetic quantum states into Zeeman levels. In addition, consider a pair of counter-propagating beams tuned to the red of the field-free

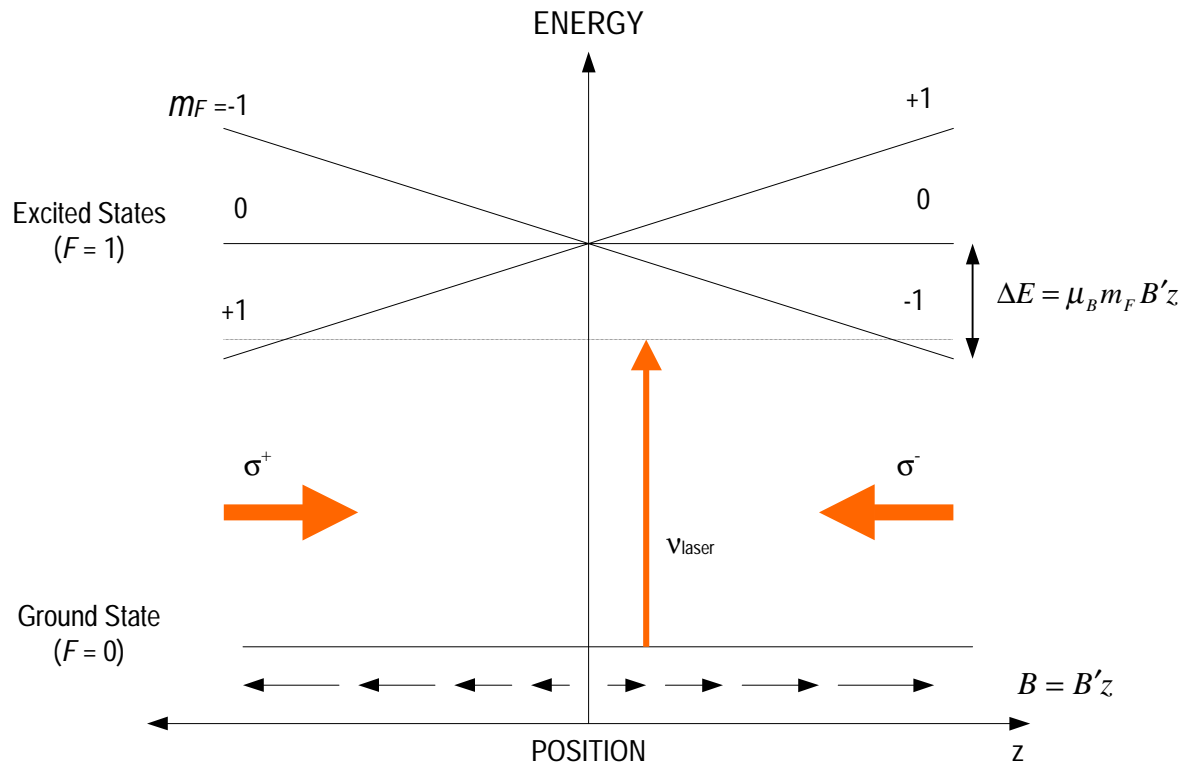


Figure 4.2 One-dimensional model of the magneto-optical trap. The magnetic field increases linearly away from the origin. On the right side the atoms absorb σ^- beam selectively and are kicked toward the origin. $B' = \partial B / \partial z$ is the magnetic gradient.

resonance with different circular helicities. Positive (negative) helicity evokes the $\Delta m_F = +1$ (-1) transitions. On the right side ($z > 0$), an atom will scatter more of the σ^- beam than σ^+ beam because transition to the $m_F = -1$ upper state is closer to resonance. Therefore, the atom will feel a restoring force toward the origin. Taking both Doppler and Zeeman shifts into account, the net force on the atom from Eq. 2.10 can be written as:

$$F_{sc} = \frac{\hbar k \pi I / I_s}{1 + I / I_s + 4 \left(\frac{\Delta - v / \lambda - \mu_B B' z / h}{\Gamma} \right)^2} - \frac{\hbar k \pi I / I_s}{1 + I / I_s + 4 \left(\frac{\Delta + v / \lambda + \mu_B B' z / h}{\Gamma} \right)^2}. \quad (4.2)$$

For an atom moving slowly near the origin, Eq 4.2 reduces to:

$$F = -\kappa z - \alpha v, \quad (4.3)$$

where the spring constant κ and damping constant α are given by:

$$\kappa = -\frac{\partial F}{\partial z} = \frac{8k|\Delta|/\Gamma(I/I_s)\mu_B B'}{\left(1 + I/I_s + 4(\Delta/\Gamma)^2\right)^2}, \quad (4.4)$$

$$\alpha = -\frac{\partial F}{\partial v} = \frac{8\hbar k^2|\Delta|/\Gamma(I/I_s)}{\left(1 + I/I_s + 4(\Delta/\Gamma)^2\right)^2}. \quad (4.5)$$

Equation 4.3 is a familiar damped harmonic oscillator and produces the magneto-optical trap (MOT). This simple one-dimensional model of a MOT is easily extended to three

dimensions. Chu and Prichard first demonstrated the MOT by capturing sodium atoms from a Zeeman slowed atomic beam in 1987 [53]. It was soon realized that slow atoms from the low energy tail of the Maxwell-Boltzman distribution can be captured by a MOT in a vapor cell. This was demonstrated by many research groups [54, 55]. We used this vapor cell MOT as the source to load our ultracold beam. Instead of using three orthogonal pairs of cooling beams and many optics, a simple way of generating a three dimensional trap with a cooling beam and an axicon mirror was also developed by Jhe *et al.* [56, 57].

4.3 Experimental arrangement

The basic arrangement for the MOT trapping beams and the repumping beam is shown in Fig. 4.3. A pair of anti-Helmholtz coils is used to generate a magnetic field that is zero near the center of the coil pair and increases away from the center. Each coil was made of 30 turns of copper wire wound around an aluminum cylinder. It has about 1.5 cm radius and a total resistance of 0.16 Ω . The coil pair is located on opposite surfaces of the glass cell. The magnetic field gradient along the symmetry axis is about 15 Gauss/cm when 1.5 Amp is applied. The six circularly polarized laser beams intersect where the magnetic field is zero. The two beams that propagate perpendicularly to the coil axis have the same polarization while the other beam that goes through the coil has different polarization. The retroreflecting beams have reversed polarization by passing quarter wave plates twice. Since we are going to make an atomic beam directed in the vertical direction with trapped atoms, four of the MOT trapping beams (beams 1, 1', 2 and 2' in Fig. 4.3) were aligned at $\pm 45^\circ$ relative to the vertical axis to make room for the

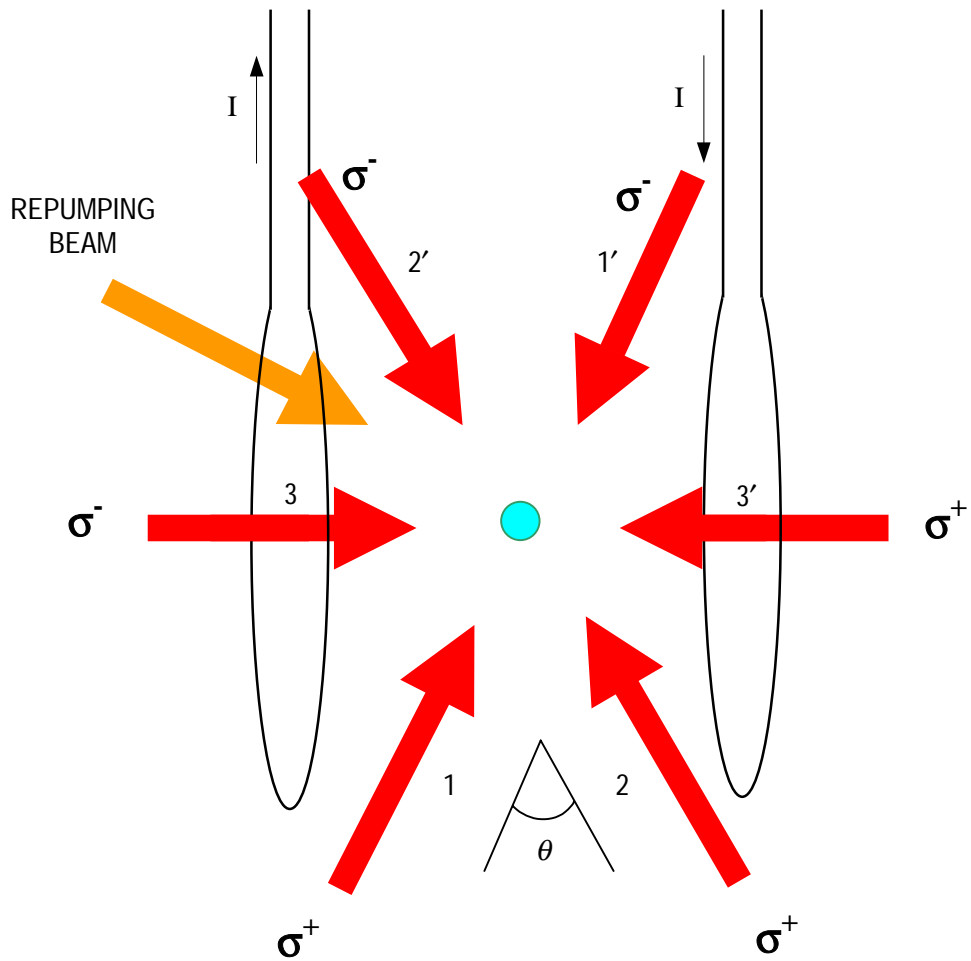


Figure 4.3 The MOT laser beam arrangement. The two anti-Helmholtz coils draw current in opposite direction to create a zero magnetic field near the center. The beams marked by 1, 1', 2 and 2' lie on a plane perpendicular to the coil axis and have $\pm 45^\circ$ with respect to the vertical axis. Beams 3 and 3' travel parallel to the coil axis. The primed beams (1', 2' and 3') are retroreflected beams.

guiding laser beam. The six trapping beams normally intersect at 90° relative to each other and have about the same power to make a spherical MOT. By changing the angle, MOTs of different shapes can be generated. In our atom-guide experiment, MOTs that had the shape of an ellipsoid with high eccentricity were especially interesting since more atoms could be trapped inside the guiding beam. A MOT a few times longer in the vertical direction than the horizontal direction was generated by increasing the angle (θ in Fig 4.3) between the beams 1 and 2. The image (b) in Fig 4.7 shows a 1 mm (horizontal) \times 3.5 mm (vertical) MOT generated with $\theta \approx 105^\circ$.

4.4 MOT loading parameters

The number of atoms loaded in a MOT can be described by a simple rate equation:

$$\frac{dN}{dt} = R - LN, \quad (4.6)$$

where R is the capture rate and L is the loss rate due to collisions with the background gases. The capture rate is the number of atoms per second that enter the trapping volume ($V = \sim 0.5 \text{ cm}^3$ for 1 cm diameter beams) with a velocity less than the capture velocity. The capture velocity is defined as the velocity at which the Doppler shift equals the detuning of the trapping laser. With a detuning of two natural linewidth ($\Delta = 2\Gamma = 10 \text{ MHz}$), the capture velocity, $v_c (= \Delta\lambda)$, is about 8.5 m/s. From the thermal distribution, the capture rate is given by:

$$R = \sqrt{8\pi} n V^{2/3} v_c^4 \left(\frac{M}{3k_B T} \right)^{3/2}, \quad (4.7)$$

where n is the number density of the background atoms. The capture rate is about a billion ($\sim 10^9$) atoms per second at $P = 10^{-7}$ Torr. The solution to the rate equation is given by:

$$N(t) = N_{ss} (1 - e^{-t/\tau}), \quad (4.8)$$

where $N_{ss} = R/L$ is the steady state number of trapped atoms and $\tau = 1/L$, the time constant of the trap.

The number of atoms trapped in the MOT can be obtained by measuring the fluorescence with a photodiode. The number of atoms is related to the photodiode signal by:

$$N = \frac{4\pi\mathcal{I}}{\eta d\Omega} \cdot \frac{\lambda}{\pi\Gamma hc} \cdot \frac{1 + I/I_s + 4(\Delta/\Gamma)^2}{I/I_s}, \quad (4.9)$$

where \mathcal{I} is the current from the photodiode, η the quantum efficiency and $d\Omega$ the solid angle subtended by the detector centered on the MOT. The quantum efficiency was 0.52 amp/watt for our diode (model # 11-01-004 from UDT Sensors, Inc.), which was determined experimentally with a beam whose power was measured by a power meter.

Figure 4.4 shows the number of atoms as a function of time while the MOT is filling. The number of atoms while the MOT fills obeys Eq. 4.8 with $\tau \approx 0.87$ sec. The time constant varies from a few hundred ms to a few seconds depending on the pressure. While the main loss in Eq. 4.6 is caused by collisions with warm background atoms, there exists another loss caused by collisions between the trapped atoms. This additional loss rate, which depends on the square of the density of the MOT, is about two orders of magnitude smaller than the main loss rate and is not considered in our experiment.

The steady state number of atoms in the MOT given by the rate equation does not depend on pressure since the trap and loss rates depend linearly on the pressure to first order. It also does not have any dependence on laser intensities and magnetic field gradient, etc. But, in actual fact, it is found that many parameters affect the number of trapped atoms. The number of atoms measured at different background pressures is shown in Fig. 4.5. The plot shows that the number is maximized at $P \sim 3 \times 10^{-7}$ Torr. One possible explanation for the decrease in the number at high pressure is that the retroreflected beams (beams 1', 2' and 3' in Fig. 4.3) are severely attenuated because of absorption by the background atoms. For example, the intensity of the retroreflected beams is reduced by 44% at $P = 1.8 \times 10^{-6}$ Torr.

4.5 Imaging schemes and the temperature measurement

The size and number distribution of a MOT can be measured by taking an image of the MOT. Two schemes of imaging are possible: fluorescence imaging and shadow imaging. The fluorescence images or shadow images of the trapped atoms were monitored with a ccd camera (model RS170 from COHU Inc.). The camera has an array

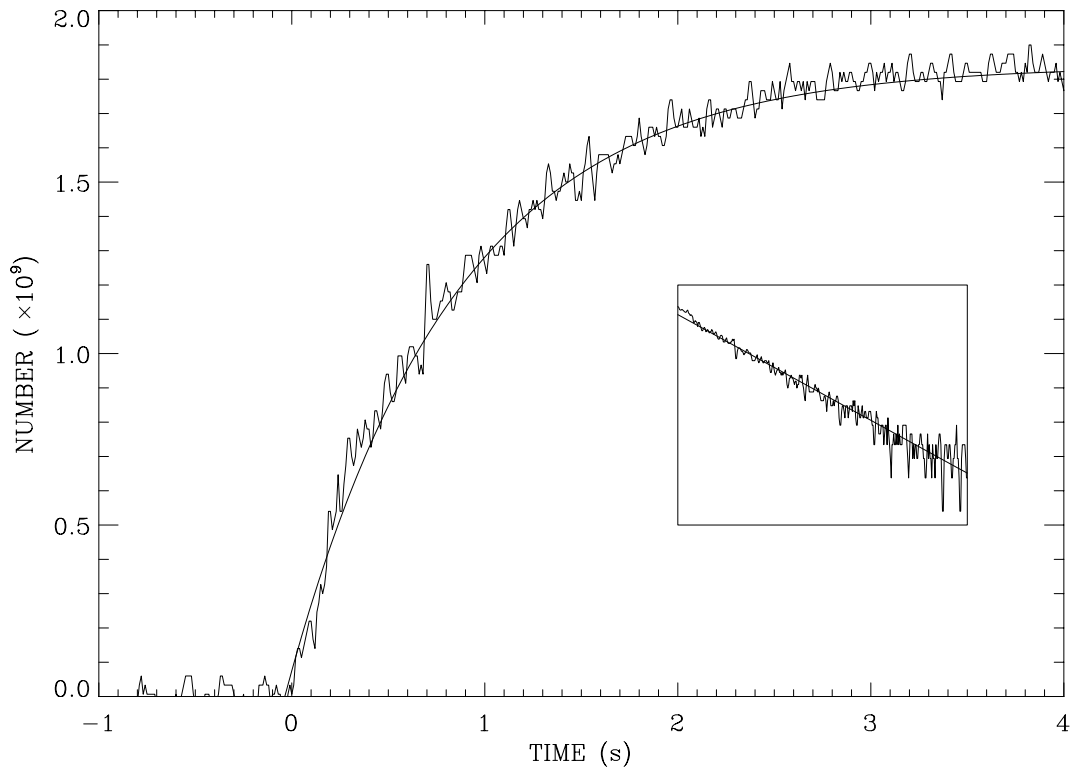


Figure 4.4 MOT buildup. The MOT starts to fill at $T = 0$ when the magnetic field is turned on. The data follow $N(t) = N_{ss}(1 - e^{-t/\tau})$ with $\tau \approx 0.87$ sec. The inset is a log plot of $N_{ss} - N(t)$, showing the exponential behavior of the number of atoms. The absolute number of atoms in the MOT was obtained from the photodiode signal using Eq. 4.9.

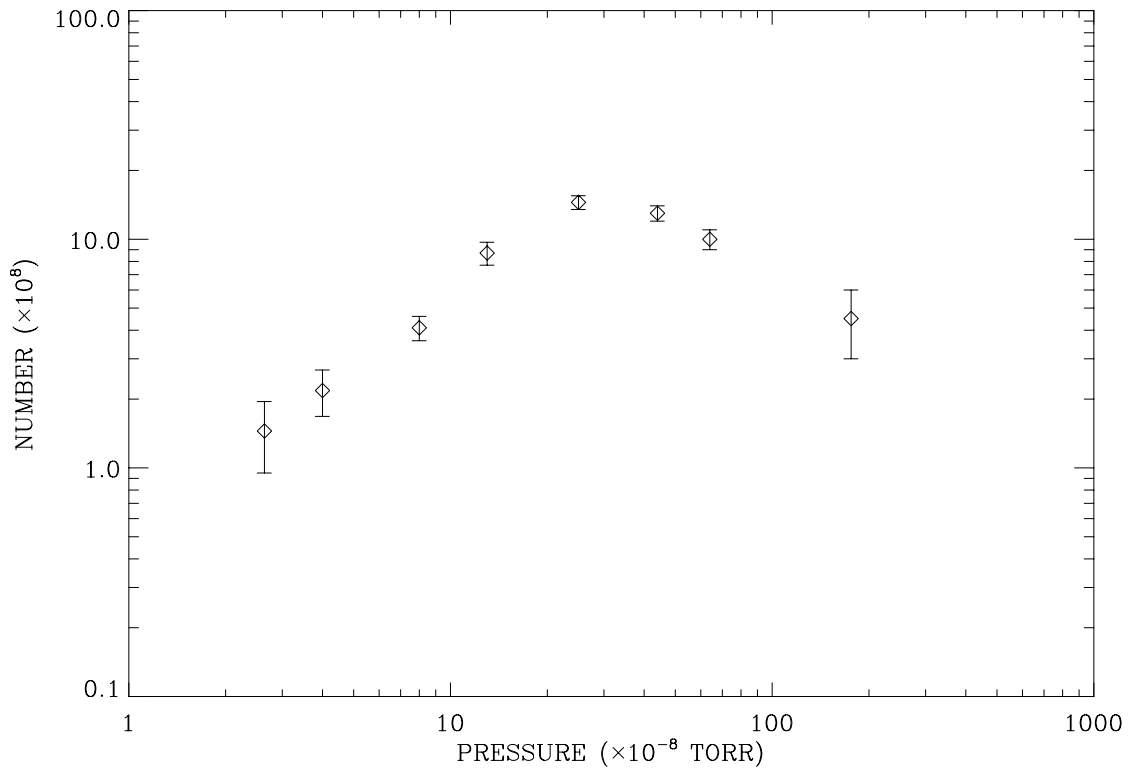


Figure 4.5 Number of atoms in the MOT as a function of the background Cs pressure. The number of trapped atoms was measured with a photodiode using Eq. 4.9. The large error bar at $P = 1.8 \times 10^{-6}$ Torr was caused by high background fluorescence. The number was maximized around 3×10^{-7} Torr. Fewer atoms were trapped at higher pressure attenuation of the retroreflected beams.

of $8.4 \mu\text{m (H)} \times 9.8 \mu\text{m (V)}$ ccd elements and captured images at 30 Hz. The images were displayed on a monochrome monitor and recorded on video tapes. A frame grabber was employed to capture and digitize the images. The digitized images were stored as tagged image file (TIF) format with 640×480 pixels by an image processing software (Matrox Magic Box from Matrox Electronic Systems, Ltd). The TIF images were then analyzed with programs written in the interface description language (IDL).

Like the number measurement, the fluorescence imaging uses the fluorescence induced by the trapping beams. Figure 4.6 shows a typical MOT fluorescence image and the density distribution. The profile of the atomic distribution fits a Gaussian function well. In general, scanning across anywhere of a MOT in the same direction gives about the same sigma of Gaussian fitting.

Shadow imaging requires a weak probe beam that passes through the cell. The absorption shadow that the atoms cast is captured by a ccd camera. The probe beam used to form the shadow was split from the MOT beam. Its frequency was shifted to resonance with two AOMs for the best image contrast. The probe beam had about 1 cm diameter and the power of about 0.1 mW. So the intensity of the probe beam was below the saturation intensity ($I_s = 1.1 \text{ mW/cm}^2$ for Cs). The camera lens was replaced by a simple lens ($f = 30 \text{ cm}$) located about 60 cm away from the MOT and the camera for one-to-one imaging and to reduce the MOT fluorescence from contaminating the shadow image. Normally a MOT is optically thick³ to a weak probe beam on resonance, which means that all the light that enters the MOT is absorbed. The shadow can therefore be

³ Definition of the optical depth and quantitative measurement for number of atoms using it will be discussed in section 6.3.

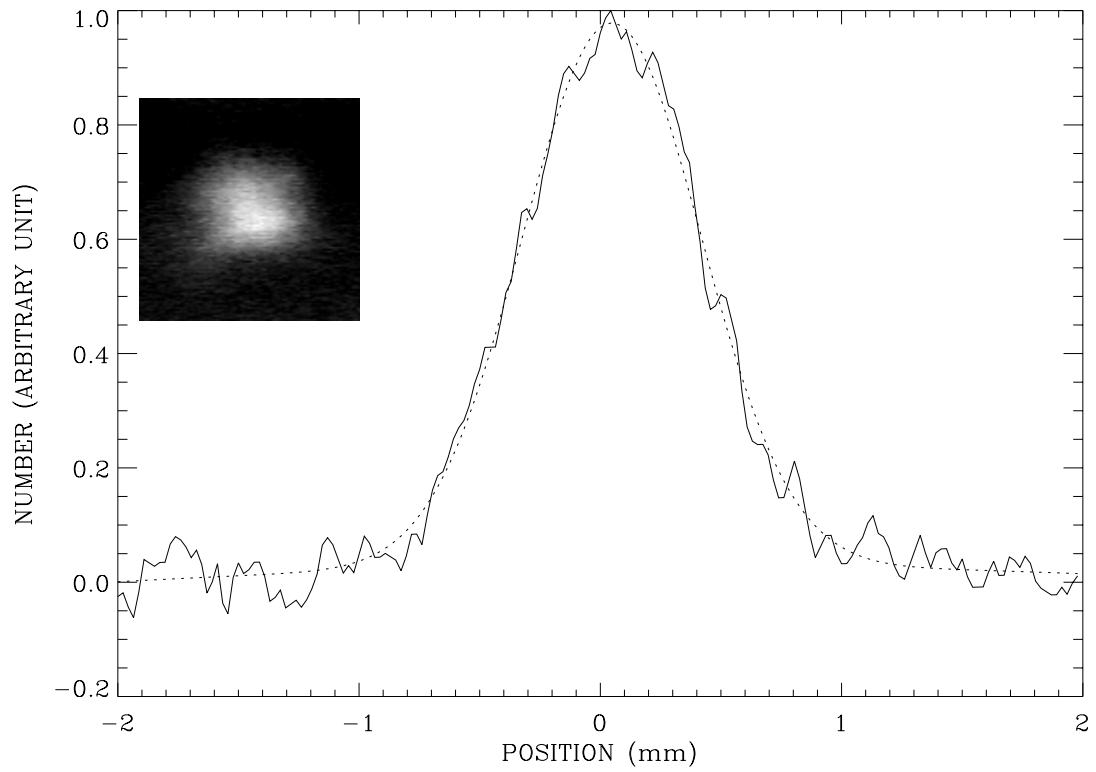


Figure 4.6 The fluorescence image and density profile of a MOT. The solid curve is the line profile across the image horizontally near the center. The dotted curve is a Gaussian fit. The sigma (σ) of the Gaussian function is 0.43 mm, which gives FWHM \approx 1 mm.

seen easily, even with an IR detection card or IR viewer. A typical shadow image and the line profile across the image are shown in Fig. 4.7. The two images in (a) are shadow images of a round MOT before and after background subtraction. The probe beam has a structure caused by the coherence of the probe beam. The probe beam develops interference patterns as it passes optical elements such as beam splitters, AOMs, lenses, and windows. Imperfection in the optical elements also affects the probe beam. To remove these artifacts, therefore, it is mandatory to subtract the background image (an image without MOT) from the MOT images. The main plot in Fig. 4.7 shows a line profile scanned across the lower image in (a). The line profile looks like a square distribution because the shadow image is completely black near the center of the MOT. Image (b) is the shadow image of a MOT in cigar shape generated by trapping beams intersecting at 105° .

In addition to stationary measurement with the images, making a movie of the cloud evolution is also possible by taking a series of images as a function of time after the MOT trapping beams are turned off. Shadow imaging was used for this purpose for several reasons. First, shadow imaging does not require an additional shutter on the camera. In fluorescence imaging, the fluorescence from the MOT must be blocked until the trapping beams are turned off. Second, the AOM can be triggered in less than a microsecond to allow precise timing. Using AOMs as shutters for trapping beam would reduce the power of the trapping beam by more than 50%. The mechanical shutter has a minimum dwell time of 1 ms and therefore cannot resolve 1 ms. Third, the weak probe beam allows imaging without disturbing the MOT while the images are taken.

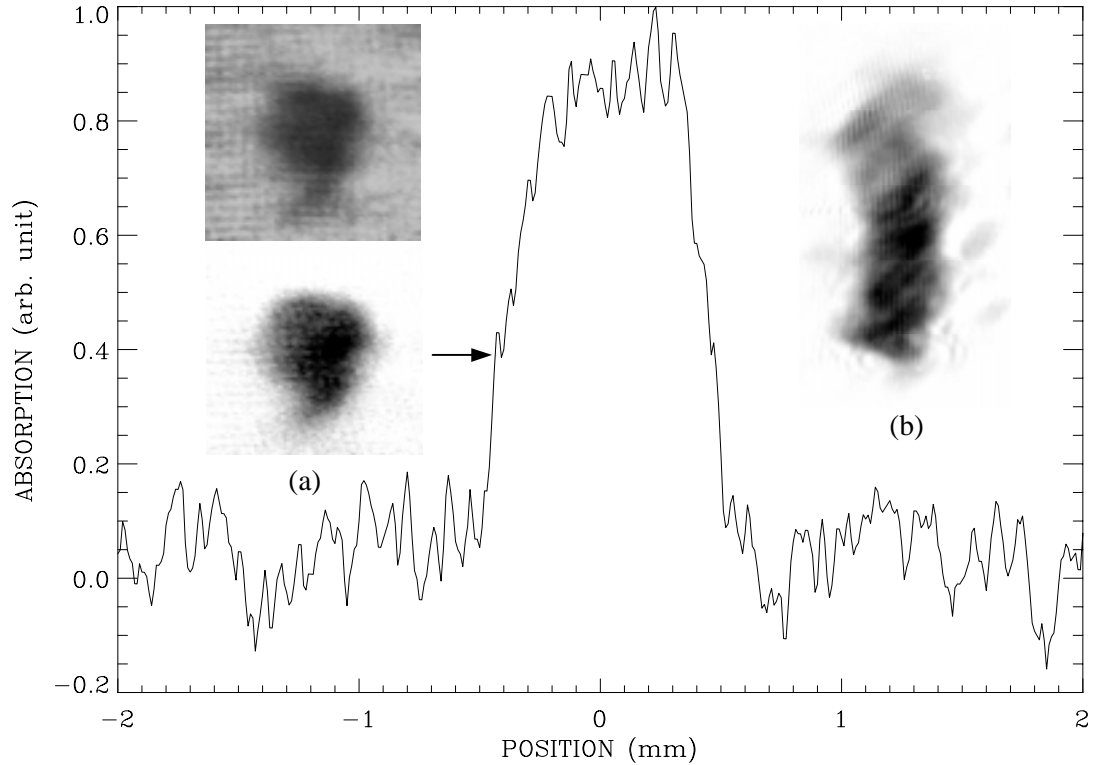


Figure 4.7 Shadow images and the density profile. (a) Shadow images of a round MOT. The top image is a raw image before the background image is subtracted. The bottom image is made after the background image is subtracted. The main plot is the profile of a line scanned across the bottom image. The top of the profile is flat because the MOT is optically thick. (b) Shadow image (after background subtraction) of a 1mm (horizontal) \times 3.5mm MOT. This was generated by trapping beams crossing at 105° as explained in section 4.3.

The timing scheme for shadow imaging is shown in Fig. 4.8. Two digital delay pulse generators (DDG, model # DG535 from Stanford Research, Inc.) were used to control the mechanical shutter and the AOM. Each DDG has 4 channels: Channels A and C are rising edges; B and D are falling edges. Channels B and D of the first DDG were used to trigger the mechanical shutter driver. The trapping beams were turned on by channel B and turned off by channel D with a 2 ms delay. Channels A and B of the second DDG was used to turn on and off one of the AOM drivers as shown in Fig. 3.10. The second DDG was triggered by the first DDG with a time delay, ΔT , and used to turn the probe beam at 0 ms, 1 ms, 2 ms, ... after the MOT trapping beams were turned off. The probe beam remained on for 50 μ s. The expansion of the atom cloud during 50 μ s was negligible (less than 10 μ m). Imaging was performed at 0.5 Hz to allow the MOT to refill so that the imaging was run with a nearly constant steady-state number of atoms. Since our camera captured images at 30 Hz, every 60 frames in the video tape had a shadow image. The shadow images were found and digitized with a frame grabber. A series of images of freely expanding atoms is shown in Fig. 4.12a.

The kinetic energy distribution can be determined by measuring the expansion ratio of the atom cloud using the shadow images. The temperature of a MOT is defined by the kinetic energy distribution of the atoms: $\frac{3}{2}k_B T = \frac{1}{2}m \langle v^2 \rangle$, or $\frac{1}{2}k_B T_i = \frac{1}{2}m \langle v_i^2 \rangle$ where $i = x, y, z$. The atoms generally have a different temperature in each direction since the confining potential is not isotropic. If we define the size of the atom cloud as the standard deviation (σ) of the Gaussian distribution, the evolution of the size is given by:

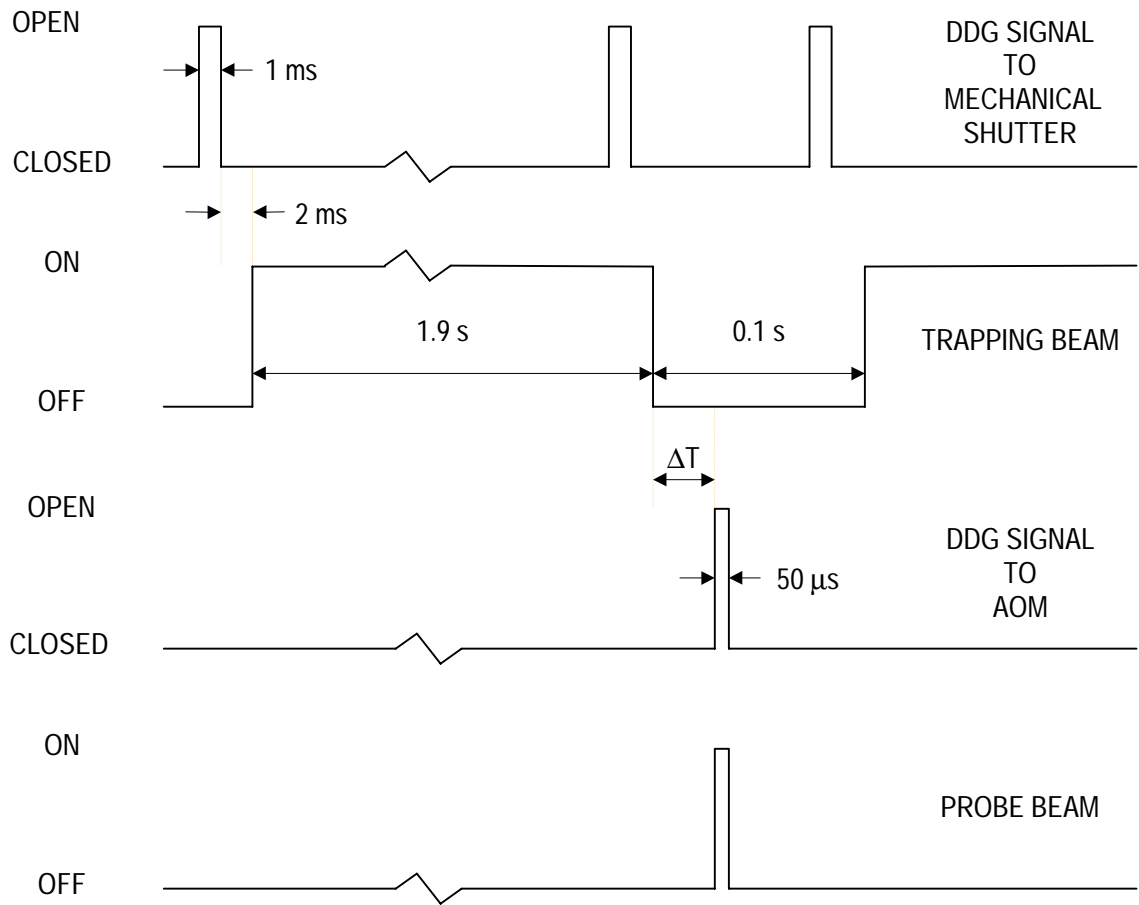


Figure 4.8 Timing scheme for shadow imaging. The MOT fills while the trapping beams are on for 1.9 s. The shadow images are taken at ΔT (in steps of 1 ms) after the trapping beams are turned off. The trapping beams are turned on and off at the falling edge of the trigger signal from the DDG with a 2 ms delay. The probe beam follows the DDG signal to the AOM with a delay of less than 1 μ s.

$$\sigma_i(t) = \sqrt{\sigma_i(0)^2 + \langle v_i \rangle^2 t^2}. \quad (4.10)$$

From the plots in Fig. 4.9, the horizontal temperature for the MOT shown in Fig. 4.12a is determined to be about 144 μK . The vertical temperature is determined to be 57 μK in the same way.

4.6 Crude atom tunnel

Starting from the MOT, one can create an ultracold atomic beam. An ultracold atomic beam has small energy dispersion and large flux compared with oven generated hot beams as discussed in Ch.1. However, the non-zero transverse temperature causes the ultracold beam to diverge. To prevent the divergence, we loaded the ultracold atoms into a hollow core laser beam where the atoms can be guided by the dipole force as explained in Ch. 2.

Before we prepared a diffractionless hollow beam, we did a preliminary experiment with a ‘quasi’ hollow beam generated by blocking the center of a Gaussian mode beam. The experimental setup to generate the hollow beam is shown in Fig. 4.10. The center of a 70 mW, 10 mm diameter ($2w$) Gaussian beam was blocked with a 5 mm disc placed immediately before a thin 200 mm converging lens. The apertured beam was directed through a thick 38 mm converging lens, approximately 255 mm away from the first lens, to form a nearly collimated tunnel (hollow) beam with a 1 mm hole. The hollow beam was aligned slightly off the vertical direction to keep the reflection on the bottom window of the six-way cross from overlapping the incident beam. Profiles of the

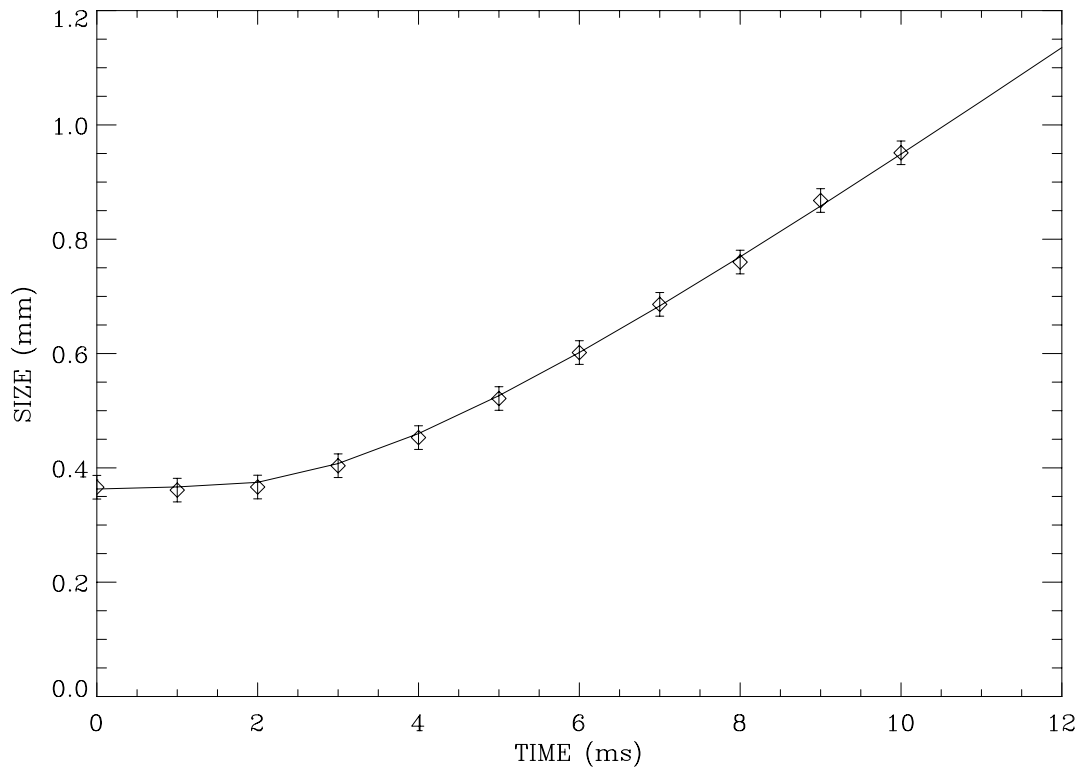


Figure 4.9 The horizontal size of a MOT measured at consecutive times. The shadow images used for this data are shown in Fig 4.12a. The horizontal size is defined as the sigma of the Gaussian fit to the profile integrated over the vertical direction. Each point in the plot is the average size of 10 images. The solid curve is the theoretical values for free expansion at $T \approx 144 \mu\text{K}$ ($v_{rms} \approx 9.5 \text{ cm/s}$). The vertical temperature for this MOT is found to be $57 \mu\text{K}$ ($v_{rms} \approx 6 \text{ cm/s}$).

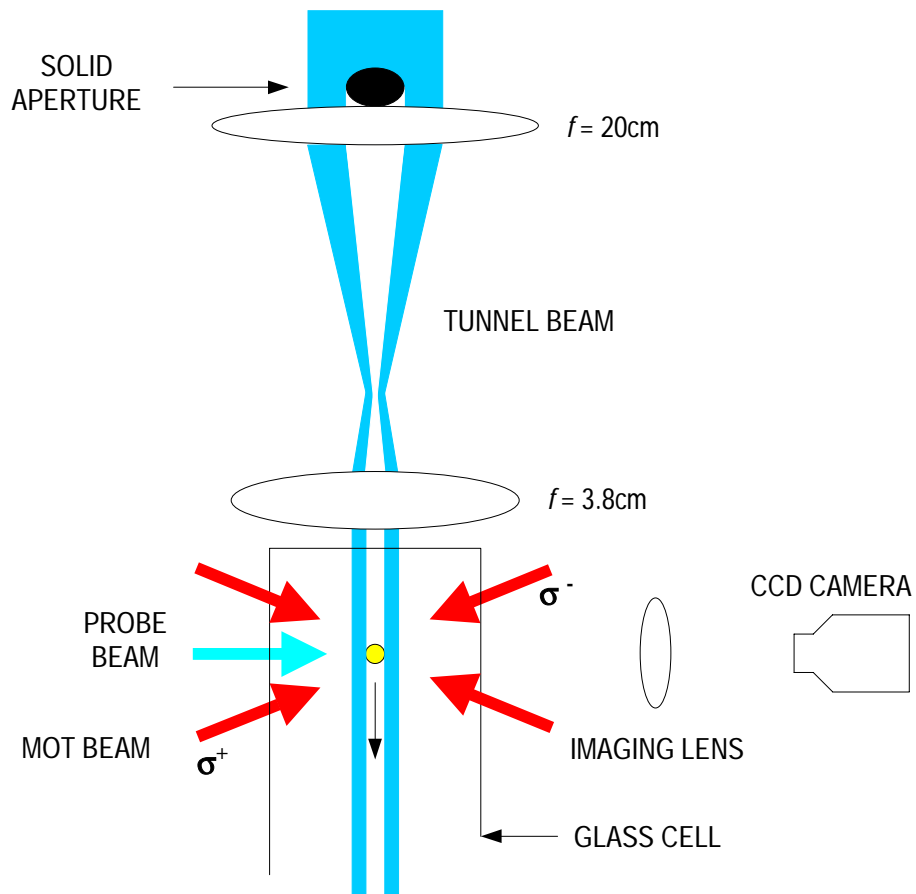


Figure 4.10 Setup for the crude atom tunnel. A hollow beam was generated by blocking the center of a 70 mW TEM_{00} mode diode laser beam. The MOT was formed inside the tunnel. The evolution of the atom cloud was monitored by shadow images with a ccd camera. The hollow beam was aligned slightly off the vertical.

hollow tunnel beam 30 and 80 mm beyond the second lens are shown in Fig. 4.11. Since the hollow beam has uncorrected phase fronts, its hole is maintained only for a short range. A bright dot (Poisson's spot) at the center of the image and airy rings can be seen in the lower images of Fig. 4.11. Consequently this demonstration was limited to a few centimeters.

The first step in creating the beam was putting the atoms into the tunnel. To facilitate loading the tunnel, the MOT was formed inside the tunnel. In order for the MOT and tunnel to coexist, the tunnel had to be detuned at least 100 MHz from resonance; otherwise, the MOT loading was inefficient. The experiments were done at detunings between 0.25 and 1.0 GHz. Whereas it was necessary to employ saturated absorption spectroscopy to lock the MOT beams to their proper frequencies, the tunnel beam need only be stationary to within tens of megahertz, rendering locking unnecessary.

Several different combinations of MOT and tunnel diameters were tried. Essentially all atoms trapped in the MOT were confined in the tunnel when the MOT diameter was smaller than the tunnel diameter. As would be expected, when the MOT diameter exceeded the tunnel diameter, those atoms residing outside the tunnel were expelled when the tunnel beams were extinguished while those inside were confined. Once the MOT was formed in the tunnel, all the MOT trapping beams were extinguished with a mechanical shutter. The ultracold atom cloud then fell under gravity and expanded. The evolution of the atom cloud was monitored by its shadow with a ccd camera as explained in the previous section.

Shadow images demonstrating confinement of the cold atoms are shown in Fig. 4.12. Without the tunnel the atom cloud expands symmetrically (Fig. 4.12a) whereas in

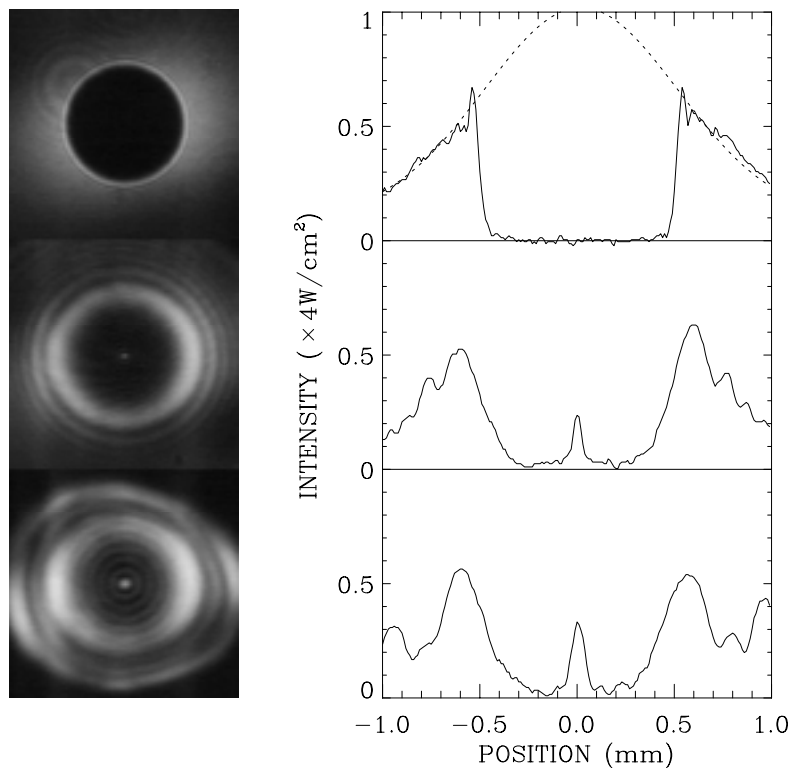


Figure 4.11 Spatial images (left) and radial intensity profiles (right) of the hollow beam 3 cm, 8 cm and 13 from the second lens in Fig. 4.11. The dotted curve is the laser beam profile without the solid aperture. About 63% of the incident power was blocked by the solid aperture. The anisotropic power distribution in the images was caused by the elliptical shape of the incident beam. The experiment was performed at the position of the top image.

the tunnel it expands asymmetrically (Fig.4.12b). In this case, the full width of the near Gaussian distribution of atoms is about 0.7 mm while the tunnel diameter was about 1 mm. The asymmetric shape in the tunnel indicates transverse confinement of the atoms by the tunnel walls as the cloud moves longitudinally (downward in this case). Three characteristics of the channeled cold atoms were analyzed from these images: (1) the transverse (horizontal) cloud size, (2) the longitudinal (vertical) cloud size, and (3) the longitudinal position of the center of mass of the cloud. A quantitative measurement of the number of atoms in the MOT and in the tunnel was made possible by digitizing the ccd images. To determine the size of the cloud it was necessary to define the volume

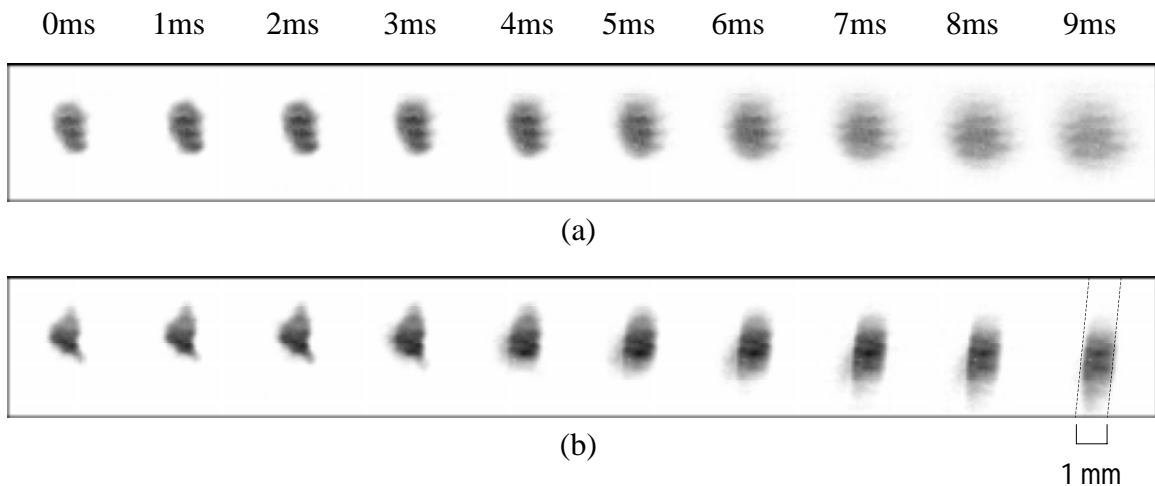


Figure 4.12 Shadow images showing 9 ms of evolution of the atom cloud (a) without and (b) with the tunnel beam. The tunnel laser was detuned by 750 MHz to the blue of resonance. Its hole diameter was ~ 1 mm. The horizontal lines in the images are caused by interference and are artifacts caused by the coherence in the probe beam as explained in section 4.5. The dashed lines indicate the tunnel beam.

occupied by the atoms while in the tunnel. An exact determination is nontrivial because the spatial distribution of the cloud changes as the atoms evolve from being trapped in the MOT to being confined by the tunnel. The atomic distribution within the cloud is approximately Gaussian in the longitudinal direction in both the MOT and the tunnel but changes from Gaussian to near square in the transverse direction once restricted by the tunnel. As a consistent metric for monitoring the evolution, we fit the distribution in both directions to Gaussian and defined the size of the cloud as the standard deviation. Even though this method does not give the true transverse size, it did allow us to track changes in the transverse size with time. The actual transverse size of the cloud in the tunnel could be extracted directly from the images, since the atoms expand and fill the full hole diameter of the tunnel, as is clearly shown in Fig. 4.12b.

Figure 4.12 offers clear evidence of confinement in the transverse direction as the atoms move downward. The transverse sizes as a function of time with and without the tunnel are shown in Fig 4.13. Without the tunnel, the atom cloud expands according to Eq. 4.10 with $v_{rms} \approx 9.5$ cm/s. The temperature in the transverse direction is $T \approx 144$ μ K. The expansion in the tunnel deviates from this once a significant number of the atoms in the cloud hit the light wall, about 4 to 5 ms after the MOT beams are turned off. The atoms are colder ($T \approx 57$ μ K) in the longitudinal direction. In Fig. 4.14, we see that the cloud expands at a slightly higher rate with the tunnel in the longitudinal direction. The reason for this high expansion rate is that the scattering acceleration depends on the transverse velocity. Atoms with large transverse velocity collide more often with the potential wall as well as they penetrate deeper. Therefore, they scatter more photons and

are subject to larger scattering acceleration than the atoms that move slowly in the transverse direction.

Figures 4.12 and 4.15 show that when the atoms interact with the wall the cloud is accelerated faster than without the tunnel. Without the tunnel, the cloud accelerates at g (9.8 m/s^2) whereas 4 ms into its evolution in the tunnel, it accelerates at a higher rate, about 23 m/s^2 . This additional acceleration is caused by recoil during photon absorption. Though the atoms spend most of their time in the dark, they absorb photons when they move into and out of the light walls. The acceleration is proportional to the average scattering rate and the recoil velocity. Analytic evaluation of the scattering acceleration will be shown in Ch. 5.

In this experiment, we demonstrated the first hollow beam atom tunnel. We generated a non-diverging ultracold atomic beam by loading the MOT atoms into the tunnel. However, the diffraction of the apertured beam limits the tunnel operation to a few centimeters. For long distance transport, we need a hollow beam that preserves the core. In Ch. 5, a simple method for generating non-diffracting hollow beams will be discussed.

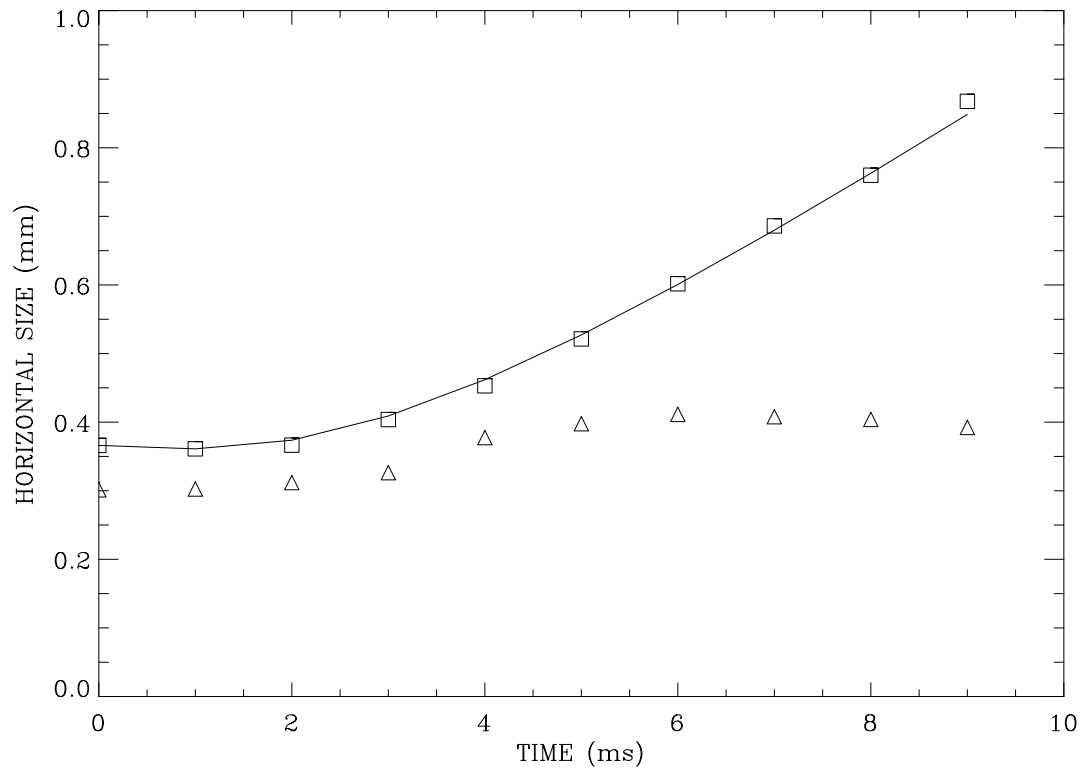


Figure 4.13 Horizontal (transverse) size of the atom cloud with (\triangle) and without (\square) the tunnel beam. The solid curve is the theoretical free expansion corresponding to $T \approx 144 \mu\text{K}$ ($v_{rms} \approx 9.5 \text{ cm/s}$). The atoms in the tunnel beam start to deviate from free expansion around 4 ms.

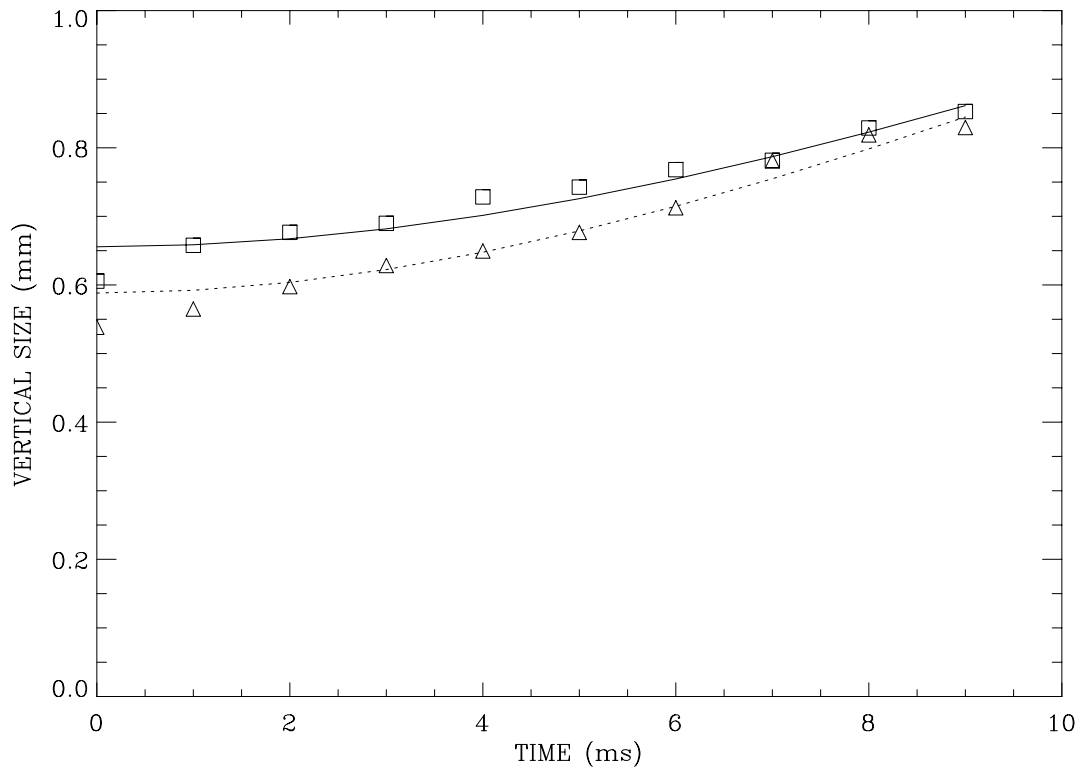


Figure 4.14 Vertical (longitudinal) size of the atom cloud with (\triangle) and without (\square) the tunnel. The solid curve is the theoretical free expansion corresponding to $T \approx 57 \mu\text{K}$ ($v_{rms} \approx 6 \text{ cm/s}$). The dashed curve is the tunnel expansion corresponding to $T \approx 57 \mu\text{K}$ ($v_{rms} \approx 6 \text{ cm/s}$) and $a_{sc} = 13.2 \text{ m/s}^2$ (see Eq. 6.3). The cloud expands faster with the tunnel than it does without the tunnel because the atoms in the tunnel are subject to different optical acceleration depending on their transverse velocities.

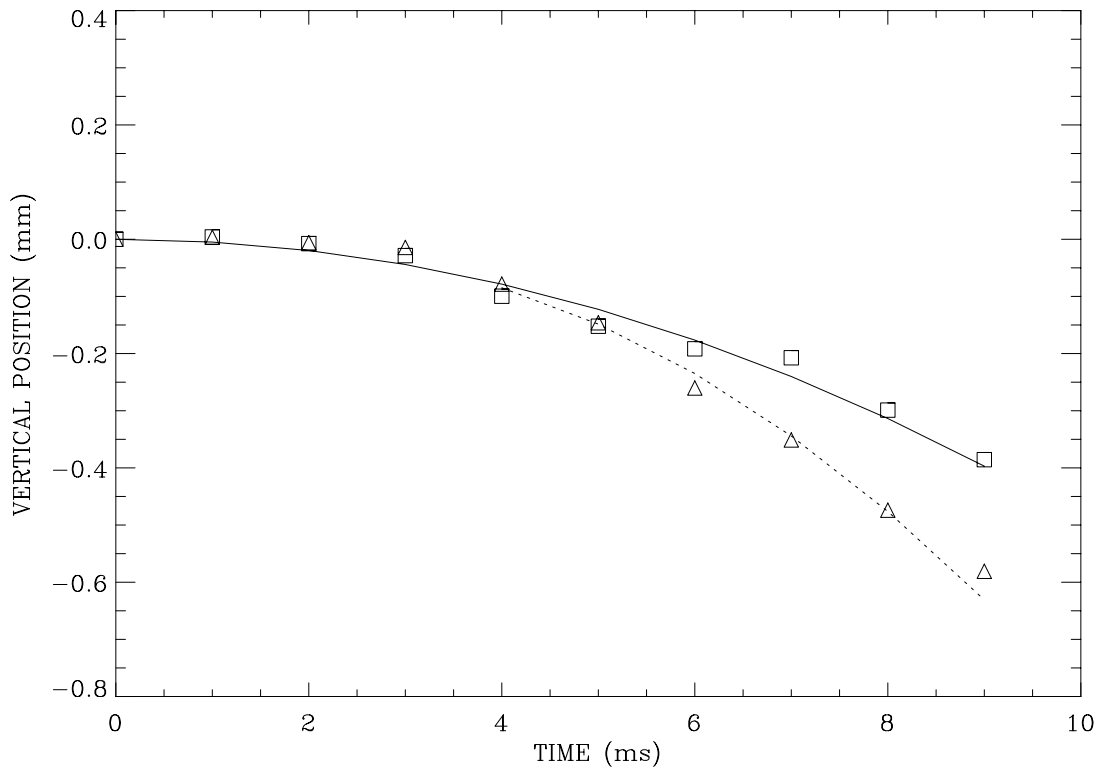


Figure 4.15 Vertical position of the atom cloud with (Δ) and without (\square) the tunnel. The solid curve represents the positions the center-of-mass expected for a cloud accelerating under gravity. The dashed curve is the expected position of the cloud for an acceleration given by $g+a_{sc} \approx 23 \text{ m/s}^2$, after the atoms begin to interact with the wall.

CHAPTER 5

EVOLUTION OF COLD ATOMS

IN THE AXICON GENERATED HOLLOW BEAM

A simple method of generating a hollow beam using axicons and spherical lenses is discussed in this chapter. The axicon generated hollow beam has an extended dark core and steep walls that are suitable for guiding ultracold atoms over long distance. Our model for the evolution of atoms in the tunnel is also discussed.

5.1 Generating hollow core beams

In the last chapter we generated a non-diverging ultracold atomic beam from magnet-optically trapped atoms. Long distance transport, however, requires a diffractionless hollow beam. Optical beams with hollow core have been of special interest in optics and atomic physics. Beams such as a TEM_{01}^* donut mode beam, higher order LG_{0m} modes, higher order Bessel beams and vortex solitons belong to this family of hollow-core optical beams. These beams differ from the hollow beam generated simply by blocking a Gaussian mode beam with a solid aperture in that they are non-diffracting. The usefulness of these hollow beams lies in the preservation of the hollow core during propagation. Several techniques for generating hollow beams from a TEM_{00} (or LG_{00}) mode have been developed. Some recent techniques involve vortex gratings [58, 59], computer generated holograms [60, 61], hollow core optical fibers [62] and axicons [63]. Of these, we selected the axicon method because of its simplicity, high efficiency and ready availability.

The axicon, an optical element with a conical surface, was first introduced in the 1950s [64]. Its non-spherical property has led to a variety of applications, including laser machining [65] and line focusing of intense laser beams for plasma generation [66]. Another useful application of the axicon is to turn a Gaussian mode beam into a hollow core beam. Grimm *et al.* used an axicon and a simple spherical lens to generate a rapidly diverging hollow beam to trap cold atoms in a conical atom trap [67], which motivated us to use axicons for generating our hollow atom guide. The ring diameter increased with a 50 mrad divergence angle. The width of the ring also increased by a factor of two over a length of 3.5 mm. Though the rapid divergence of the hollow core diameter is necessary for the conical atom trap, it is not desirable for an atom guide. It is possible, however, to control the divergence as is discussed below.

To generate and manipulate hollow beams with axicons, one first needs to understand the properties of axicons, especially in comparison with spherical lenses. The fundamental difference between an axicon and a lens is that the angle of refraction in an axicon is not position-dependent, whereas the angle in a lens depends on the position of the rays. The action of a thin lens with a focal length f on a ray can be expressed using ray matrix technique as:

$$\begin{pmatrix} r_2 \\ r_2' \end{pmatrix} = \begin{pmatrix} 1 & 0 \\ -1/f & 1 \end{pmatrix} \begin{pmatrix} r_1 \\ r_1' \end{pmatrix}, \quad (5.1)$$

where r_1, r_2 are the transverse displacements from the propagation axis, and r_1', r_2' are the slopes of the ray, before and after the lens respectively, as shown in Fig 5.1. The change

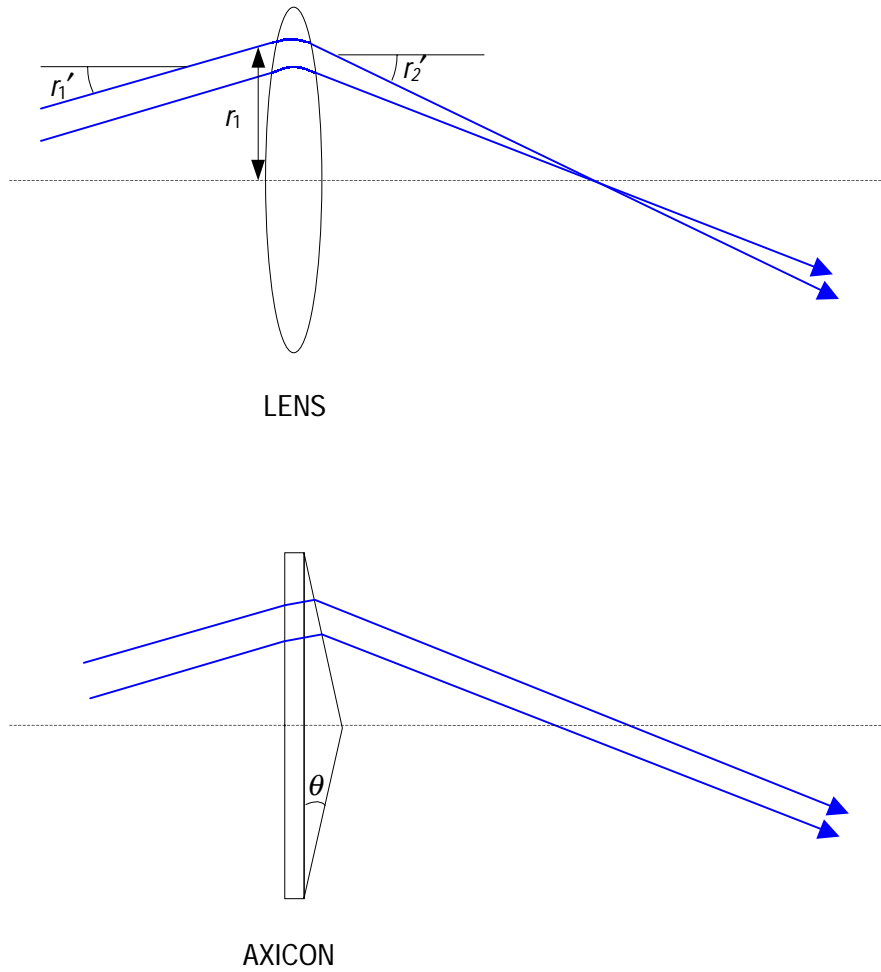


Figure 5.1 Spherical lens vs. axicon. Axicon has a conical surface on one side. The axicon refracts the rays by a constant amount whereas the lens refracts them in harmonic fashion. The shape of the ray focused by an axicon is inverted. A ring shaped profile can be generated from a Gaussian mode beam with the axicon.

in the slope is proportional to the position of the ray. The action of an axicon on the angle of a ray, however, is independent of the position of the ray. For an axicon with small base angle θ ($= 3^\circ$ for our axicons), the action can be written as:

$$\begin{pmatrix} r_2 \\ r_2' \end{pmatrix} = \begin{pmatrix} 1 & 0 \\ 0 & 1 \end{pmatrix} \begin{pmatrix} r_1 \\ r_1' \end{pmatrix} + \begin{pmatrix} 0 \\ (1-n)\theta \end{pmatrix}, \quad (5.2)$$

where n is the index of refraction of the axicon ($n = 1.5$ for axicons made of optical glass). The slope r' was assumed to be small, and small changes (< 0.1 mm) in r were ignored. The divergence of the ring generated by an axicon is half the base angle of the axicon. Though two variables r and r' are enough to describe a Gaussian beam, hollow beams need four variables: the radii and divergences of inner and outer walls (r_i, r_i', r_o, r_o'), or equivalently the central radius of the wall (r_i), its width ($w = r_o - r_i$) and the divergences of the wall and ring (r_i', w'). The ray matrix of a lens for w and w' is exactly the same as the one in Eq. 5.1. This means that a spherical lens acts on both the core and the wall in the same manner. One cannot control the four variables independently by using only spherical lenses. On the other hand, since an axicon acts only on the core diameter without affecting the wall thickness, a combination of lenses and axicons, in the proper order, allows manipulation of all four variables of the hollow beam to be made independently. In general, at least four optical components are needed to produce a specific hollow beam, just as two spherical lenses are needed for Gaussian beam manipulation.

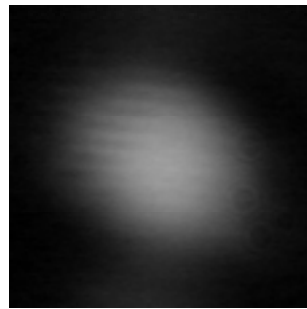
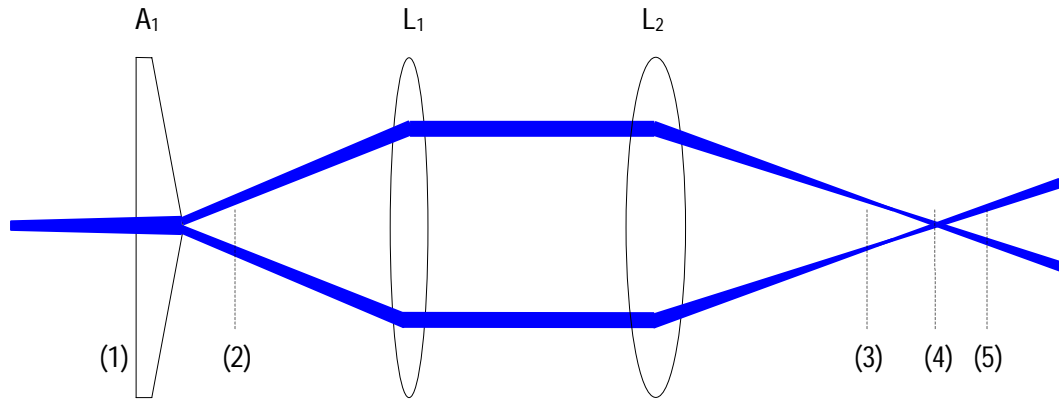
One bad aspect of the axicon is the singularity at the center. The tip is an obstacle in the beam that causes diffraction. The diffraction pattern consists of a series of rings plus a bright spot on the axis as shown in image (2) of Fig. 5.2. The main power goes into the 0th order ring (the outermost ring). From Eq. 5.2, the diameter of the outermost ring is given by:

$$d = 2\theta(n-1)D, \quad (5.3)$$

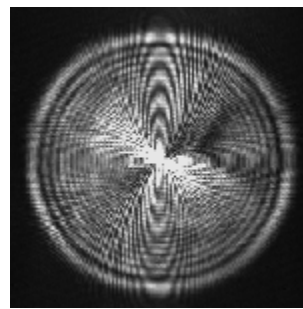
where D is the distance from the axicon. The measured value of the diameter at $z = 7$ cm is ~ 3.7 mm and agrees with Eq. 5.3. When a hollow beam is focused with a lens, generally the ring and hollow core are focused at different positions.⁴ In the specific case of Fig. 5.2a, the 0th order ring has the minimum width, 4 cm before the beam intersection (image (3)). The diameter of the beam at the focal point of the ring can be varied by changing the divergence of the incident beam. The hole disappears completely at the beam intersection (i.e., 2 mm after position 4). The rings all overlap and cannot be resolved near the beam intersection as shown in image (4). Image (5) shows that the higher order diffraction rings still remain inside the 0th order after the rings cross.

The hollow beam propagates differently if the focusing lens (L_2) is replaced by an axicon (A_2). First, the rings remain collimated (i.e., the thickness does not change) after the beam traverses the second axicon. Second, the higher order rings are found outside

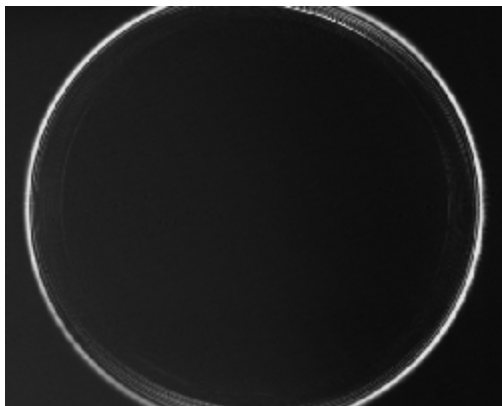
⁴ Focusing the ring means to minimize the ring thickness, and focusing the core means to reduce the rings to a point.



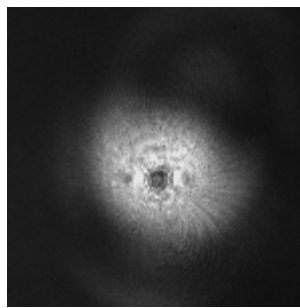
(1)



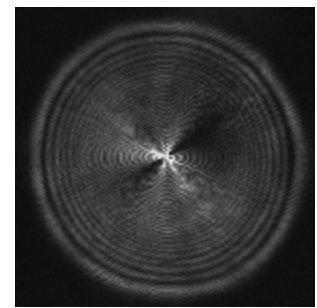
(2)



(3)



(4)



(5)

Figure 5.2a Hollow beam images generated by an axicon and lenses at various positions: (1) just before the axicon, (2) 7 cm after the axicon, (3) 4 cm before the focal point of L_2 , (4) 2 mm before focal point, (5) 3 cm after the focal point.

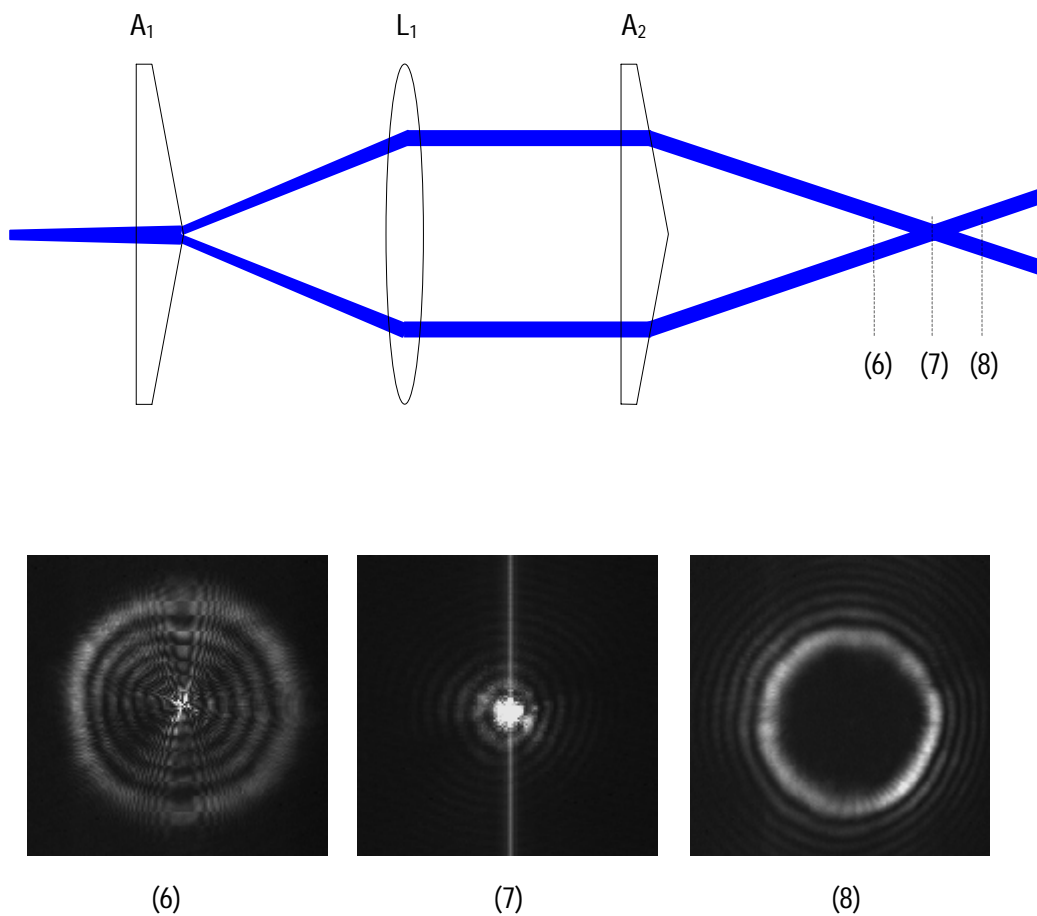


Figure 5.2b Hollow beam images with an axicon (A_2) replacing the second lens (L_2) in Fig. 5.2a. The beam (the outermost ring) crosses at position (7). Positions (6) and (8) are 4 cm before and 3 cm after the beam crosses. The axicons have 3° base angle. L_1 has a focal length of 40 cm and is located 44 cm away from A_1 . L_2 has a focal length of 20 cm and is located 8 cm away from L_1 . The vertical structures in images (2), (3) and (7) are artifacts of the camera as a result of the saturation. The anisotropic power distribution in the images was caused by the ellipticity of the incident beam.

the main ring after the core focus, and the beam is truly hollow as shown in image (8) of Fig. 5.2. The bright spot in image (7) is an intersection of the 0th order ring. The power distribution at this point was shown to be the 0th order Bessel function (J_0) [68]. If a third axicon is located at position 8 of Fig. 5.2, the beam will be nearly collimated, with a nearly constant wall thickness. Figure 5.3 shows the optical setup used for generating a 1 mm hollow beam with both the core and the wall collimated. In this setup we used the second axicon (A_2) twice, making alignment a great deal easier. Precise alignment of the second and third axicons is required to keep the circular beam shape. Misalignment of the first axicon does not affect the beam shape but changes the power distribution. The divergence of the incident beam on the first axicon (A_1) was carefully chosen to have the wall nearly collimated after the collimating lens (L_1). The slight wall and core divergence was corrected by the second simple lens (L_2). This second lens was located about two focal lengths (i.e., 60 cm) from both the third axicon (A_2) and the position where the guiding experiment was performed. The hollow beam after the third axicon was imaged to the experiment position. The core size is determined mainly by the position of the mirror in Fig. 5.3. The core divergence of the beam at the interaction region can be changed by the location of L_1 and the focal length of L_2 .

The image and radial intensity profile of the hollow beam generated by our setup is shown in Fig. 5.4. The intensity profile shows that the axicon generated hollow beam has steep and thin walls with dark cores that extend over most of the beam diameter. This is the most important distinction between the axicon method and other means of generating hollow beams mentioned earlier. Other methods generate TEM_{01}^* like hollow beams that have zero intensity only at the center. The axicon generated hollow beam

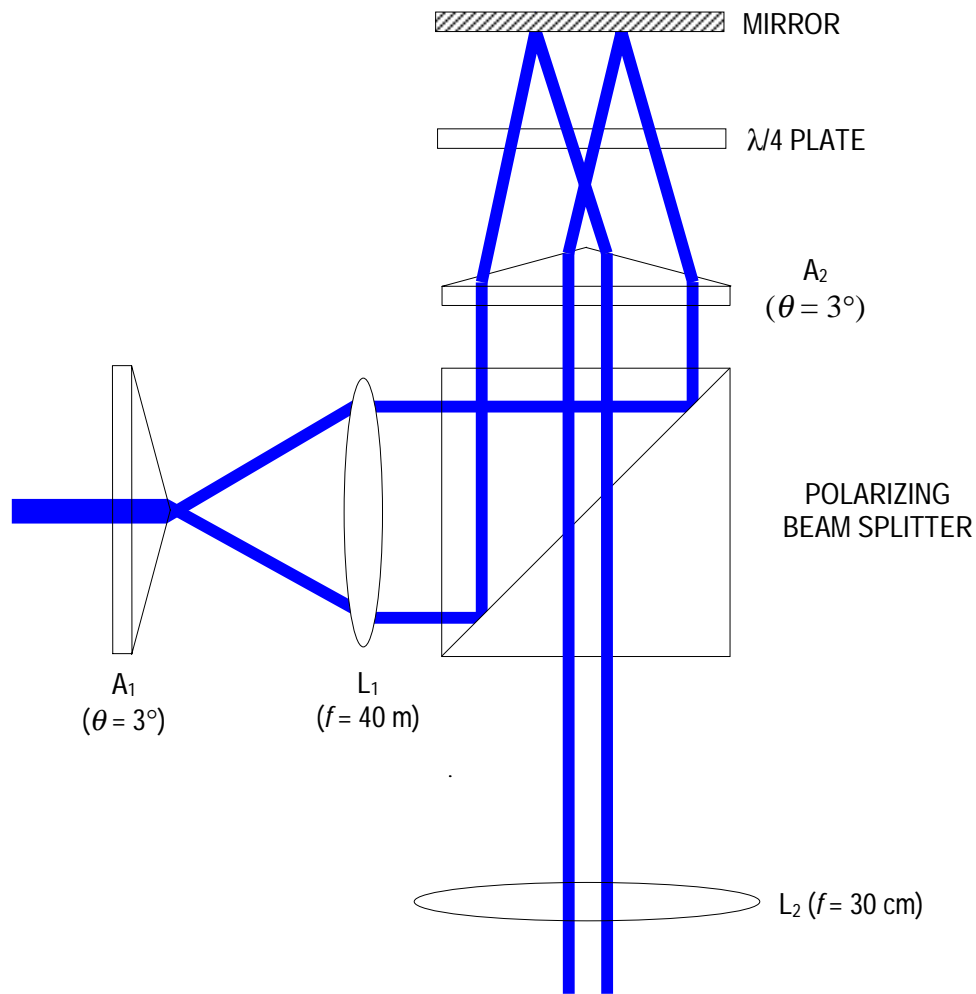


Figure 5.3 The optical setup for generating a collimated hollow beam. The incident beam is the one given in image (1) of Fig. 5.2. The incident beam is vertically polarized and reflected from the beam splitter. The polarization is rotated by 90° after the beam passes twice through the quarter-wave plate.

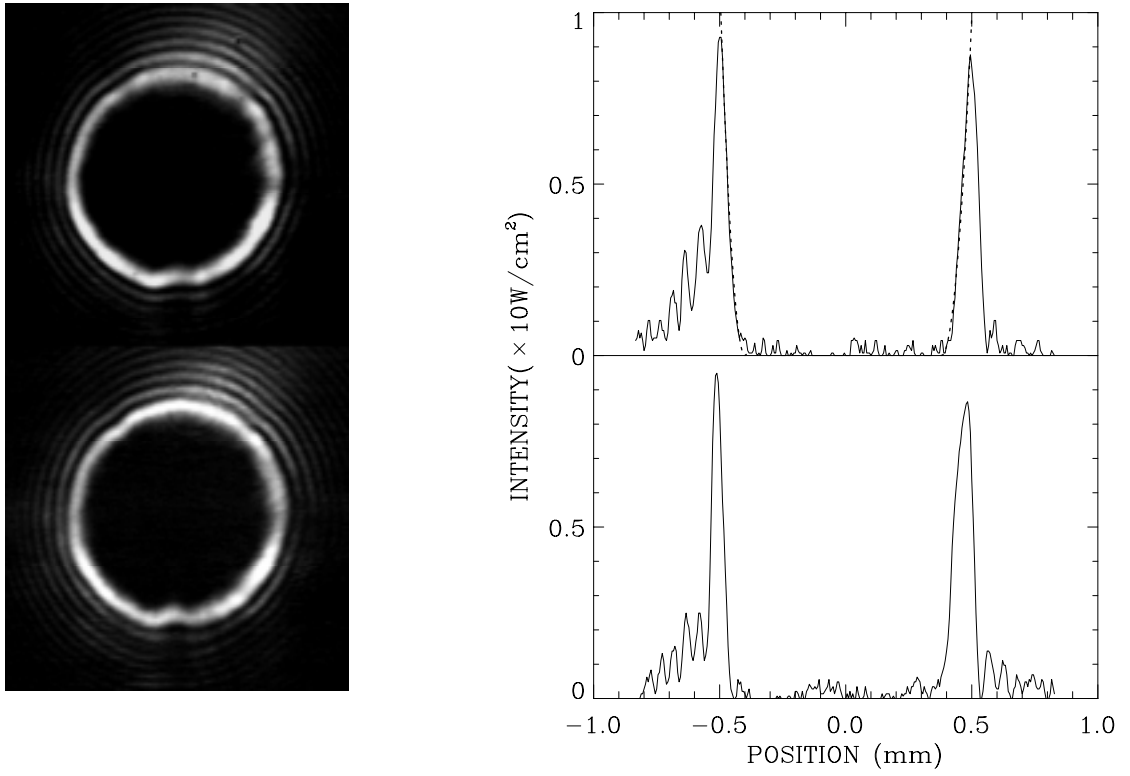


Figure 5.4 Spatial image (left) and radial intensity profile (right) of the axicon generated beam. The two images were separated by 5 cm. The dotted curve is the extended harmonic function with $r_0 = 0.4$ mm and $r_1 = 0.1$ mm (see Fig. 5.5a).

therefore can guide the atoms with minimum interaction or heating. Ultracold atoms in the axicon tunnel spend about 90% of their time in the dark. Another advantage is that the axicon method has a high efficiency.⁵ We can employ most of the incident power in the 0th order ring. Main losses are caused by reflections from the various optical elements, which can be eliminated by AR coatings. Furthermore, most of the power is concentrated in the narrow wall, with the peak intensity much higher than in walls generated by other means. The axicon generated beam has about 3 times higher peak intensity than the apertured beam shown in Fig. 4.12. The axicon method is thus suitable when low power lasers are used. The main wall in Fig. 5.4 can be described well by a Gaussian function:

$$I(r) = I_{\max} \exp\left(-\frac{(r - r_w)^2}{\sigma^2}\right), \quad (5.4)$$

where r_w is the radius of the wall and σ the 1/e width, which is about 40 μm . We find that it is more convenient to approximate the wall by a quadratic function:

$$I(r) = \begin{cases} 0 & , r < r_0 \\ I_{\max} (r - r_0)^2 / r_1^2 & , r_0 < r < r_0 + r_1 \end{cases}, \quad (5.5)$$

⁵ The efficiency of other methods ranges from 20% to 50%.

where r_o is the radius of the zero intensity part (i.e., the hollow core) and r_1 the width of the non-zero intensity part (i.e., the wall) as shown in Fig. 5.5a. The dotted line in Fig. 5.4 shows that this quadratic function overlaps the inner wall well. This ‘extended harmonic potential’ enables us to solve the equation analytically for the evolution of the atoms in the tunnel.

5.2 Evolution of atoms in the hollow beam atom tunnel

5.2.1 The interactions between the atoms and the light wall

In the preliminary experiment we found that the resonance scattering in the hollow beam plays an important role in the propagation of the atom cloud in the tunnel beam. Before we discuss the guiding experiment with our axicon generated hollow beam, we will solve the equations for the interaction between the hollow beam and the light wall. Basically, there are three major interactions to consider.

(1) The first is the dipole interaction between the induced dipole moment of the atoms and the light field, which confines the atoms in the transverse direction. The dipole potential is given in Eq. 2.14 or Eq. 2.16. For convenience, Eq. 2.16 is repeated here:

$$U(r) = \frac{\hbar\Gamma}{2} \cdot \frac{I(r)/I_s}{4q}, \quad (5.6)$$

where $q = \Delta/\Gamma$ is the detuning factor.

(2) The second is the momentum transfer from the photons to the atoms caused by resonance absorption. This accelerates the atoms in the direction of laser propagation (longitudinal direction). The scattering acceleration is given in Eq. 2.11. For large detunings ($\Delta/\Gamma \gg 0.5\sqrt{I/I_s}$), this reduces to:

$$a_{sc} = v_{rec} \cdot \frac{\pi\Gamma I(r)/I_s}{4q^2}. \quad (5.7)$$

Since the laser intensity is a function of position, the acceleration is also position dependent. To determine the center-of-mass acceleration of an atom cloud, we consider an ensemble average of the acceleration. The ensemble average is equivalent to the time averaged acceleration of an atom since the density of atoms at a certain position is proportional to the time they spend there. Therefore, we define the scattering acceleration as:

$$\begin{aligned} \bar{a}_{sc} &\equiv \left\langle v_{rec} \cdot \frac{\pi\Gamma I(r)/I_s}{4q^2} \right\rangle_{ensemble}, \\ &= v_{rec} \cdot \frac{\pi\Gamma I(r_t)/I_s}{4q^2} \cdot \frac{1}{T} \int_0^T \frac{I(r(t))}{I(r_t)} dt \end{aligned} \quad (5.8)$$

where $I(r)$ is the intensity of the laser a distance r away from the axis and r_t the turning point as shown Fig. 5.5a. The last factor in Eq. 5.8, the time average of the normalized

intensity over one period of atomic motion, we call the ‘shape factor’(SF) because it depends mainly on the shape of the hollow beam.

(3) The third is the spontaneous emission. While absorption produces a longitudinal acceleration, the subsequent emission is isotropic and causes the atoms to be heated. As a consequence, the kinetic energy of the ensemble experiences a continual spread in both transverse and longitudinal directions. From Eq. 2.12, the heating rate of the ensemble under the large detuning approximation can be written as:

$$\frac{d\delta K}{dt} = K_{rec} \cdot \frac{\pi \Gamma I(r_t) / I_s}{4q^2} \cdot \frac{1}{T} \int_0^T \frac{I(r(t))}{I(r_t)} dt, \quad (5.9)$$

where $\delta K \equiv m\langle v^2 \rangle / 2$ is the kinetic energy spread.

5.2.2 Shape factor and ensemble heating

In the previous section we saw that the evolution of atoms in the hollow beam depends on the shape of the hollow beam. The shape dependence can be evaluated quantitatively by means of the shape factor defined by:

$$SF \equiv \frac{1}{T} \int_0^T \frac{I(r(t))}{I(r_t)} dt. \quad (5.10)$$

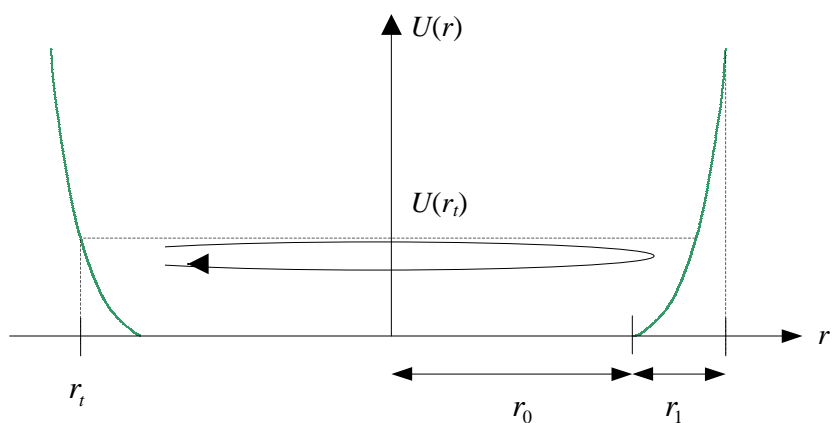
The shape factor can be written in terms of normalized potential instead of normalized intensity since the dipole potential is proportional to the intensity as in Eq. 5.6. Furthermore, the integral over time can be replaced by the integral over position using the energy conservation law, $\frac{1}{2}m\left(\frac{d\bar{r}}{dt}\right)^2 + U(r) = U(r_i)$. Considering only radial motion, SF can be written as:

$$SF = \frac{\int_0^{r_i} \frac{U(r)/U(r_i)}{\sqrt{1-U(r)/U(r_i)}} dr}{\int_0^{r_i} \frac{1}{\sqrt{1-U(r)/U(r_i)}} dr}. \quad (5.11)$$

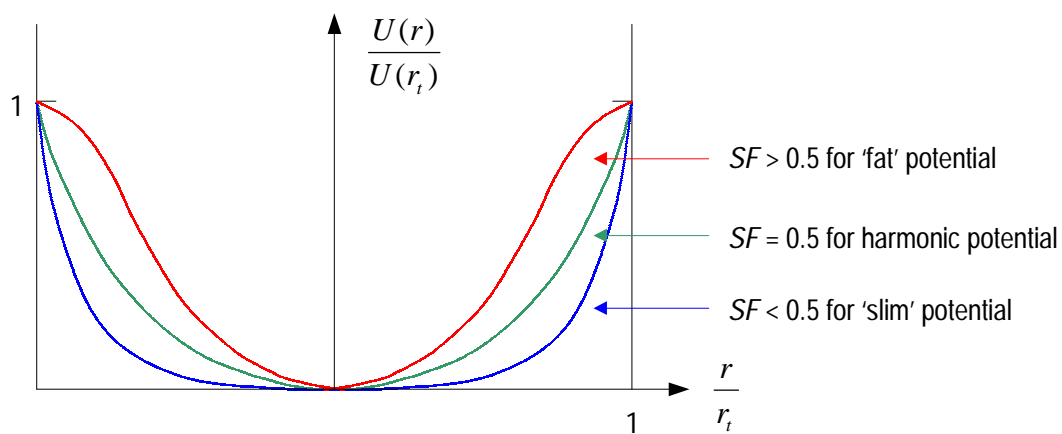
In general, the shape factor depends on the transverse kinetic energy⁶ and the shape of the potential. If the potential were given by a single r^n term, SF would not depend on the transverse kinetic energy but only on the shape of the potential because the r_i terms in the integral can be removed by replacing dr with $d(r/r_i)$. For example, the shape factor for a harmonic potential is always 0.5. As shown in Fig. 5.5b, SF is larger than 0.5 for a ‘fat’.

⁶ ‘Transverse kinetic energy’ is not physically correct terminology because the kinetic energy is a scalar quantity and has no direction. Nevertheless, it is used in this thesis because of its convenience and should be understood as the kinetic energy related to the transverse motion, i.e., $K_{\perp} \equiv \frac{p_{\perp}^2}{2m}$, where p_{\perp} is the transverse momentum. The ‘transverse kinetic energy spread’ will also be defined in the same way,

$$\delta K_{\perp} \equiv \frac{\langle p_{\perp}^2 \rangle}{2m}.$$



(a)



(b)

Figure 5.5 (a) Extended harmonic potential. The potential is zero for $r < r_0$ and quadratic for $r_0 < r < r_1$. The turning point, r_t , is determined by the kinetic energy of the atoms. (b) Shape factor for various potentials. ‘Fat’ potential has a reduced core, and ‘slim’ potential has an extended core.

beam such as the TEM_{01}^* beam and smaller than 0.5 for a ‘slim’ beam such as the axicon-generated beam. In principle, the square potential has a shape factor of almost zero, which means the atoms do not scatter photons at all. The shape factor for a TEM_{01}^* mode is shown in Fig. 5.6. When the transverse kinetic energy is small, the atoms move near the axis where the potential is harmonic and $SF \approx 0.5$. As the transverse kinetic energy increases, the shape factor increases almost linearly. The reason for the steep increase in the shape factor near $K_{\perp} \approx U_{max}$ is that the potential is flat at the peak. A small increase in the transverse kinetic energy results in far more photon scattering near the flat potential than anywhere else.

The shape factor for the extended harmonic potential given in Eq. 5.5 can be calculated analytically from Eq. 5.11:

$$SF = \frac{0.5}{\frac{2r_0}{\pi r_1} \cdot \sqrt{\frac{U_{max}}{\delta K_{\perp}} + 1}}, \quad (5.12)$$

where δK_{\perp} is the transverse energy spread. The factor of 0.5 in the numerator comes from the non-zero intensity part of the potential (i.e., the wall), which is harmonic. The first term in the denominator is the ratio between the time spent in the core (T_0) and the time spent in the wall (T_1). Eq. 5.12 agrees with the original definition of the shape factor in Eq. 5.10, which gives $SF = 0.5 T_1/(T_0+T_1) = 0.5/(T_0/T_1+1)$.

Using Eq. 5.6 and Eq. 5.12, the acceleration (Eq. 5.8) and the heating rate (Eq. 5.9) can be rewritten as:

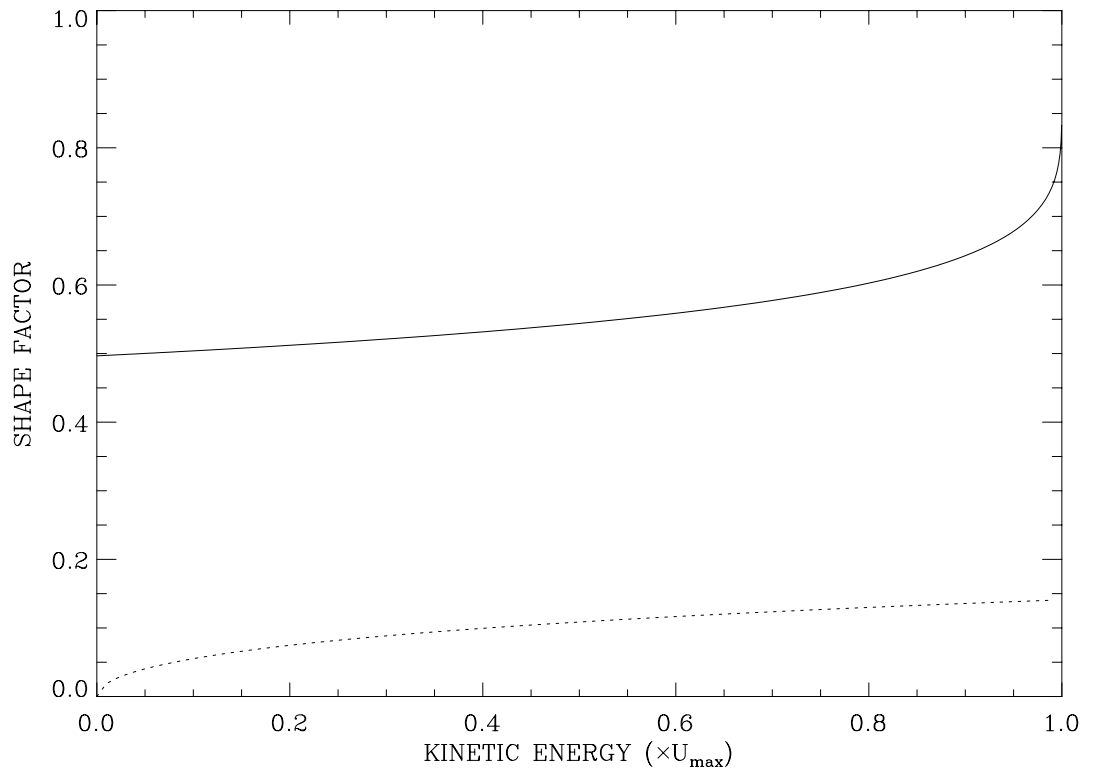


Figure 5.6 Shape factor for TEM₀₁* beam (solid curve) and the axicon beam (dashed curve) calculated using Eq. 5.11. The x -axis is the transverse kinetic energy spread in terms of the maximum potential. The shape factor for TEM₀₁* beam increases from 0.5 almost linearly until the energy spread reaches $\sim 90\%$ of the peak potential. The shape factor for the extended harmonic potential increases rapidly near $\delta K_{\perp} = 0$ and linearly elsewhere. The axicon beam has ~ 10 times smaller SF than TEM₀₁* beam for the MOT temperature.

$$\bar{a}_{sc} = \frac{\pi\Gamma v_{rec}}{2q} \frac{\xi}{\frac{2r_0}{\pi r_1} \sqrt{\frac{u_{max}}{\xi} + 1}}, \quad (5.13)$$

$$\frac{d\xi}{dt} = \frac{2}{3} \cdot \frac{\pi\Gamma}{2q} \cdot \frac{K_{rec}}{h\Gamma/2} \cdot \frac{\xi}{\frac{2r_0}{\pi r_1} \sqrt{\frac{u_{max}}{\xi} + 1}}, \quad (5.14)$$

where the dimensionless quantities $\xi \equiv \delta K_{\perp}/(h\Gamma/2)$ and $u_{max} \equiv U_{max}/(h\Gamma/2)$ are the transverse kinetic energy spread and the maximum potential energy in terms of the Doppler limit. The quantity $K_{rec}/(h\Gamma/2)$ is the ratio between the recoil limit and the Doppler limit. For Cs, it is $(v_{rec}/v_D)^2 = (0.36/8.7)^2 = \sim 1/600$. Equation 5.14 gives the heating rate only in the transverse direction which we are mainly interested in. After a time τ , the tunnel hold time, $\delta K_{\perp} = U_{max}$, and the tunnel will become leaky. The factor of $2/3$ in Eq. 5.14 is due to the fact that there are two dimensions in the transverse direction. The energy spread in the longitudinal direction is just half the spread in the transverse direction.

The hollow beam used for the preliminary experiment can also be approximated by an extended harmonic potential. The shape factor for the solid aperture beam is assessed at ~ 0.058 . From the scattering acceleration of 13 m/s^2 extracted from the shadow images, I find $SF = 0.054$, in good agreement with the analytic determination. This agreement suggests that our one-dimensional model captures most of the dynamics between the atoms and the tunnel.

5.2.3 Maximum hold times and optimum detuning

The transverse kinetic energy spread as a function of time can be obtained by solving Eq 5.14. But, Eq.5.14 is more easily solved for time t as a function of the kinetic energy ξ . The solution for $t(\xi)$ is given by:

$$t = \frac{3q}{\pi\Gamma} \cdot \frac{h\Gamma/2}{K_{rec}} \cdot \left[\frac{4r_0}{\pi r_1} \sqrt{u_{\max}} (\xi_0^{-0.5} - \xi^{-0.5}) + \ln\left(\frac{\xi}{\xi_0}\right) \right]. \quad (5.15)$$

where $\xi_0 \equiv \delta K_{\text{MOT}}/(h\Gamma/2)$ is the initial kinetic energy spread in terms of the Doppler limit. The second term in the above solution comes from the harmonic part (the wall). When the core is reduced to zero length (i.e. $x_0 = 0$), Eq. 5.15 can be solved for the kinetic energy spread, which is an exponential function of time. As the atoms are heated in a harmonic potential, they move to higher parts of the potential, and the heating rate increases. This process leads to an exponential increase of the kinetic energy spread. The first term is the contribution by the dark core. As the size of the dark core (r_0) increases, this term overwhelms the second term, and the kinetic energy spread increases more slowly because the heating is suppressed.

The hold time is defined as the time when the kinetic energy spread becomes equal to the potential height: $\tau \equiv t(\xi = u_{\max})$. If we define another dimensionless constant $\zeta = \xi_0 / u_{\max} = 4q\xi_0 I_s / I_{\max}$, the hold time can be written as:

$$\tau = \frac{3I_{\max}}{4\pi\Gamma I_s \xi_0} \cdot \frac{h\Gamma/2}{K_{rec}} \cdot \left[\frac{4r_0}{\pi r_1} (\zeta^{0.5} - \zeta) + \zeta \ln(\zeta^{-1}) \right]. \quad (5.16)$$

The optimum detuning that maximizes the hold time is found by differentiating Eq. 5.16 with respect to ζ . The differential equation $d\tau/d\zeta = 0$ can be written as:

$$\frac{4r_0}{\pi r_1} (0.5\zeta^{-0.5} - 1) - \ln(\zeta) - 1 = 0. \quad (5.17)$$

The value of ζ that satisfies Eq. 5.17 is a function of r_0/r_1 , which is the ratio between the core and wall sizes. If the core is extended to most of the hollow beam size (i.e., $r_0/r_1 \rightarrow \infty$, and the potential is almost square), the equation is dominated by the first term and $\zeta \approx 0.25$. In the other limit where the core is reduced to zero length (i.e., $r_0/r_1 \rightarrow 0$, and the potential is harmonic), the first term is negligible, and $\zeta \approx 1/e = 0.37$. In general, the equation has a solution between these two extremes, $0.25 < \zeta < 0.37$. Therefore, the optimum detuning is in the range:

$$0.25 \times \frac{I_{\max}/I_s}{4\xi_0} < q_{\text{opt}} < 0.37 \times \frac{I_{\max}/I_s}{4\xi_0}. \quad (5.18)$$

The axicon generated beam is very close to a square well potential and has $\zeta \approx 0.28$. In the large core size limit ($r_0/r_1 \rightarrow \infty$), the hold time goes to infinity, which means the atoms stay in the hollow beam forever. This agrees with our intuition because the

atoms remain generally in the dark and do not scatter photons. The hold time also increases as the MOT temperature decreases ($\xi_0 \rightarrow 0$) and the potential increases ($I_{\max} \rightarrow \infty$).

Compared to the detuning that maximizes the potential ($q_0 \approx 0.25\sqrt{I_{\max}/I_s}$, see Eq. 2.15), the optimum detuning in Eq. 5.18 is much larger. For the extended harmonic potential, q_0 is about 25 ($\Delta \sim 75$ MHz) and q_{opt} is about 600 ($\Delta \sim 3$ GHz). At the small detuning of 75 MHz, heating is very large, reducing the hold time. And, as shown in the preliminary experiment, the MOT and the tunnel cannot coexist at detunings less than 100 MHz because the atoms are excluded from the MOT position. It is clear that the tunnel beam cannot be detuned too far because the potential would be too small.

The existence of a finite optimum detuning can also be understood graphically. Figure 5.7 shows an increase in the transverse kinetic energy spread as a function of time at various detunings (a) for the TEM_{01}^* beam and (b) for the axicon generated beam. The same power and size for the two potentials were assumed. The diamonds at the intersection of the potential (dotted lines) and the kinetic energy (solid curves) determine the hold time. The axicon tunnel has a maximum hold time about 20 times larger than the TEM_{01}^* tunnel. The atoms are heated more slowly in the axicon generated beam than in the TEM_{01}^* beam. The hold time for the axicon tunnel is maximized at $q_{\text{opt}} = 573$. The maximum hold time at this detuning is about 0.37 sec. The ultracold atoms, however, cannot stay in the tunnel this long because they would travel several meters due to the scattering acceleration for this 0.37 sec time period. It is not possible to make a 1 mm hollow beam that is collimated for meters. But, this analysis can still be used to predict the trap times in hollow beam atom traps [69]. According to this analysis, we know that

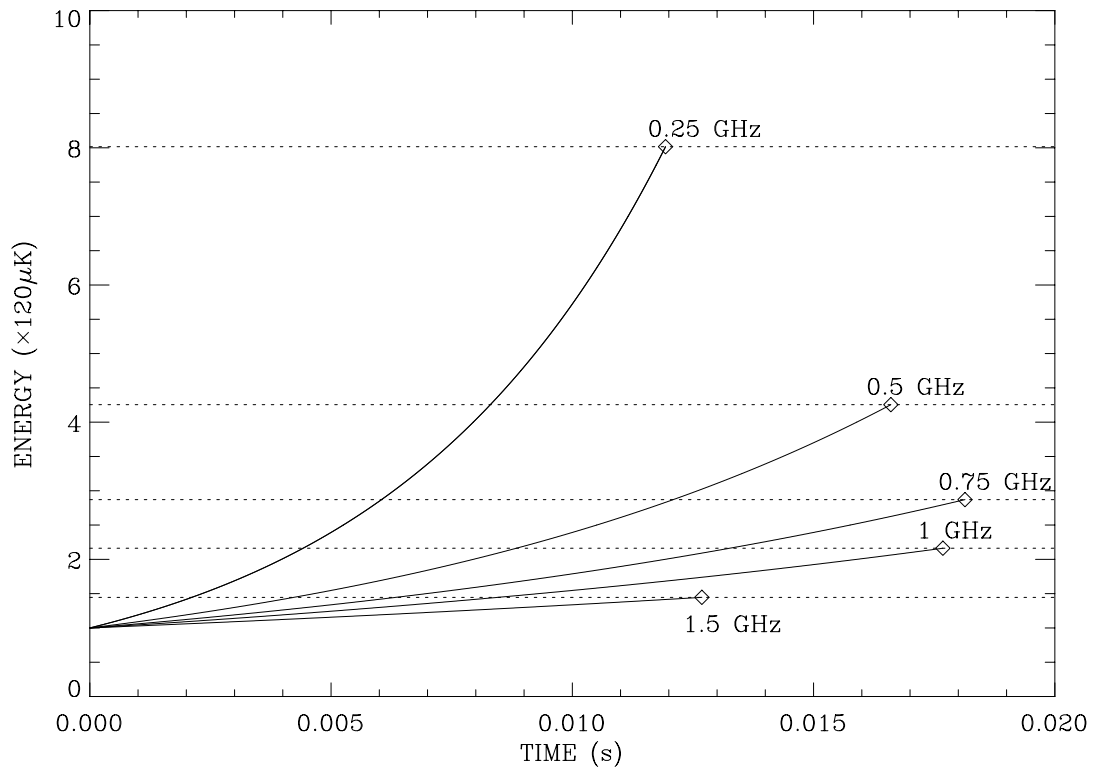


Figure 5.7a Increase in the transverse kinetic energy spread in a TEM_{01}^* donut mode beam. The same total power (40 mW) and peak-to-peak diameter (1 mm) as the axicon generated beam in Fig. 5.5 was assumed. The peak intensity is 1.9 W/cm^2 . The horizontal lines are potential heights at different detunings. The diamonds determine the hold times ($\delta K_{\perp}(\tau) = U_{\text{max}}$). The maximum hold time is $\tau_{\text{max}} = 18 \text{ ms}$ at $q_{\text{opt}} = 162$ ($\Delta = 810 \text{ MHz}$).

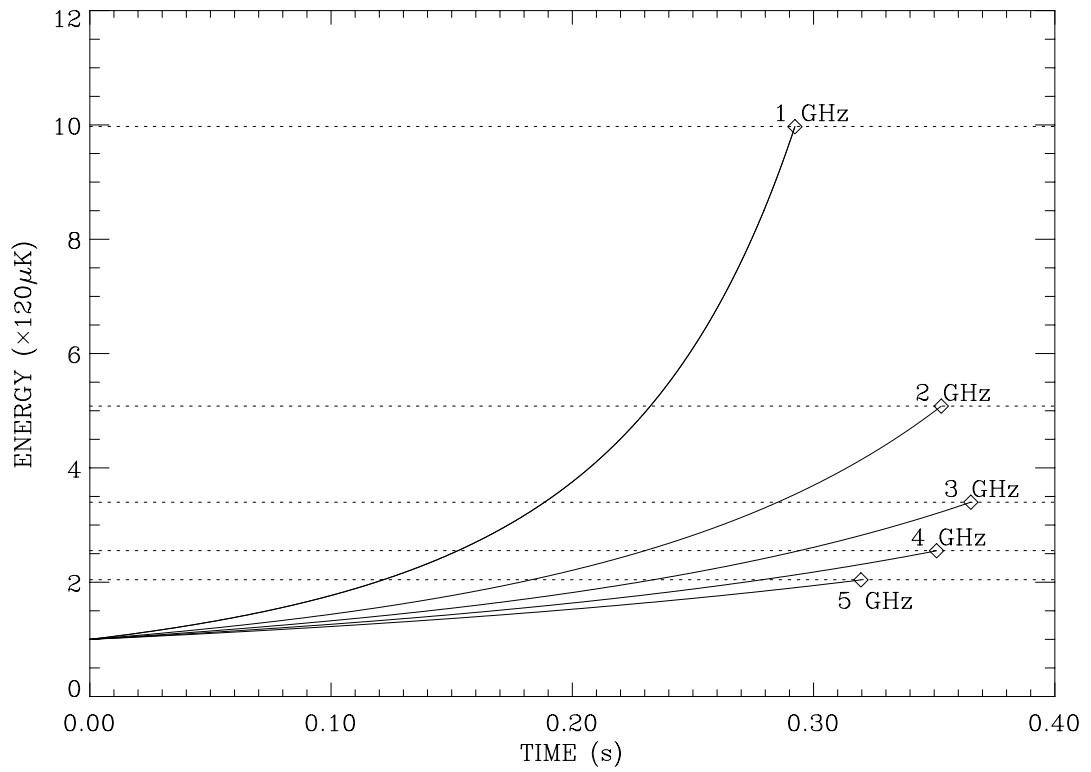


Figure 5.7b Increase in the transverse kinetic energy spread in our axicon generated hollow beam shown in Fig. 5.4. The maximum hold time is $\tau_{\text{max}} = 365$ ms at $q_{\text{opt}} = 573$ ($\Delta = 2.87$ GHz).

the atoms would stay in the tunnel beam with the kinetic energy spread almost unchanged up to 150 milliseconds if we guide our cold atoms for ~ 20 cm as will be described in Ch. 6. In guiding experiments, therefore, the optimum detuning is not necessarily the one that maximizes the hold time. Rather, it should be considered how much acceleration is needed to transport the atoms effectively. If the acceleration is too small, the transport time will be long and the atom cloud will be elongated in the longitudinal direction, which reduces the beam flux. And in case we want to send the atoms upward, the scattering acceleration should be larger than the gravitational acceleration. The detuning that gives the scattering acceleration equal to the gravitational acceleration is about 1 GHz. With larger detuning, we will lose control over gravity. Furthermore, if the transport time is too long, significant number of atoms can be lost by optical pumping and collisions with the background atoms.

While the atoms are heated by the light walls, they can be cooled via inelastic reflections from the walls [70, 71]. However this Sisyphus cooling is effective only when the resonance scattering is close to one per reflection [72, 67], which is true of very steep potential walls such as in an evanescent wave guide [73]. In our tunnel, the resonance scattering rate is several tens per reflection. To reduce the scattering rate, much larger detuning (hundreds of GHz) is required. In that case, the potential is too low to confine the atoms unless higher powered lasers are used.

CHAPTER 6

ALL-LIGHT ATOM TUNNEL

This chapter describes guidance of ultracold atoms from a MOT for ~ 20 cm with an axicon generated hollow beam. The evolution of the atom cloud in the tunnel was monitored by shadow images in both transverse and longitudinal directions. With appropriate detuning, the atoms could be levitated by directing the tunnel beam against gravity. The primary loss mechanism was found to consist of collisions with the warm background atoms. This chapter concludes with suggestions for enhancing the guiding efficiency and the beam flux.

6.1 Horizontal images and scattering acceleration

Having prepared a diffractionless hollow beam and developed a theory for guiding cold atoms, I performed an atom guide experiment. The experimental setup was almost the same as the one for the preliminary experiment shown in Fig. 4.11, except that the crude hollow beam was replaced by the axicon generated hollow beam.

First, I took shadow images of the atom cloud in the transverse (horizontal) direction for detunings from $\Delta = 0.25$ GHz to 2 GHz. A series of images for $\Delta = 250$ MHz, 1 GHz, 2 GHz ($q = 50, 200, 400$) are shown in Fig. 6.1. The images were stopped at 40 ms (30 ms for $\Delta = 0.25$ GHz) because (1) the atoms started to fall out of the screen about these times, and (2) the cloud became too dilute to be seen by its shadow.

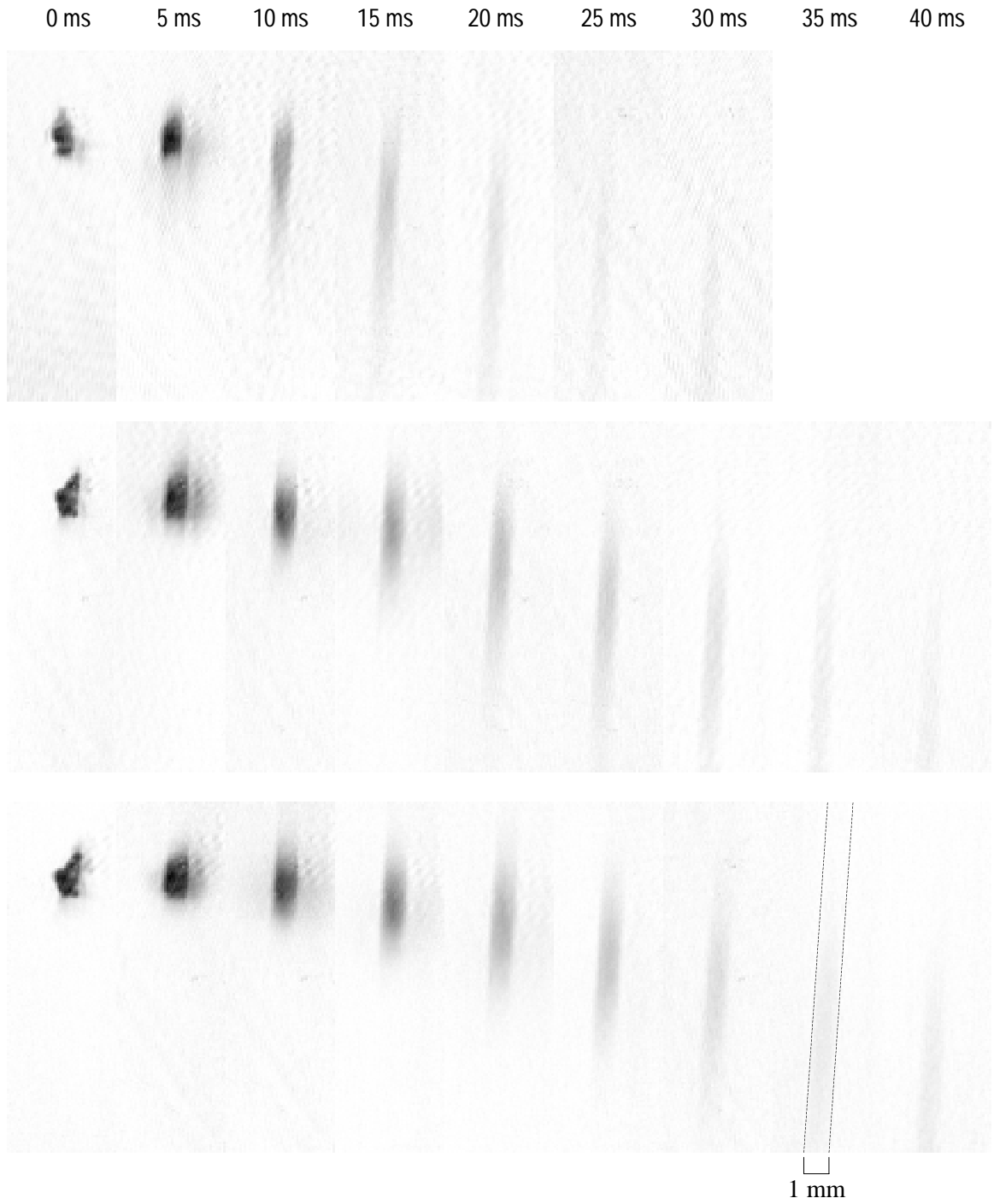


Figure 6.1 Transverse shadow images of the atom clouds in a tunnel beam directed downward for $\Delta = 0.25$ GHz (top), $\Delta = 1$ GHz (middle) and $\Delta = 2$ GHz (bottom). The dashed lines indicate the tunnel beam.

The shadows for $\Delta = 0.25$ GHz faded away more quickly than the others. The reason is that the atoms were lost by optically pumping to the lower hyperfine state. The repumping beam for the MOT was about 1 cm in diameter. After the atoms fell out of the repumping beam, they could be pumped into the $F=3$ hyperfine level where they were no longer confined by the tunnel beam. At smaller detunings, the atoms experienced more rapid optical pumping to the $F=3$ hyperfine level and were more quickly lost from the tunnel. Another reason is that with small detuning the atoms expand faster in the longitudinal direction, as will be explained later (see Eq. 6.3).

The temperature of the MOT in this experiment was measured by taking shadow images without the tunnel beam; it was determined to be ~ 80 μK . The MOTs were nearly round without the tunnel beam. With the tunnel beam superimposed on the MOT, the edge was cut off and the shape was deformed as shown in the images at 0 ms. Some atoms trapped in the MOT were outside the tunnel beam and were expelled when the trapping beams were extinguished (see the shadows outside the tunnel beam at 5 ms). While the atoms in the MOT have a Gaussian spatial distribution, after spending some time in the tunnel they have a nearly square distribution in the transverse direction as explained in Ch. 4. Since we are looking at the atoms in a cylindrical container from the side, the transverse distribution will be $f(x) \sim \sqrt{r^2 - x^2}$, where r is the radius of the tunnel beam and x the distance from the propagation axis. A typical distribution in the transverse direction is shown in Fig. 6.2.

From the transverse images we can derive the longitudinal position of the center-of-mass of the atom cloud. Fig. 6.3 shows the positions as a function of time for the three

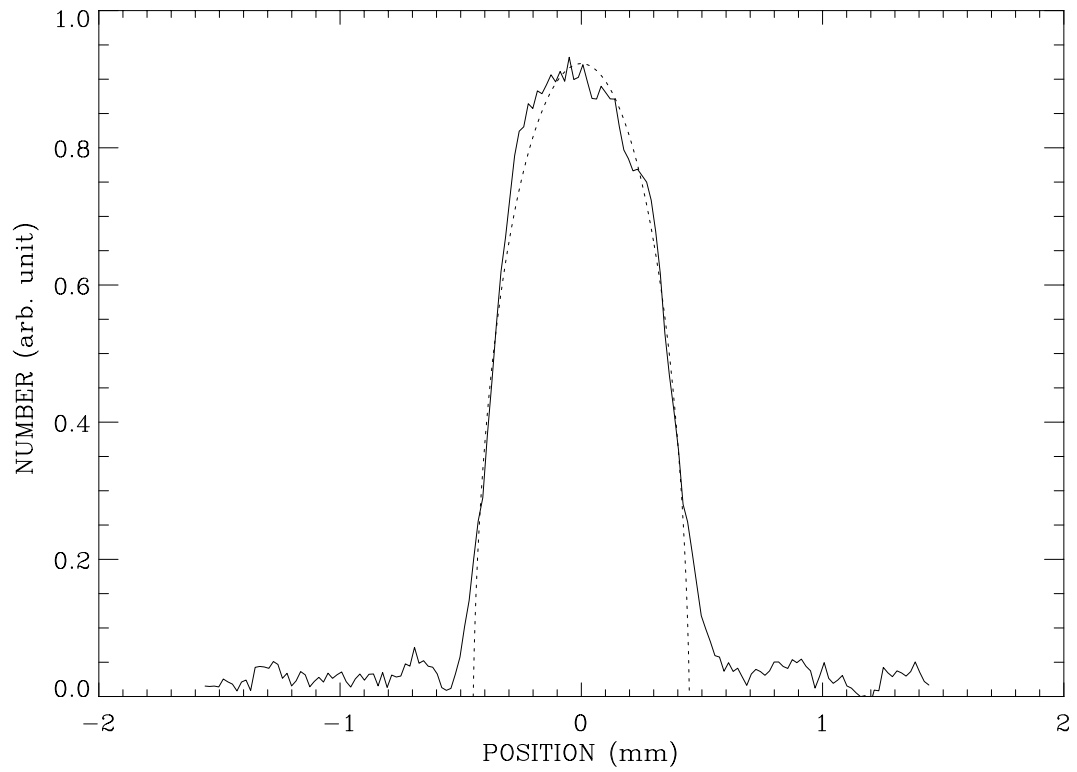


Figure 6.2 Transverse density profile of an atom cloud in the tunnel. The solid curve is the line profile across the image at $t = 25\text{ms}$ with $\Delta = 2\text{GHz}$ of Fig. 6.1. The dotted curve is proportional to $\sqrt{r^2 - x^2}$ where r is the radius of the tunnel and x the distance from the axis.

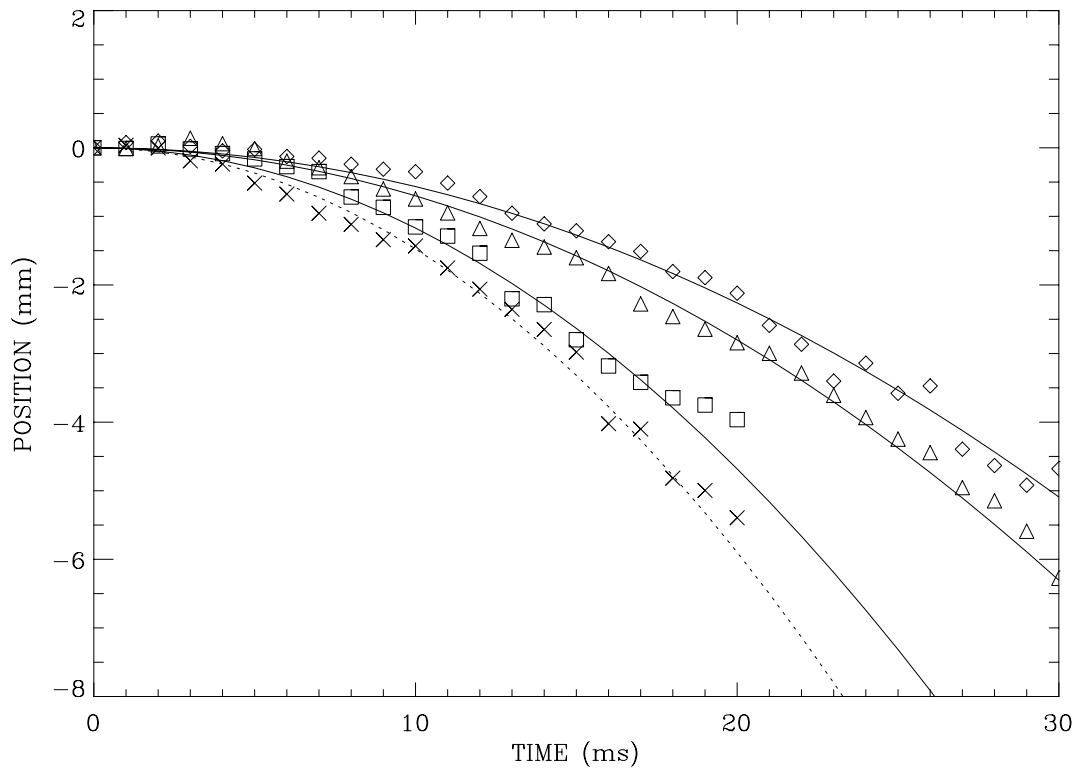


Figure 6.3 Vertical position of the atom clouds for $\Delta = 0.25$ GHz (\square), 1 GHz (\triangle), 2 GHz (\diamond) at $T \approx 80 \mu\text{K}$, and $\Delta = 1$ GHz at $T \approx 140 \mu\text{K}$ (\times). The data points are shown until the atoms start to fall out of the screen. The solid curves represent falls with $a = g + a_{sc} = 23.4, 14.0, 11.3 \text{ m/s}^2$ respectively. The dotted line represents for $a = 29.5 \text{ m/s}^2$.

detunings. The data are shown only up to 30 ms since the position cannot be determined after some atoms fall out of the screen. The scattering accelerations deduced from Fig. 6.3 are shown in Fig. 6.4. The acceleration for other detunings (not shown in Fig 6.3) are plotted here to show the dependence on the detuning. The solid curve is the theoretical curve from Eq. 5.13 and agrees well with the experimental data. To understand qualitatively the dependence of a_{sc} on other parameters, we take a closer look at Eq. 5.13. At large detuning, the first term in the denominator of Eq. 5.13 is much larger than unity. The scattering acceleration can therefore be approximated as:

$$\bar{a}_{sc} = \frac{\pi\Gamma v_{rec}}{2q} \cdot \frac{\xi}{\frac{2r_1}{\pi r_0} \sqrt{\frac{u_{max}}{\xi}}} \quad (6.1)$$

The dotted curve in Fig. 6.4 represents this approximation. Using the definition of $u_{max} = U_{max}/(h\Gamma/2) = I/(4qI_s)$, Eq. 6.1 can be rewritten as:

$$\bar{a}_{sc} = \frac{\pi^2\Gamma v_{rec}}{2} \cdot \frac{r_1}{r_0} \cdot \frac{\xi^{1.5}}{q^{0.5} (I_{max}/I_s)^{0.5}} \quad (6.2)$$

Equation 6.2 shows how the scattering acceleration scales with various parameters. Dependence of \bar{a}_{sc} on the core and wall sizes (r_0 , r_1) can be easily understood. Compared with Eq. 5.7, dependence on the detuning is reduced to $\bar{a}_{sc} \propto 1/\sqrt{\Delta}$ to first

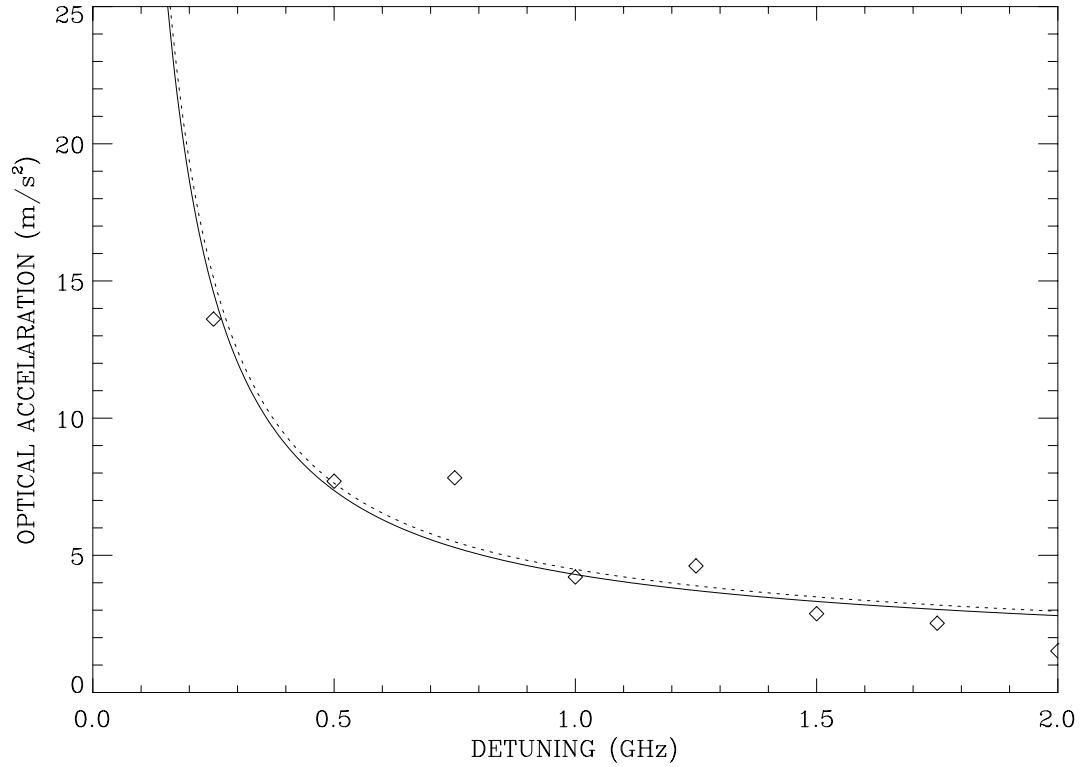


Figure 6.4 Scattering acceleration of the atom clouds at $T \approx 80 \mu\text{K}$ with different detunings of the tunnel beam. The solid curve represents the theoretical values in Eq. 5.13. The dotted line is the approximation in Eq. 6.1.

order. The strong dependence on the temperature ($T \propto \xi$) is worth notice. The reason is that the atoms with larger transverse kinetic energy penetrate the potential more deeply and frequently and therefore scatter more photons. The data points marked by \times in Fig. 6.3 show the positions of the atom cloud with $\Delta = 1\text{GHz}$, $T \sim 140 \mu\text{K}$. The scattering acceleration deduced from this plot is about 19.7 m/s^2 , a good deal larger than the acceleration (4.2 m/s^2) with $\Delta = 1\text{GHz}$, $T \sim 80 \mu\text{K}$.

While the q and ξ dependence agrees qualitatively with our intuition, the inverse dependence to the maximum intensity (or total power) is quite surprising at first glance. In usual situations, the scattering acceleration increases as the laser intensity increases as shown in Eq. 5.7. This mystery can be understood by noticing that the maximum intensity in Eq. 5.7 is not the intensity experienced by the atoms. The intensity that the atoms experience depends on the transverse kinetic energy of the atoms. If the power of the beam increases while the shape of the tunnel is unchanged, the potential wall becomes steeper, and the time that the atoms spend climbing up and down the wall decreases. Therefore, the average scattering rate over one round trip decreases.

Another quantity we can measure from the images is the longitudinal size; this reveals the temperature and the heating of the atoms. Fig. 6.5 shows the longitudinal size of the clouds. The temperature increase due to the optical heating for the first few tens of milliseconds is negligibly small as discussed in previous chapter. However, the expansion of the atom cloud deviates from the free expansion, especially at small detunings. The reason is that atoms at different horizontal temperatures are subject to different accelerations. The atoms at the sigma point of the velocity distribution will be accelerated under both gravity and the scattering acceleration in Eq. 5.13 while atoms

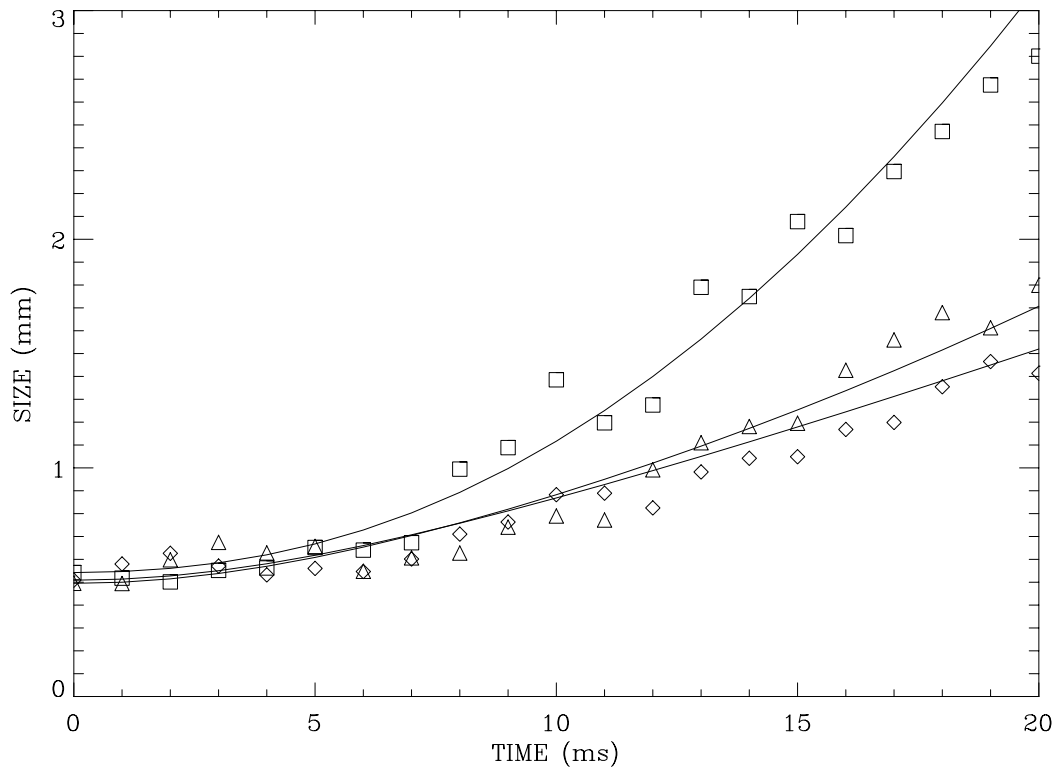


Figure 6.5 Longitudinal size of the atom clouds in the tunnel for $\Delta = 0.25$ GHz (\square), 1 GHz (\triangle), 2 GHz (\diamond) at $T \approx 80$ μ K. The solid curves are the theoretical values given by Eq. 6.3, with scattering accelerations corresponding to the detunings.

with zero transverse velocity fall under gravity only. Therefore, the longitudinal size of the atom cloud as a function of time is:

$$\sigma(t) = \sqrt{\sigma(0)^2 + (v_{z,rms} t)^2 + (0.5a_{sc} t^2)^2}, \quad (6.3)$$

where $v_{z,rms}$ is the root mean square velocity in the longitudinal direction. The solid curves in Fig. 6.5 represent the theoretical values given by Eq. 6.3.

6.2 Levitating the atoms

The optical acceleration observed in our tunnel experiment covered a range from $\sim 3 \text{ m/s}^2$ to $\sim 15 \text{ m/s}^2$ depending on the detuning and the temperature. From this we realized that the atoms could be launched upward and levitated by reversing the direction of the tunnel beam. Fig. 6.6 shows shadow images at $\Delta = 0.25, 1$ and 1.75 GHz . The shadow images for $\Delta = 0.25 \text{ GHz}$ show that the center-of-mass position moves upward while some atoms with small transverse velocity stay near the MOT position. The positions measured from these images are shown in Fig. 6.7. The atoms for $\Delta = 1 \text{ GHz}$ stay near the initial position showing thermal expansion. For $\Delta > 1 \text{ GHz}$, the atoms fell since the optical acceleration was smaller than the gravitational acceleration.

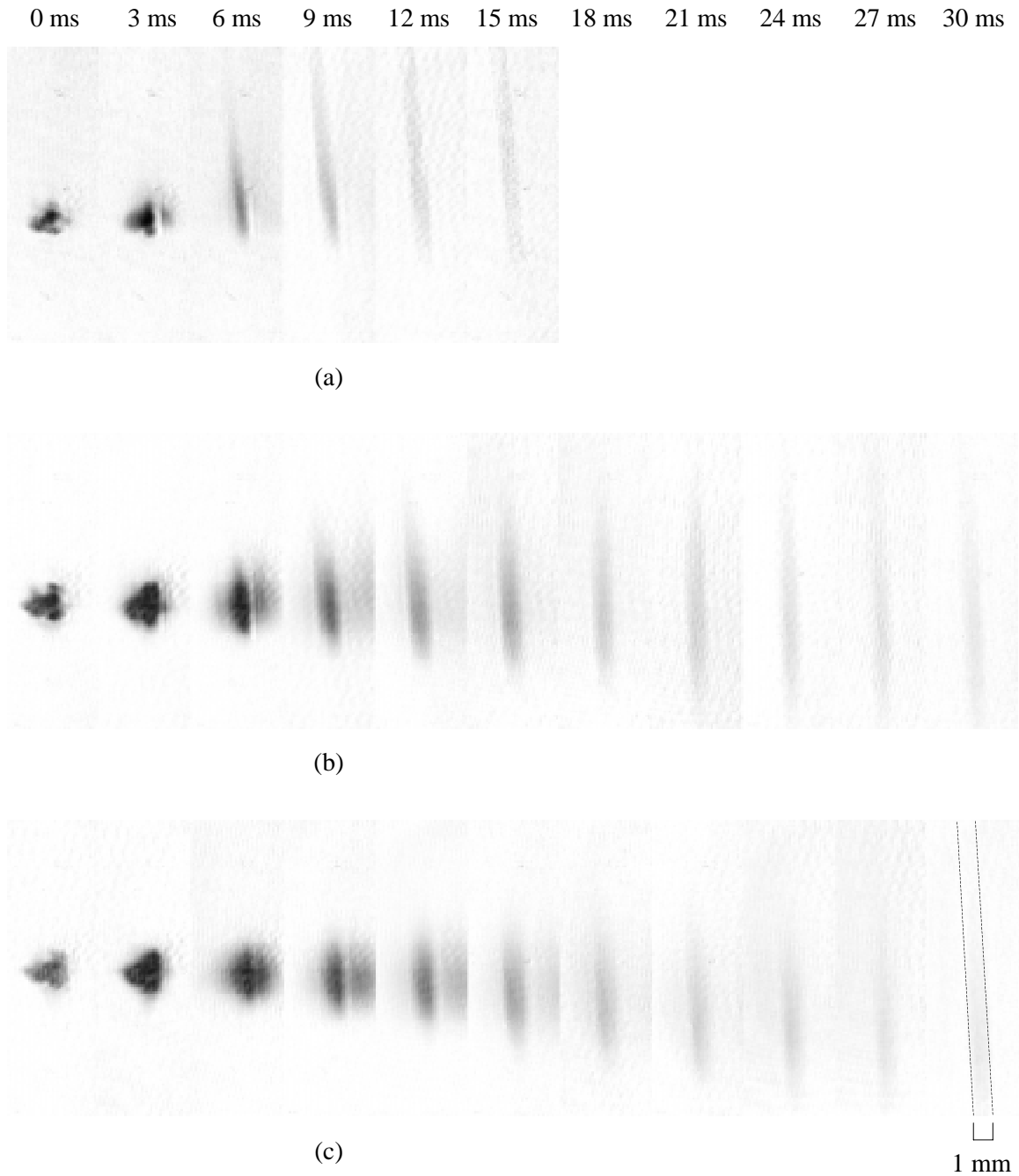


Figure 6.6 Transverse shadow images of the atoms clouds in the tunnel beam directed upward for (a) $\Delta = 0.25$ GHz, (b) $\Delta = 1$ GHz and (c) $\Delta = 1.75$ GHz. The dashed lines indicate the tunnel beam.

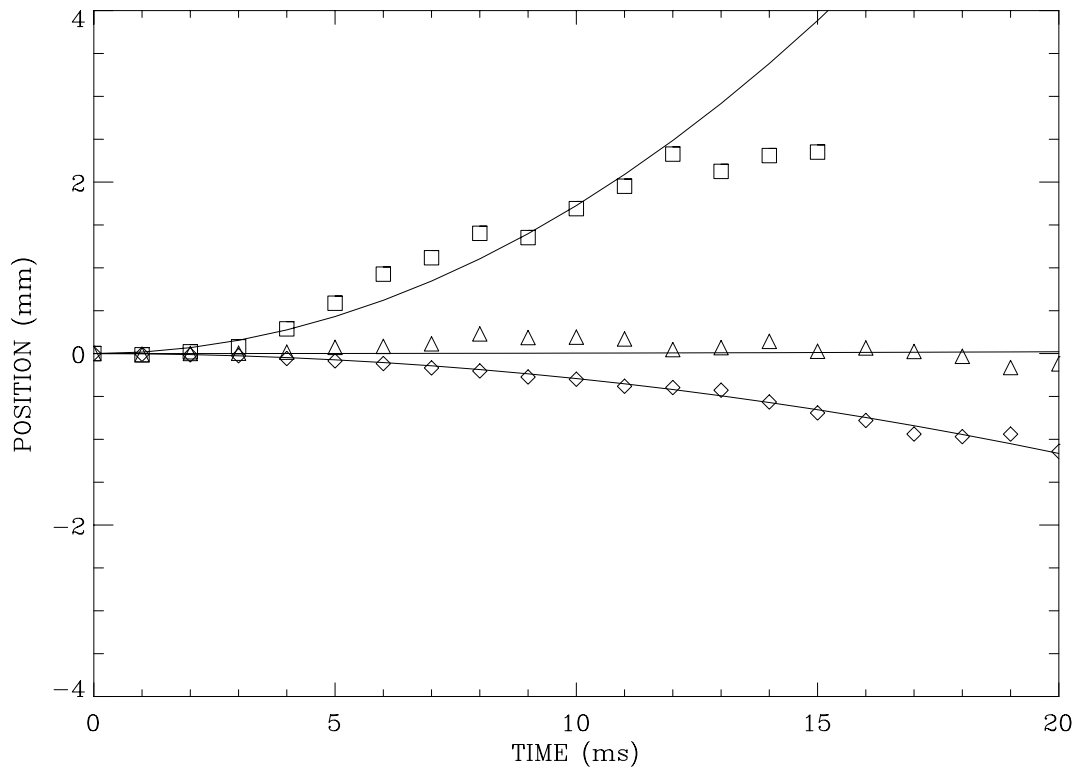


Figure 6.7 Vertical position of the atom clouds in the tunnel directed upward for $\Delta = 0.25$ GHz (\square), 1 GHz (\triangle), 1.75 GHz (\diamond). The positions at 13, 14 and 15 ms for $\Delta = 0.25$ GHz deviate from the solid curve because some atoms are out of the screen.

6.3 Longitudinal images and loss mechanism

As discussed before, monitoring the atoms by transverse imaging was limited by the thermal expansion in the longitudinal direction. After about 60 ms, the atom cloud became too dilute to be seen by its shadow. We needed a different detection scheme. We soon realized that the shadow imaging could be extended by changing the direction of view. This was possible by combining and separating the tunnel and probe beams with polarizing beam splitters as shown in Fig. 6.8. The polarization of the two beams was made perpendicular to each other.

The longitudinal shadow images are shown in Fig. 6.9. The images in Fig. 6.9a were photographed without the repumping beam except near the MOT position while the images in Fig. 6.9b were photographed with the repumping beam co-propagating with the tunnel beam. To maximize the number of atoms loaded into the tunnel, the MOT was made in the shape of a cigar with a major axis 3-4 times as long as the minor axis. This was done by making two of the MOT trapping beams intersect at more than 90° as explained in Ch. 4. The optical depth in the longitudinal direction is proportional to the number density integrated along the longitudinal direction, $f(x, y) \equiv \int f(x, y, z) dz$. The monitoring time, therefore, can be maximized by increasing the vertical length of the MOT. As a result the shadow images were saturated for the first 40 ms. The bright circles around the atom cloud at early times were the tunnel wall. Some atoms were trapped in the MOT outside the tunnel. Consequently the diameter of the atom cloud changed substantially as the atoms flew away between 0 and 20 ms. The largest number of atoms was guided when the MOT diameter was a little larger than the tunnel diameter.

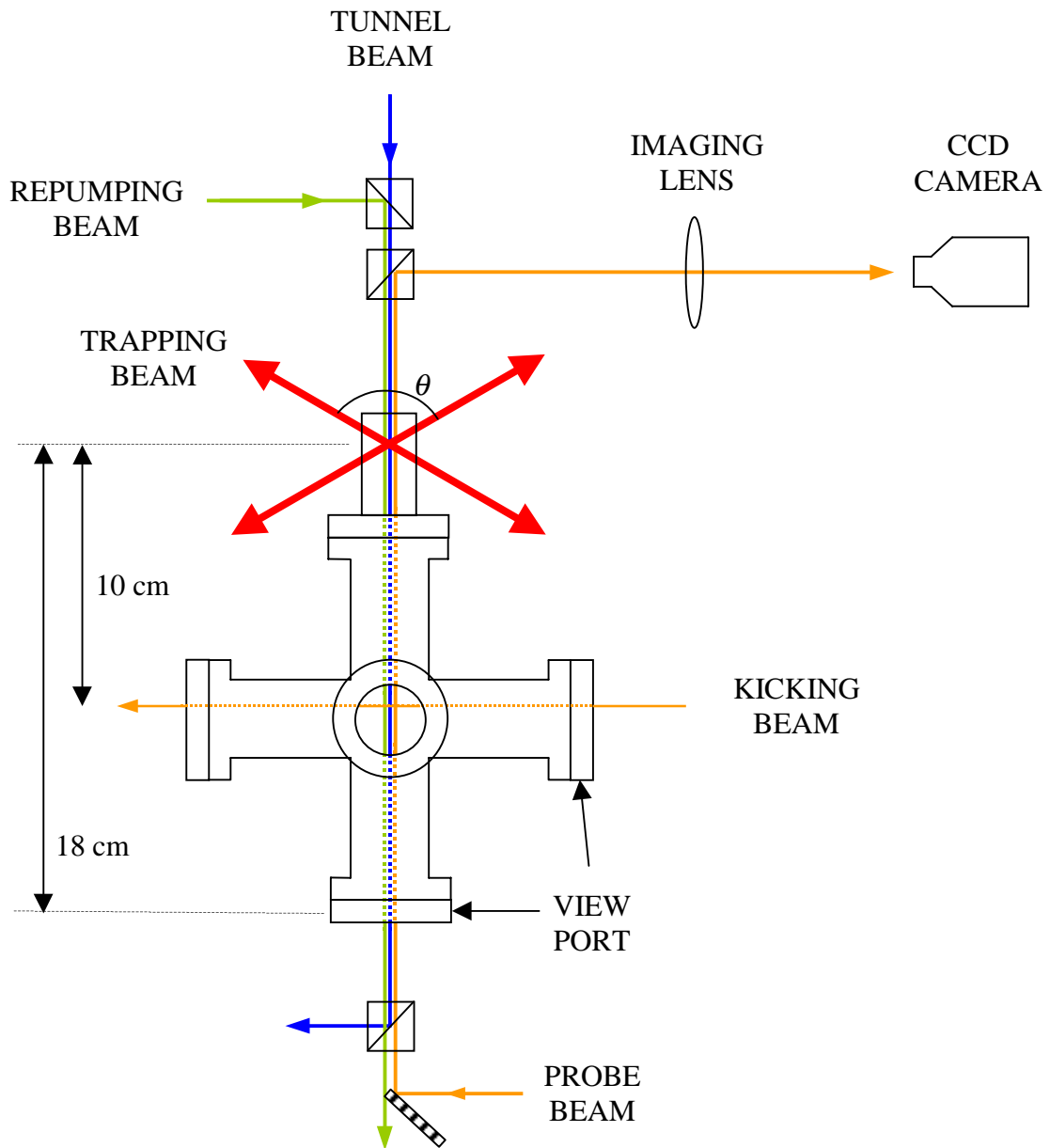


Figure 6.8 Setup for longitudinal shadow imaging. The two trapping beams intersect at $\theta = \sim 105^\circ$. The other trapping beam not shown is into and out of the paper. The tunnel, probe and repumping beams overlap in the chamber.

Figure 6.10 shows the number of atoms in the tunnel as a function of guiding time. The number of atoms was measured by integrating the density distribution in the shadow images. But, this gives only a relative value for the number of atoms. The absolute value can be obtained by considering the optical depth. As shown in the plot, the data points remain almost flat for 0-40 ms with the repumping beam (0-20 ms without the repumper) because the cloud is optically thick. When the atom cloud is optically thick, all light is absorbed. As the atoms leave the tunnel (photon absorbers decrease), the optical depth decreases, and the shadow starts to pale. This happens when the number of incident photons is equal to the maximum number of photons that can be absorbed, or in other words, the intensity of the absorbed beam is equal to that of the

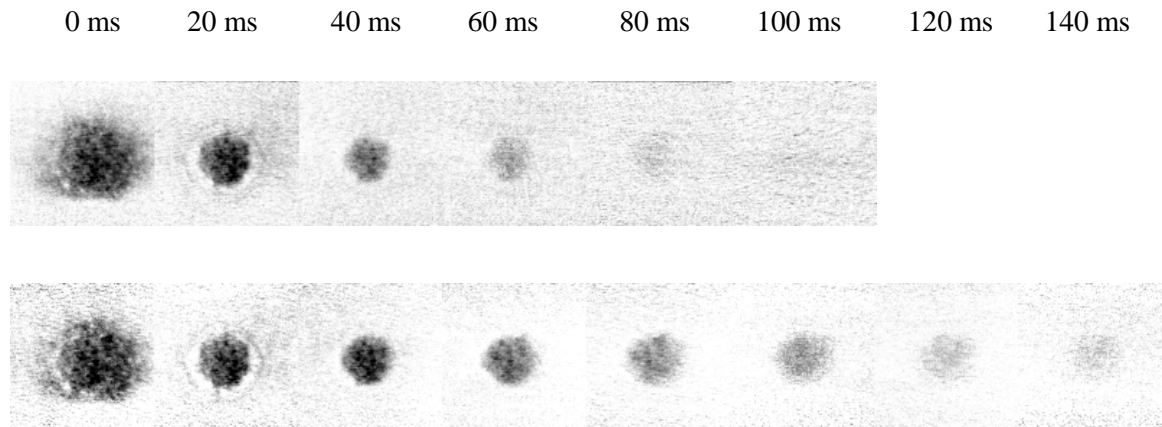


Figure 6.9 Longitudinal shadow images of the atom clouds without the repumper (top) and with the repumper (bottom) co-propagating with the tunnel beam. The tunnel beam was detuned by $\Delta = 1.5$ GHz. The bright circles around the shadow are the 1 mm diameter tunnel beam.

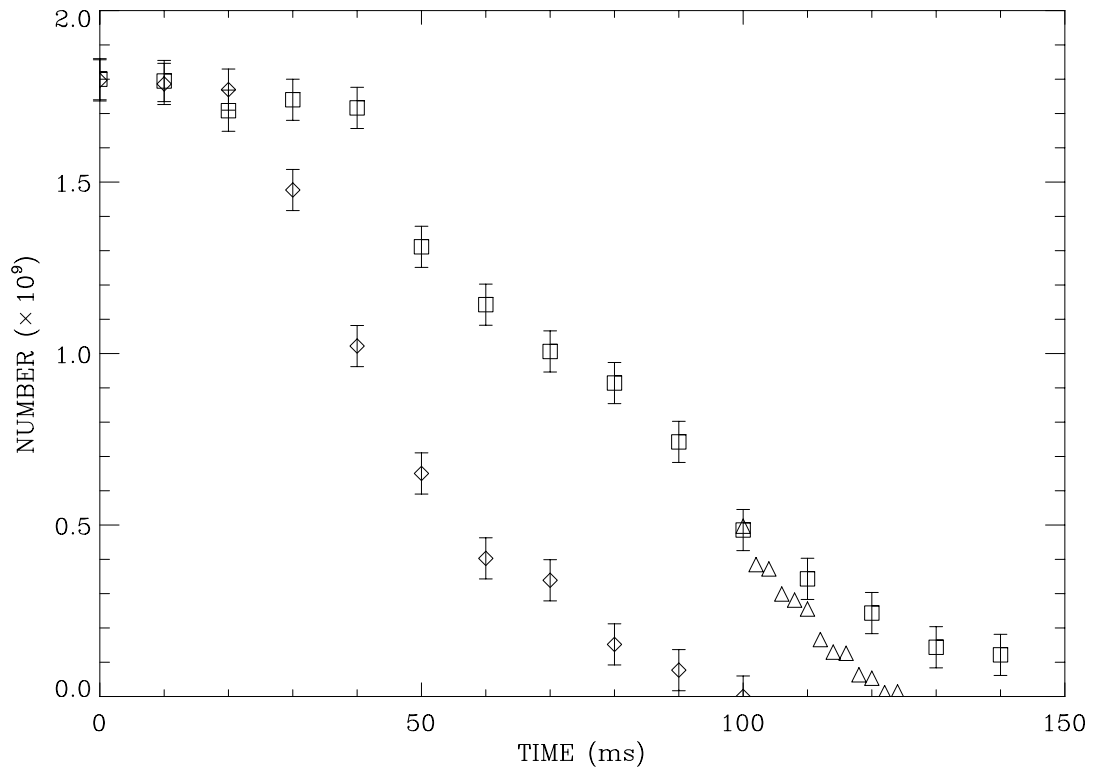


Figure 6.10 The number of Cs atoms in the tunnel vs. time from longitudinal images in Fig. 6.9 without the repumper (\diamond), with the repumper (\square), and with the kicker beam placed 10 cm below the MOT (\triangle).

incident beam. This criteria can be written as:

$$\frac{I_{ab}}{I} = \frac{nlhc\pi\Gamma}{\lambda_s \left(1 + I/I_s + 4(\Delta/\Gamma)^2\right)} = 1, \quad (6.4)$$

where I_{ab} is the intensity of the absorbed beam, n the atom density and l the length of the atom cloud. With $I/I_s \ll 1$ and $\Delta \approx 0$, Eq. 6.4 gives the number density integrated along the longitudinal direction, $nl = \sim 3 \times 10^{11} / \text{cm}^2$. Multiplying this value by the area of the tunnel gives the absolute number of atoms in the tunnel when the absorption starts to decrease. We cannot know the number of atoms before 40 ms by shadow since the absorption signal does not change. After about 40 ms, the absorption is roughly proportional to the number of atoms. Therefore, with the number at saturation as a reference, the integration over the shadow images gives absolute number of atoms.

Several things should be considered when the number of atoms is being determined. First, if the ccd camera is not sensitive at low intensity, the images will be completely dark even though not all the light is absorbed by the atoms. In that case, the number will be overestimated. Second, the camera must respond linearly to the probe beam intensity. We measured the sensitivity and linearity of our camera by varying the intensity of the probe beam. The camera was linear until the intensity was reduced to less than 5% of the probe beam intensity used for shadow imaging. Therefore, the error in the number determination caused by these effects is less than 5%. Third, the absorption by the background atoms as the probe beam traverses the chamber, as shown in Fig. 6.8, must be taken into account. The background absorption was experimentally determined to be about 10% at the pressure of $\sim 10^{-7}$ Torr. However, this does not necessarily mean

that the error is 10% since the camera sees this 10% attenuated intensity as the maximum probe beam intensity. Equation 6.4 is still valid if we replace the incident intensity I with $I - I_{bg}$ where I_{bg} is the intensity absorbed by the background atoms.

We stopped taking images at 150 ms because the atoms hit the bottom chamber window, 18 cm below the MOT, and disappeared quickly between 140 and 150 ms. As an independent check that the atoms remained in the tunnel, we introduced a 50 mW/cm² kicking beam about 10 cm below the MOT to knock the atoms out of the tunnel before they hit the window. The triangles in Fig. 6.10 shows that nearly all of the atoms were knocked out of the tunnel between 100 and 120 ms. The center-of-mass acceleration deduced for the flight time to the kicker beam is 16.5 m/s². With this acceleration the atoms reach the bottom window between 140 and 150 ms. At this point the atoms have a drift velocity of about 2.4 m/s. From the 20 ms for which the atoms pass the kicker beam, the longitudinal size is estimated to be about 3.6 cm. If we assume that 95% of the atoms are included in this length, the sigma of the distribution is about 9 mm, which agrees with Eq. 6.3 for $T \sim 80 \mu\text{K}$, $\sigma(0) \sim 3\text{mm}$, $t \sim 110 \text{ms}$.

Though $\sim 10^8$ atoms were guided to the bottom with the repumper, no atoms were detected at the bottom without the repumper because of the optical pumping to the lower hyperfine ground state. The number of atoms in the tunnel, however, decreased as they traveled in the tunnel, even with the repumper. The potential height produced by the hollow beam in Fig. 5.4 with $\Delta = 1.5 \text{GHz}$ was estimated to be about 1 mK using Eq. 5.6, which is more than 10 times the temperature ($\sim 80 \mu\text{K}$) of the atoms during their flight. The temperature remains almost the same for the 150 ms during which we monitored the atoms as shown in Fig. 5.7b. A simple way to estimate the temperature change is to use

the scattering rate. The acceleration of 5 m/s^2 gives a scattering rate of $R \approx 1200$ per second, which means the atoms absorb and emit 180 photons on average during the 150 ms flight. This corresponds to an increase of only $\sim 25 \text{ } \mu\text{K}$ in temperature. Therefore the loss is not caused by thermal escape. The primary loss mechanism is associated with collisions with the warm ($v \approx 300 \text{ m/s}$) background gases. Our guide was placed in a relatively high pressure environment, $P \approx 1.3 \times 10^{-7} \text{ Torr}$, to enhance the number of atoms trapped in the MOT. Partial pressure for other background gases was an order of magnitude lower and the collision cross-section of these light species is several times smaller than the collision cross-section of Cs. The collision cross-section of Cs atoms was found to be $\sigma = 2 \times 10^{-13} \text{ cm}^2$ [74], which gives a half-life time of $\tau = (nv\sigma)^{-1} \approx 30$ ms, where n and v are the number density and the average velocity of the background atoms respectively. The half-life measured from Fig 6.10 is $\tau_{\text{exp}} \approx 27 \text{ ms}$, consistent with the theoretical value. The half-life of the atoms in the tunnel was measured for several different detunings and found to be independent of the detuning as shown in Fig. 6.11.

In general the guiding efficiency is given by:

$$\eta = \exp(-tnv\sigma), \quad (6.5)$$

where t is the transport time. The guiding efficiency with the repumper in Fig. 6.10 is $(1/2)^{(t/\tau)} = (1/2)^5 = \sim 3\%$. To enhance the performance of the tunnel, collisions with warm atoms should be minimized. This can be accomplished by reducing the background pressure and the transport time. If the pressure is reduced to 10^{-8} Torr , the efficiency increases to $\sim 70\%$. In this case, however, the total number of transported atoms does not

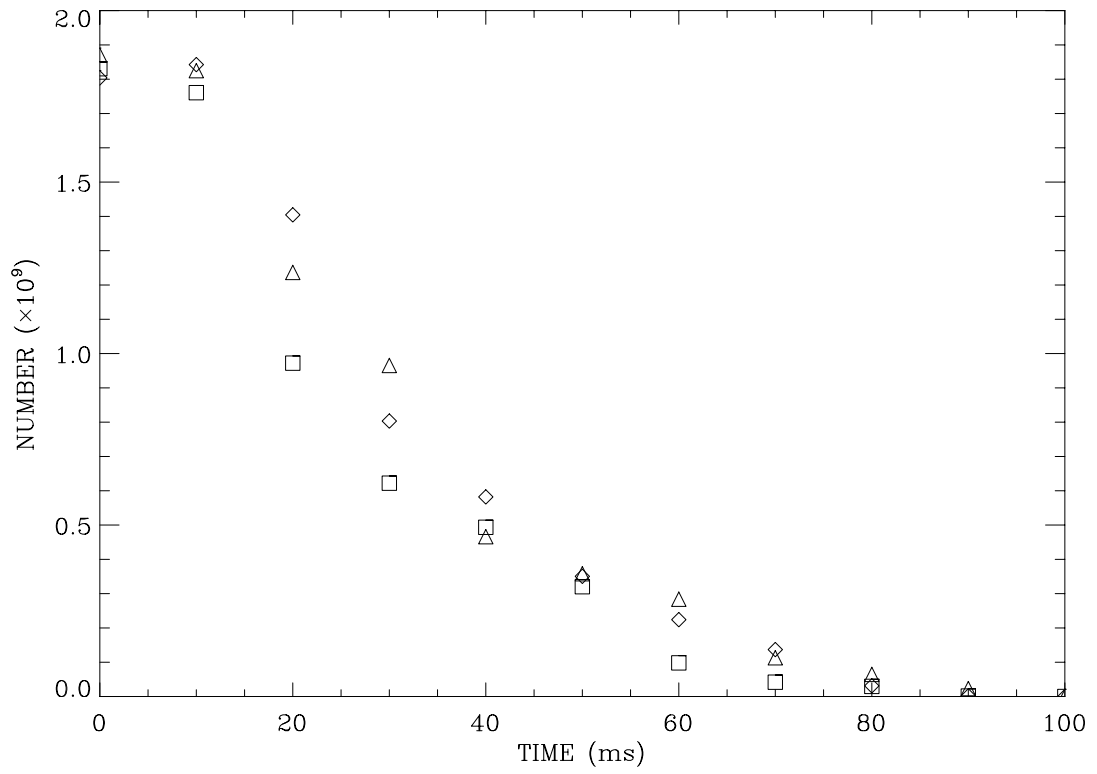


Figure 6.11 The number of atoms in the tunnel vs time with different tunnel detunings, $\Delta = 0.25$ GHz (\square), 1 GHz (\triangle), and 2 GHz (\diamond). The MOT for this plot had fewer atoms than the MOT shown in Fig. 6.9.

necessarily increase because the number of atoms trapped in the MOT is also reduced as shown in Fig. 4.6. For smaller detuning, the atoms are accelerated faster, and the transport time decreases. But, decreasing the detuning does not increase the efficiency as much because the scattering acceleration is proportional to $1/\sqrt{\Delta}$ as shown in Eq. 6.2. The efficiency is $\sim 10\%$ for $\Delta = 0.25$ GHz. A much higher guiding efficiency can be achieved by adding a kicking beam to the hollow tunnel beam. If part of the MOT trapping beam ($I \approx I_s$, $\Delta = 2\Gamma$) is used for the kicker beam, the transport time is reduced to ~ 15 ms, and the efficiency increases to $\sim 60\%$.

Since the number of atoms in the cloud and the drift velocity change as the atoms are guided, the beam flux also changes as a function of time (or position). The atomic beam shown in the bottom figure of Fig. 6.9 has a drift velocity of ~ 2 m/s and a size of ~ 2 cm after the beam is guided for 18 cm. With $\sim 10^8$ atoms guided, the flux of the beam is $\sim 10^{10}$ s $^{-1}$ (or flux density of $\sim 10^{12}$ /cm 2 ·s). The beam flux can be greatly enhanced with a kicker beam, by not only increasing the guiding efficiency but also increasing the drift velocity and decreasing the longitudinal size. With a kicker beam of $I \approx I_s$, $\Delta = 2\Gamma$, the atomic beam 18 cm below the MOT would have 2×10^9 atoms with a drift velocity of ~ 20 m/s and a size of ~ 2 mm. This corresponds to a beam flux of $\sim 2 \times 10^{13}$ s $^{-1}$ (or flux density of $\sim 2 \times 10^{15}$ /cm 2 ·s).

CHAPTER 7

ATOM FUNNEL

Several schemes for focusing neutral atomic beams are discussed in this chapter. Conventional harmonic focusing and aberrations will be discussed in section 7.1. This includes transverse optical cooling and magnetic and electric dipole focusing. An atom funnel, a new method of aberration-free focusing, will be suggested in section 7.2

7.1 Harmonic focusing and aberrations

An atomic beam with high flux density and small cross-section is desirable in many applications. The divergence of an atomic beam due to the transverse velocity components increases the size and decreases the flux density. Focusing or collimating a neutral atomic beam involves using the internal structure of the atoms. Forces related to the internal structure, such as scattering forces, electric dipole forces and magnetic dipole forces can be used to kick atoms back toward the propagation axis. In most cases the minimum spot size is limited by chromatic and spherical aberrations. When a harmonic impulse is applied on a mono-energetic beam, as shown in Fig. 7.1, the spot size at the focal point is given by $y_2 = \frac{z_2}{z_1} y_1$, where y_1 is the size of the source and z_1 and z_2 are

distances from the harmonic impulse to the source and the focal point respectively. The focal length z_2 depends on the strength of the impulse and the longitudinal (drift) velocity of the atomic beam. If the atomic beam is not mono-energetic, atoms with different longitudinal velocities spend different amounts of time in the potential. The impulse the

atoms are subject to depends not only on the transverse position but also on the longitudinal velocity. Therefore, the atoms cross the propagation axis at different positions, depending on their longitudinal velocity. If the atomic beam has a longitudinal velocity spread of δv_z , the spot size increases and is given by:

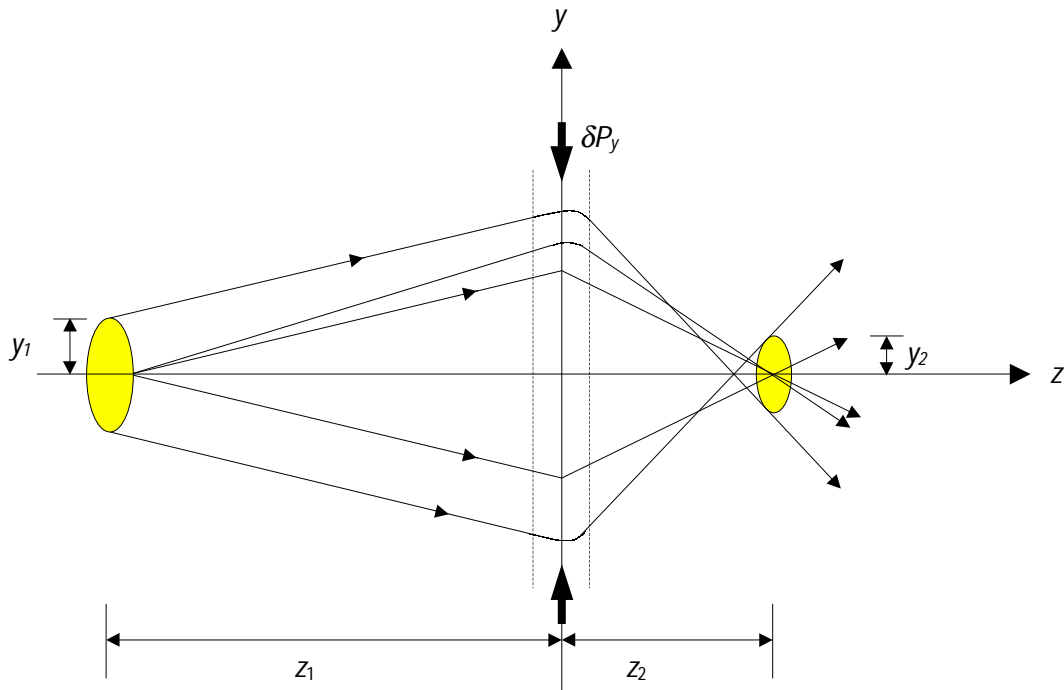


Figure 7.1 Harmonic focusing of an atomic beam. The harmonic impulse is given by $\delta P_y = -Ky\delta t$, where K is the spring constant and δt the time that the atoms experience the restoring force. Regardless of the spring constant, the compression rate is determined by the geometry, $y_1/y_2 = z_1/z_2$ provided there are no chromatic or spherical aberrations.

$$y_2 = \frac{z_2}{z_1} y_1 + 2y_1 \frac{\delta v_z}{v_z} \left(1 + \frac{z_2}{z_1} \right) \left(1 + \frac{v_y}{v_z} \frac{z_1}{y_1} \right), \quad (7.1)$$

where v_z and v_y are the longitudinal and transverse velocities of the atoms respectively. With reasonable parameters of effusive beams without velocity selection, the second term (the aberration term) is larger than the first term, which means focusing of the hot beam is limited by chromatic aberration. For an ultracold beam from a MOT, the second term is smaller than the first term, so chromatic aberration is less important in focusing an ultracold beam. Whereas the chromatic aberration is an intrinsic property of the atomic beam itself, spherical aberration comes from the anharmonicity of the focusing potential. Atoms far from the propagation axis experience non-harmonic potential and are focused at different positions.

Many different techniques for harmonic focusing have been developed. Those include focusing with radiation pressure, magnetic dipole focusing and electric dipole focusing. Focusing an atomic beam with radiation pressure is often called a 2D MOT since it works in exactly the same way as a 3D MOT except there are only four beams in the transverse direction. Tsao *et al.* achieved a spatial compression ratio of ~ 2.5 using a thermal sodium beam from an oven [75]. They pointed out that the compression ratio was limited by chromatic aberration due to the longitudinal energy spread of the atoms. Although the spatial compression ratio is not large, the momentum compression ratio that can be achieved with a hot beam is as high as 400 because of transverse cooling. This transverse cooling, however, has no effect on the ultracold beam from a MOT.

Magnetic dipole focusing employs the interaction between the magnetic moment of the atoms and the gradient of inhomogeneous magnetic field. The magnetic potential

for an atom with magnetic moment $\mu = -g_L(F)\mu_B m_F$ in a magnetic field $\vec{B}(\vec{r})$ is given by $U(\vec{r}) = g_L(F)\mu_B m_F B(\vec{r})$, where $g_L(F)$ is the Lande g-factor and μ_B the Bohr magneton (9.27×10^{-24} J/T). The potential can be either attractive or repulsive depending on the quantum state. For example, a Cs atom with $F = 3$, $m_F = 3$ has $g_L(F) = 1/4$ and is attracted toward the minimum magnetic field. This magnetic dipole interaction with an inhomogeneous magnetic field can be used to trap the atoms without using light. Bose-Einstein condensates have been contained in this type of magnetic trap [10]. Another use of the magnetic dipole interaction is to focus an atomic beam. The JILA trapping group achieved a minimum spot size of 3.5 mm (axial) \times 2.5 mm (radial) with the ultracold atoms levitated from a MOT (~ 1 mm) by the magnetic lenses made up of a pair of coils [74]. The minimum spot size was limited mainly by spherical aberration. When focusing pulses were applied, the atom cloud had ~ 1 cm diameter, and the magnetic potential was highly anharmonic. The fringing field also contributed to astigmatism. To reduce the spherical aberration, the coil should be much larger than the cloud size. To have the magnetic gradient large enough to attract atoms, the current must also be increased, which is not easy. The coils they used already had more than 10000 Amp-turn.

The most popular way of focusing a neutral atomic beam is the electric dipole focusing. Atoms in an inhomogeneous electric field can be attracted either toward the intense field or toward the weak field, depending on the laser detuning. Since the possibility of trapping and guiding neutral atoms was first suggested by A. Ashkin [27], many experiments have been performed, including focusing atomic beams with near field of diffracted laser light [76], focusing with large period standing waves [77], channeling [78] and narrow pattern formation [79] with standing waves. Focusing with a Gaussian

mode laser beam has attracted special interest. Bjorkholm *et al.* focused an effusive atomic beam that traveled through the focal spot of the superimposed Gaussian beam by a factor of about 27 ($\sim 0.76 \text{ mm} \rightarrow \sim 28 \text{ }\mu\text{m}$) [80, 81]. They also showed defocusing of the atomic beam by detuning the laser to the blue of resonance. The main mechanism that limited the minimum spot size was transverse heating caused by the spontaneous force. Since the atoms experience the most intense part of the laser beam, the random scattering

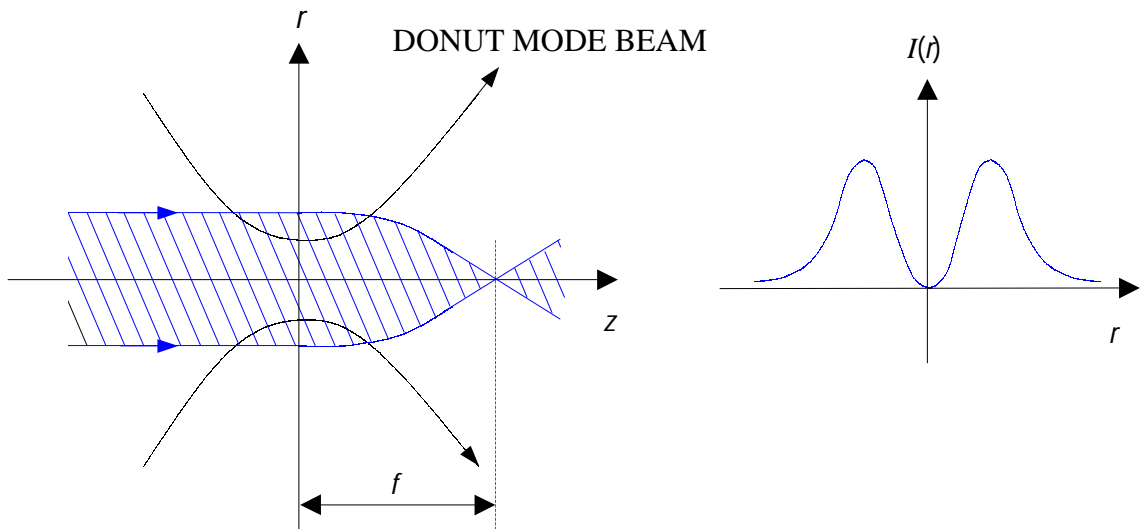


Figure 7.2 Focusing an atomic beam with a TEM_{01}^* donut mode laser beam. The focal length of the optical lens is of same order of magnitude as the spot size of the laser beam. The atomic beam can be focused to a size equal to the de Broglie wavelength. Focusing an atomic beam to the diffraction limited spot size requires a chromaticity of $\Delta v_z/v_z = 10^{-3}$ and an initial atomic beam size smaller than the laser spot size.

of the photons may not be negligible even though the laser was detuned many GHz away from resonance.

The use of a donut mode laser beam or hollow core laser beam was suggested as an alternative to Gaussian mode focusing. The atoms propagate axially with the laser beam, being focused by the gradient of the laser intensity as shown in Fig.7.2. Optical heating is negligible, and deep focusing is possible. Theoretical calculations by several groups show that an atomic beam can be focused to submicron size [82, 83, 84]. To achieve the anticipated spot size, however, the atomic beam needs to have ‘ideal’ characteristics: a chromaticity of less than 10^{-3} and an initial beam size smaller than the laser spot size. In many practical cases such as focusing an ultracold atomic beam, the beam quality is far from ideal. The initial condition assumed in the calculations is often the goal to achieve. For example, our motivation of the atom tunnel and funnel experiment was to reduce the cold atomic beam size to $\sim 10 \mu\text{m}$, which enabled us to have an atomic target inside the laser focal spot. So the focus of an ultracold atomic beam needs another scheme of focusing. The idea of an atomic funnel arose against this historical background.

7.2 Atom funnel

I noticed that instead of using the hollow laser beam as a lens near its focal point, I could squeeze the atoms through the small opening at the focus of the hollow laser beam. The atomic beam has a transverse size smaller than the focal spot size of the hollow laser beam if the dipole potential is high enough to confine the atoms. We call this an *atom funnel*. A prototype design of the atom funnel is shown in Fig. 7.3. A

TEM₀₁* mode beam with $P_0 = 30$ mW, $\Delta = 250$ MHz is focused to $10\ \mu\text{m}$ peak-to-peak transverse size ($w_0 = 7\ \mu\text{m}$). The potential depth at the focus is about 330 times the kinetic energy of the ultracold atoms in the MOT. At the position of the MOT where the peak-to-peak beam diameter is 1 mm, the potential depth is 3.4 times the kinetic energy,

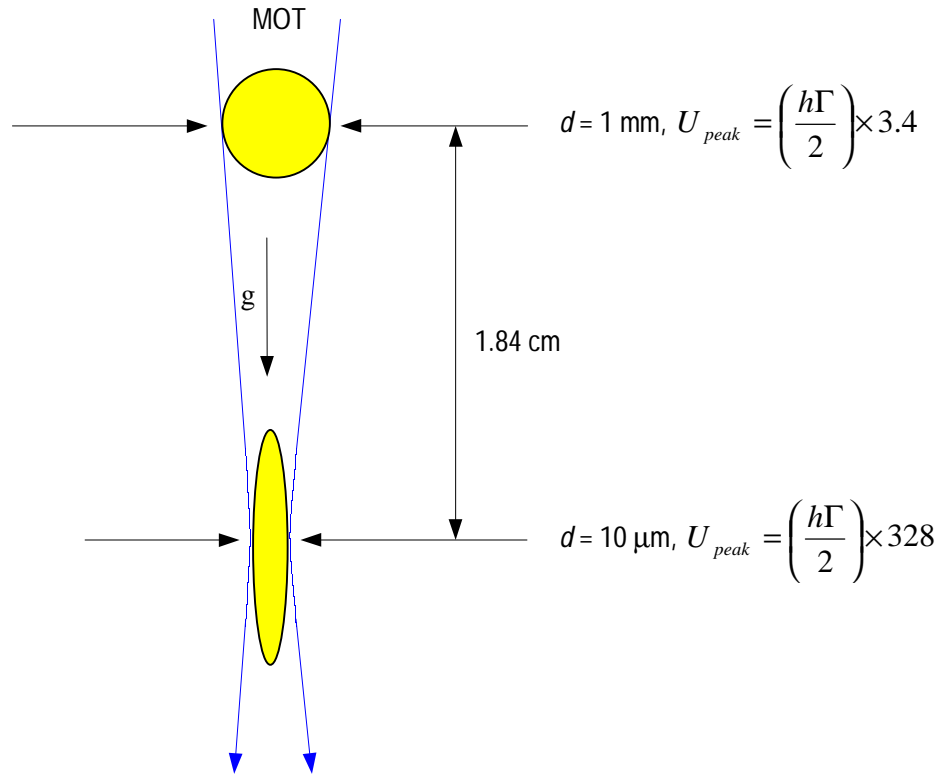


Figure 7.3 A prototype design of an atom funnel. $d (= \sqrt{2}w)$ is the peak-to-peak size. The detuning factor is $q (= \Delta/\Gamma) = 50$. The total power of the laser beam is 30 mW. The intensities are $I(d = 1\ \text{mm}) = 7 \times 10^2\ \text{mW}/\text{cm}^2$ and $I(d = 1\ \mu\text{m}) = 7 \times 10^6\ \text{mW}/\text{cm}^2$. The kinetic energy of atoms in the MOT is about $h\Gamma/2$, the Doppler limit.

which is deep enough to confine the atoms.

Various combinations of the beam power, detuning and spot size are also possible for the atom funnel. The power of 30 mW chosen in the above example is a reasonable value that can be obtained from a 100 mW diode laser. Higher power is, of course, better. The power dependence of the potential depends strongly on the position. For example, if the total laser power is increased from 30 mW to 60 mW, the potential depths are $U(d = 1 \text{ mm}) = 6.5 (h\Gamma/2)$ and $U(d = 10 \text{ }\mu\text{m}) = 360 (h\Gamma/2)$, i.e. $U(d = 1 \text{ mm})$ increases by a factor of almost two whereas $U(d = 10 \text{ }\mu\text{m})$ does not change much. The reason is that the potential is linearly proportional to the intensity for low intensity ($I/4q^2 \ll 1$) and is logarithmically dependent on the intensity for high intensity ($I/4q^2 \gg 1$).

Determining the optimum detuning is rather complicated. The detuning that maximizes the potential depends on the intensity as in Eq. 2.12. The potential is maximized for $\Delta_0 \sim 33 \text{ MHz}$ at the MOT position and $\Delta_0 \sim 330 \text{ MHz}$ at the focal point. But the detuning of 33 MHz cannot be employed since the MOT cannot coexist with the hollow laser beam at this small detuning (Δ must be more than 100 MHz as explained in Ch. 4). Nor can the detuning of 330 MHz be used since the potential is too shallow at the MOT position. If the funnel beam is detuned by 330 MHz, the potential at the MOT position is only twice the Doppler limit and may barely confine the atoms. Thus the optimum detuning should be chosen between about 100 MHz and 330 MHz. The detuning of 250 MHz seems reasonable.

The choice of spot size depends basically on how tightly we want to focus the atomic beam. If the funnel beam is focused too tightly, one has to worry about adiabatic heating of the atom beam. As the atoms travel deeper into the funnel, the size of the atom

cloud decreases. In a frame moving with the atoms, this is simply an adiabatic compression. The source of the adiabatic heating is the momentum transfer from the longitudinal direction to the transverse direction as the atoms collide with the wall as shown in Fig. 7.4. After the atoms acquire enough transverse kinetic energy, they may escape the potential walls established by the light. However, as the atomic beam is focused, the potential depth also increases. The temperature of the atoms is proportional to the beam size, i.e. $T \propto V^{1-\gamma} \propto d^{1.3}$, where V is the volume of the cloud and $\gamma = C_p/C_v =$

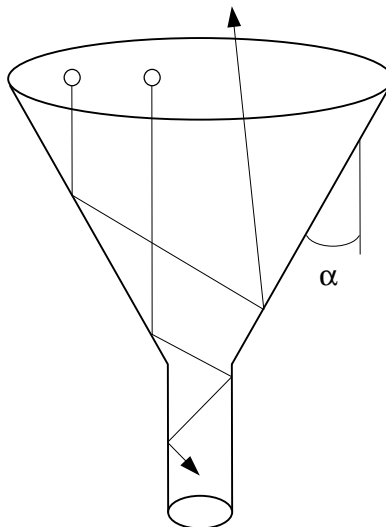


Figure 7.4 The adiabatic heating and bounce back of atoms thrown into a funnel. The angle between the funnel axis and the velocity vector of the atoms increases by 2α each time they collide with the funnel wall. When an atom is thrown into the funnel too far from the center, it may bounce back or leak through the potential walls.

5/3 the ratio of specific heats for the monoatomic gas. The dipole potential is inversely proportional to the square of the beam size ($U \propto d^{-2}$) and increases faster than the temperature as the atoms are compressed. In case the potential is not high enough to confine the atoms, the temperature can be lowered by applying two dimensional cooling beams [67].

Another problem caused by the compression is ‘bounce back.’ Each time an atom collides with the wall, its direction of motion changes by 2α , where α ($\equiv w_0 / z_R = \pi w_0 / \lambda$) is the angle of the funnel wall relative to the propagation axis. After $n = \pi/4\alpha$ collisions, the atoms lose all their longitudinal momentum and start to bounce back. This imposes a limit on the compression ratio. Using a far field approximation where the laser beam is linearly diverging for $z \gg z_R$ with z_R being the Rayleigh length, the maximum compression ratio is given by $1/\alpha$. The angle in the above example ($w_0 = 7 \mu\text{m}$) is $\alpha = 26$ mrad, and the maximum compression ratio is 38. This means that the 1 mm atom ball will be compressed to 26 μm before the atoms bounce back. However, in the actual experiment, the shape of the funnel beam is not a cone but nearly parallel near the focal point. So the situation is not so severe as one may think. Furthermore, the forces that push the atoms into the funnel – gravity and the scattering force by the funnel beam – must be considered. As a pingpong ball would eventually fall through a funnel, the atoms also go through the funnel waist if the funnel potential is high enough. Ertmer *et al.* reported compressing a 750 μm Zeeman slowed beam to 17 μm with a TEM_{01}^* beam generated by a computer-generated hologram [85]. To prevent transverse heating, they applied a two-dimensional cooling beam near the focus.

We created an atom funnel by focusing the axicon generated hollow beam. With a 20 cm focal length lens on top of the glass cell (3 cm above the MOT), a funnel beam with its focus near the bottom window was generated. The funnel beam, however, does not maintain its hole at the focus as shown in image (7) of Fig. 5.2. The reason is that axicons modify only the intensity not the phase. Consequently the axicon generated hollow beam does not have a phase that depends on the azimuthal angle. When the axicon generated beam is focused, the intensity adds up at the center. The minimum peak to peak diameter when the hollow core starts to disappear was about 100 μm . In principle, the phase dependence can be added to the axicon generated beam with holograms or phase masks.

Figure 7.5 shows the shadow images of atom cloud in the funnel. Unfortunately, these images were taken without the repumper since this experiment was done before we

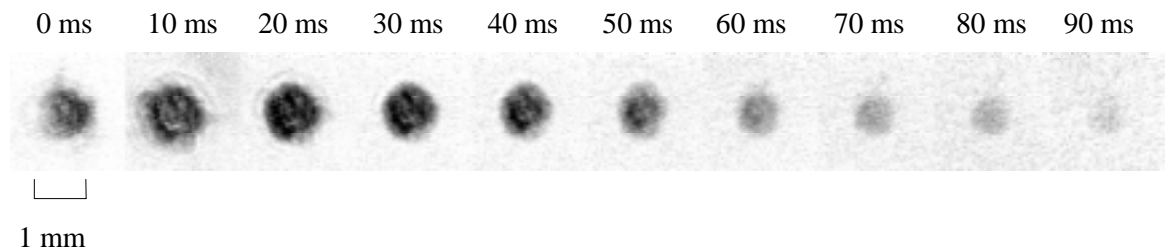


Figure 7.5 Shadow images of the atom cloud in the funnel without the repumping beam. The atoms were guided ~ 5 cm for 90 ms. The funnel was focused by 20 cm focal length lens. Over the 5 cm, the funnel diameter was reduced by 30%; The size of the atom cloud decreased from 138 pixels at 0 ms to 96 pixels at 90 ms

noticed the loss by optical pumping. So the shadow imaging was visible for only ~90 ms during which the atoms traveled about 5 cm.

During this time, the diameter of the funnel was reduced by 30%, 5 cm below the MOT compared to the funnel diameter at the MOT position. In the shadow images, the size of the atom cloud decreased from 138 pixels (about 1 mm) at 0 ms to 96 pixels (about 0.7 mm) at 90 ms and agreed with the funnel size. With the repumper, the atoms would travel to near the focus of the funnel beam since the funnel angle is very small ($\alpha = 5.5$ mrad) and the potential is high.

It would be interesting to see what happens at the focus where the hole disappears. One possibility is that the atoms are trapped in the conical potential walls [67]. But in our case this seems unlikely because of the large drift velocity unless the atoms are slowed down by a laser beam directed upward.

CHAPTER 8

SUMMARY

In this thesis, a novel way of transporting neutral atoms has been developed. We demonstrated a hollow beam atom tunnel by guiding magneto-optically trapped Cs atoms with an axicon generated hollow beam for approximately 20 cm. Using shadow imaging technique we could follow the atoms all the way through their travel in the tunnel. Characteristics of atomic ensembles in the tunnel, such as the total number and density distribution of the atoms, the center-of-mass position and the size, were measured as a function of time.

The axicon generated hollow beam used to construct our atom tunnel had a large dark core and a steep wall. The 1 mm axicon beam has a shape factor about 10 times smaller than TEM_{01}^* modes, which allowed atoms to be transported with a minimal interaction with the light. The potential wall in the axicon generated hollow beam was modeled as an extended harmonic potential, which enabled us to evaluate the shape factor analytically. Using the shape factor, we could solve the equations for the position and the size of atom clouds in the tunnel. The solutions revealed some counterintuitive properties of the tunnel operation, such as suppression of the optical acceleration with increasing power of the tunnel beam. The experimental observations were in good agreement with our theoretical model.

We showed that by adjusting the detuning and the direction of the tunnel beam relative to gravity, it is possible to control the speed and direction of the atoms in the tunnel. The guiding efficiency of the atom tunnel over 20 cm at a detuning of 1.5 GHz

was about 3%. The loss mechanism turned out to be associated with collisions with warm background Cs atoms. To enhance the guiding efficiency, these collisions must be minimized by reducing the pressure or the guiding time.

I discussed how reducing the core size of a hollow beam could lead to a novel way of focusing neutral atomic beams. Atoms in the hollow beam atom funnel could be focused as small as the core size of the hollow beam. However, the axicon generated hollow beam can not be used for a tight focus because the core disappears when the beam is focused. To preserve the dark core at the focus, the hollow beam must be a pure Laguerre-Gaussian mode. This might be done with holograms or phase masks.

The hollow beam atom tunnel and funnel have many possible applications. They could provide small atomic targets for intense laser field experiments. They might help to enhance the resolution in atom lithography. Ultraprecision spectroscopy, interferometry and collision studies could employ the atom tunnel and funnel. Fundamental physics in small sizes or reduced dimensions might be possible in the light walls. Finally they could provide a way to transport and manipulate Bose-Einstein condensates as well as antimatter.

REFERENCES

1. E. L. Raab, M. Prentiss, A. Cable, S. Chu, D. E. Prichard, *Phys. Rev. Lett.* **59**, 2631 (1987).
2. P. D. Lett, P. S. Jessen, W. D. Phillips, S.L. Rolston, C. I. Westbrook, P. L. Gould, *Phys. Rev. Lett.* **67**, 2139 (1991).
3. L. Marcassa, V. Bagnato, Y. Wang, *Phys. Rev. A* **47**, R4563 (1993).
4. J. Weiner, V. S. Bagnato, P. S. Julienne, *Rev. of Mod. Phys.* **71**, 1 (1999).
5. T. P. Dinneen, C. D. Wallace, K. N. Tan, P. L. Gould, *Opt. Lett.* **17**, 1706 (1991).
6. J. D. Miller, R. A. Cline, D. J. Heinzen, *Phys. Rev. Lett.* **71**, 2204 (1993).
7. S. Wolf, H. Helm, *Phys. Rev. A* **56**, R4385 (1997).
8. M. A. Kasevich, E. Riis, S. Chu, *Phys. Rev. Lett.* **63**, 612 (1989).
9. J. W. Tabosa, G. Chen, Z. Hu, R. B. Lee, H. J. Kimble, *Phys. Rev. Lett.* **66**, 3245 (1991).
10. M. H. Anderson, J. R. Ensher, M. R. Matthews, C. E. Wieman, E. A. Cornell, *Science* **269**, 198 (1995).
11. R. E. Scholten, J. J. McClelland, E. C. Palm, A. Gavrin, R. J. Celotta, *J. Vac. Sci. Technol. B* **12**, 1847 (1994).
12. R. Abfalterer, C. Keller, S. Bernet, M. K. Oberthaler, J. Schmiedmayer, A. Zeilinger, *Phys. Rev. A* **56**, R4365 (1997).
13. See F. Reif, *Fundamentals of Statistical and Thermal Physics* (McGraw-Hill, Inc., 1965), pp 274.

14. Y. Song, D. Milam, W. T. Hill III, *Opt. Lett.* **24**, in press (1999)
15. E. Riis, D. S. Weiss, K. A. Moler, S. Chu, *Phys. Rev. Lett.* **64**, 1658 (1989).
16. Z. T. Lu, K. L. Corwin, M. J. Renn, M. H. Anderson, E. A. Cornell, C. E. Wieman, *Phys. Rev. Lett.* **77**, 3331 (1996).
17. M. A. Ol'Shanii, Y. B. Ovchinnikov, V. S. Letokhov, *Opt. Comm.* **98**, 77 (1992).
18. M. J. Renn, D. Montgomery, O. Vdovin, D. Z. Anderson, C. E. Wieman, E. A. Cornell, *Phys. Rev. Lett.* **75**, 3253 (1995).
19. H. Ito, T. Nakata, K. Sakaki, M. Ohtsu, K. I. Lee, W. Jhe, *Phys. Rev. Lett.* **76**, 4500 (1996).
20. J. Yin, Y. Lin, K. Lee, H. Nha, H. Noh, Y. Wang, K. Oh, U. Paek, W. Jhe, *J. Korean Phys. Soc.* **33**, 362 (1998).
21. M. Schiffer, M. Rauner, S. Kuppens, M. Zinner, K. Sengstock, W. Ertmer, *Appl. Phys. B* **67**, 1 (1998).
22. P. Lebedev, *Ann. Phys.* **6**, 433 (1901).
23. O. R. Frish, *Phys. Zs.* **86**, 42 (1933).
24. A. Siegman, *Lasers* (University science books, 1986, CA), pp 626-697.
25. T. Kuga, Y. Torii, N. Shiokawa, T. Hirano, *Phys. Rev. Lett.* **78**, 4713 (1997).
26. T. W. Hänsch, A. L. Schawlow, *Opt. Comm.* **13**, 68 (1975).
27. A. Ashikin, *Phys. Rev. Lett.* **40**, 729 (1978).
28. J. P. Gordon, A. Ashkin, *Phy. Rev. A* **21**, 1606 (1980).
29. For a discussion of saturation or power broadening, see R. Pantell and E. Puthoff, *Fundamentals of Quantum Electronics* (Wiley, 1969, New York), pp 71-74, or W.

- Demtröder, *Laser Spectroscopy* (Springer-Verlag Berlin Heidelberg, New York, 1982), pp 105-106.
30. W. D. Phillips, H. Metcalf, *Phys. Rev. Lett.* **48**, 596 (1982).
 31. J. V. Prodan, W. D. Phillips, H. Metcalf, *Phys. Rev. Lett.* **49**, 1149 (1982).
 32. J. Prodan, A. Migdall, W. D. Phillips, *Phys. Rev. Lett.* **54**, 992 (1985).
 33. R. N. Watts, C. E. Wieman, *Opt. Lett.* **11**, 291 (1986).
 34. V. S. Bagnato, G. P. Lafyatis, A. G. Martin, E. L. Raab, R. N. Ahmad-Bitar, D. E. Pritchard, *Phys. Rev. Lett.* **58**, 2194 (1987).
 35. D. J. Wineland, W. M. Itano, *Phys. Rev. A* **20**, 1521 (1979).
 36. For example, see F. Reif, *Fundamentals of statistical and thermal physics* (McGraw-Hill, Inc., 1965), pp 4-17.
 37. P. D. Lett, R. N. Watts, C. I. Westbrook, W. D. Phillips, *Phys. Rev. Lett.* **61**, 169 (1988).
 38. C. Salomon, J. Dalibard, W. D. Phillips, A. Clairon, S. Guellati, *Europhys. Lett.* **12**, 683 (1990).
 39. A. M. Steane, C. J. Foot, *Europhys. Lett.* **14**, 231 (1991).
 40. J. Dalibard, C. Cohen-Tannoudji, *J. Opt. Soc. Am. B.* **6**, 2020 (1989).
 41. P. J. Ungar, D. S. Weiss, E. Riis, S. Chu, *J. Opt. Soc. Am. B.* **6**, 2058 (1989).
 42. J. E. Bjorkhom, R. R. Freeman, A. Ashikin, D. B. Pearson, *Phys. Rev. Lett.* **41**, 1361 (1978).
 43. J. E. Bjorkhom, R. R. Freeman, A. Ashikin, D. B. Pearson, *Opt. Lett.* **5**, 111 (1979).

44. V. I. Balykin, V. S. Letokhov, *Opt. Comm.* **64**, 151 (1987).
45. G. M. Gallatin, P. L. Gould, *J. Opt. Soc. Am. B* **8**, 502 (1991).
46. J. J. McClelland, M. R. Scheinfein, *J. Opt. Soc. Am. B* **8**, 1974 (1991).
47. R. Ludeke, E. P. Harris, *Appl. Phys. Lett.* **20**, 499 (1972).
48. M. Fleming, A. Mooradian, *IEEE J. of Quantum Electronics* **QE-17**, 44 (1981).
49. C. Wieman, L. Hollberg, *Rev. Sci. Instrum.* **62**, 1 (1990).
50. K. B. MacAdam, A. Steinbach and C. Wieman, *Am. J. Phys.* **60**, 1098 (1992).
51. C. E. Tanner, A. E. Livingston, R. J. Rafac, F. G. Serpa, K. W. Kukla, H. G. Berry, L. Young, C. A. Kurtz, *Phys. Rev. Lett.* **69**, 2765 (1992).
52. L. Young, W. T. Hill III, S. J. Sibener, S. D. Price, C. E. Tanner, C. E. Wieman, S. R. Leone, *Phys. Rev. A* **50**, 2174 (1994).
53. E. L. Raab, M. Prentiss, A. Cable, S. Chu, D. E. Prichard, *Phys. Rev. Lett.* **59**, 2631 (1987).
54. C. Monroe, W. Swann, H. Robinson, C. Wieman, *Phys. Rev. Lett.* **65**, 1571 (1990).
55. C. Wieman, G. Flowers, S. Gilbers, *Am. J. Phys.* **63**, 317 (1995).
56. K. I. Lee, J. A. Kim, H. R. Noh, W. Jhe, *Opt. Lett.* **21**, 1117 (1996).
57. J. A. Kim, K. I. Lee, H. R. Noh, W. Jhe, M. Ohtsu, *Opt. Lett.* **22**, 117 (1997).
58. A. V. Mamaev, M. Saffman, A. A. Zozulya, *Phys. Rev. Lett.* **77**, 4544 (1996).
59. A. V. Mamaev, M. Saffman, A. A. Zozulya, *Phys. Rev. A* **56**, R1713 (1997).
60. H. Lee, B. Stewart, K. Choi, H. Fenichel, *Phys. Rev. A* **49**, 4922 (1994).
61. C. Paterson, R. Smith, *Opt. Comm.* **124**, 121 (1996).

62. J. Yin, H. Noh, K. Lee, K. Kim, Y. Wang, W. Jhe, *Opt. Comm.* **138**, 287 (1997).
63. I. Manek, Y. B. Ovchinnikov, R. Grimm, *Opt. Comm.* **147**, 67 (1998).
64. J. H. Mcleod, *J. Opt. Soc. Am.* **44**, 592 (1954).
65. M. Rioux, R. Tremblay, P. A. Belanger, *Appl. Optics* **17**, 1532 (1978).
66. T. R. Clark, H. M. Milchberg, *Phys. Rev. Lett.* **81**, 357 (1998).
67. Y. B. Ovchinnikov, I. Manek, A. I. Sidorov, G. Wasik, R. Grimm, *Europhys. Lett.* **43**, 510 (1998).
68. R. M. Herman, T. A. Wiggins, *J. Opt. Soc. Am. A* **8**, 932 (1990).
69. T. Kuga, Y. Torii, N. Shiokawa, T. Hirano, *Phys. Rev. Lett.* **78**, 4713 (1997).
70. V. I. Balykin, D. V. Laryushin, M. V. Subbotin, V. S. Letokhov, *JETP Lett.* **63**, 802 (1996).
71. J. Yin, Y. Zhu, W. Jhe, Z. Wang, *Phys. Rev. A* **58**, 509 (1998).
72. Y. B. Ovchinnikov, J. Soding, R. Grimm, *JETP Lett.* **61**, 21 (1995).
73. H. Ito, K. Sakaki, T. Nakata, W. Jhe, M. Ohtsu, *Opt. Comm.* **115**, 57 (1995).
74. C. R. Monroe, *Experiments with optically and magnetically trapped cesium atoms*, Ph.D thesis, University of Colorado, Boulder, 1992.
75. C. C. Tsao, Y. Wang, J. Weiner, V. S. Bagnato, *J. of Applied Phys.* **80**, 8 (1996).
76. V. I. Valykin, V. S. Letokhov, V. V. Klimov, *JETT Lett.* **59**, 235 (1994).
77. T. Sleator, T. Pfau, V. Balykin, J. Mlynek, *App. Phys. B* **54**, 375 (1992).
78. C. Salomon, J. Dalibard, A. Aspect, H. Metcalf, C. Cohen-Tannoudji, *Phys. Rev. Lett.* **59**, 1659 (1987).

79. R. E. Scholten, J. J. McClelland, E. C. Palm, A. Gavrin, R. J. Celotta, *J. Vac. Sci. Technol. B* **12**, 1847 (1994).
80. J. E. Bjorkholm, R. R. Freeman, A. Ashkin, D. B. Pearson, *Phys. Rev. Lett.* **41**, 1361 (1978).
81. J. E. Bjorkholm, R. R. Freeman, A. Ashkin, D. B. Pearson, *Optics Lett.* **5**, 111 (1980).
82. V. I. Balykin, V. S. Letokhov, *Optics Comm.* **64**, 151 (1987).
83. G. M. Gallatin, P. L. Gould, *J. Opt. Soc. Am. B* **8**, 502 (1991).
84. J. J. McClelland, M. R. Scheinfein, *J. Opt. Soc. Am. B* **8**, 1974 (1991).
85. S. Kuppens, M. Rauner, M. Schiffer, G. Wokurka, T. Slawinski, M. Zinner, K. Sengstock, W. Ertmer, *OSA TOPS on Ultracold Atoms and BEC* **7**, 102 (1996).